University of Limoges

University of Brescia

UNIVERSITÉ FRANCO ITALIENNE | UNIVERSITÀ ITALO FRANCESE

Ecole Doctorale EDT1
Sciences et ingénierie
pour l'information

Facoltà di Ingegneria
XXV ciclo

Thesis n°. 69/2011

Co-directed PhD Thesis

to obtain the title of

PhD of University of Limoges
PhD of University of Brescia

Specialty : ELECTRONICS OF HIGH FREQUENCIES AND OPTOELECTRONICS, ELECTRONIC INSTRUMENTATIONS

Defended by

Marco ANDREANA

Soliton propagation in crystals and optical fibres

Thesis co-directed by Vincent COUDERC and Costantino DE ANGELIS

prepared at Xlim, department of PHOTONICS

defended on December 6, 2011

Jury :

Alain BARTHELEMY	-	CNRS/Xlim Limoges (President)
Philippe DELAYE	-	CNRS/Institut d'Optique (Reviewer)
Vittorio FERRARI	-	Universitá di Brescia (Reviewer)
Stefano BOSCOLO	-	Universitá di Udine (Reviewer)
Alessandro TONELLO	-	CNRS/Xlim Limoges
Philippe LEPROUX	-	CNRS/Xlim Limoges
Costantino DE ANGELIS	-	Universitá di Brescia
Vincent COUDERC	-	CNRS/Xlim Limoges
Fabio BARONIO	-	Universitá di Brescia

Contents

List of Figures

List of Tables

Preface

Since the first demonstration of laser emission realized by Maiman in 1960, a large variety of applications have been developed[1]. At present days, one of the most challenging and booming field is biophotonics, where laser emission is used for the chemical and the metrology of biological elements constituting the living tissues[2]. For example, flow cytometry is a technique able to displace microscopic elements, like cells in a fluid, in order to probe them by multiparametric analysis[3,4]. This technique allows simultaneous measurements of the physical and/or chemical characteristics of particles by using bioelectric impedencemetry, fluorescence, diffraction, electro-absorption[5,6]... To realize this type of analysis, multiwavelength optical sources are key devices with large potentialities in simultaneous probing of marked cells.

The Laser is a device able to generate coherent light in space or in time domain[1]. This particular system, based on light amplification, can deliver intense optical field but the available wavelengths are limited to some discrete values imposed by the physics that is behind the principle of stimulated emission. Among the various solid-state lasers that are currently commercialized, those which are the most commonly used emit in the infrared region. Advantageously, these lasers are relatively low cost and easy to fabricate. In general, they produce a "quasi-monochromatic" emission, whose spectrum is distributed among several longitudinal and/or trans-

[1] J. Hecht; "Beam: The Race to Make the Laser," Optics and Photonics News, Vol. 16, pp.24-29 (2005).

[2] S.K. Mohanty, M. Sharma, P.K. Gupta, "Biophotonics: Nanosecond Near-Infrared Laser Assisted Microinjection Into Targeted Cells," Optics and Photonics News, Vol. 14, pp.17-17 (2003).

[3] M.R. Melamed, T. Lindmo and M.L. Mendelson, "Flow cytometry and sorting Second Edition," Wiley-Liss, New York, 1-9 (1990).

[4] H.M. Shapiro, "Practical Flow Cytometry Second Edition," A.R. Liss, New York (1988).

[5] H.E. Kubitschek, "Electronic measurement of particle size," Research (London), Vol. 13, 128-135 (1960).

[6] L.A. Kamentsky, M.R. Melamed and H. Derman, "Spectrophotometer: New instrument for ultra rapid cell analysis," Science, 150, 630-631 (1965).

verse modes having slightly different wavelengths. The output spectral width is generally reduced to few nanometers or a few tens of nanometres[7]. Only dye lasers exhibit larger spectrum, allowing moderate wavelength tuning in the visible domain. Additionally, bulk lasers, as typically femtosecond oscillators, can possibly deliver very short pulses whose spectral width can extend over $\sim$800 nm[8]. Nevertheless, no laser is capable to produce at the same time a broadband and bright spectrum of light covering, for instance, the whole silica transparency window, which ranges between 400 nm and 2.2 μm. The only possible solution to produce such a ultralarge spectrum is to exploit cascaded frequency conversion by means of nonlinear light/matter interaction.

In spectroscopy, as well as in many futuristic applications in biophotonics, the managing of time delays between the different wavelengths interacting via the non-linearity may open a route towards new applications. For this reason, I have studied in my work the way to equalize and control group velocities of different regions of an optical spectrum.

I have considered the case of second order susceptibility in nonlinear crystals, due to their large nonlinear response. In this case, the nonlinear control arises from the knowledge of exact and explicit expressions for the self-sustained optical waveform called solitons.

Under the same perspective, I have then analysed the case of third-order nonlinear susceptibility. In this case, I have focused my attention on propagation of laser light in nonlinear fibres. Fibre-based components are remarkably attractive in this context, because they allow to design compact, easy-to-use, robust and powerful broadband light sources. In particular, the combination of silica-based microstructured optical fibres with microchip lasers has already led to the achievement of dazzling results, with the experimental demonstration of very compact polychromatic radi-

[7] W. Koechner, D.K. Rice, "Birefringence of YAG: Nd Laser Rods as a Function of Growth Direction," JOSA, Vol. 61, pp.758-766 (1971).

[8] G. Cerullo, S. De Silvestri, V. Magni, L. Pallaro, "Resonators for Kerr-lens mode-locked femtosecond Ti:sapphire lasers," Opt. Lett., Vol. 19, pp.807-809 (1994).

ations (supercontinuum sources)[9]. These supercontinuum sources thus represent a revolutionary alternative to those which are currently commercially available, as typically incoherent white light sources including xenon arc lamps, halogen lamps, SLED's, or to the multiplexing of different lasers, each one delivering a single ray in the visible range. Indeed, the advantages of supercontinuum sources are dramatically large, since they are clearly more powerful than incoherent sources and much cheaper than any set of lasers.

That type of polychromatic optical sources (continuum) is based on nonlinear conversion of a powerful light source. The nonlinear behaviour is then controlled by the strong spatial confinement of light and by engineering the chromatic dispersion of the fiber by the well-known technique called microstructuration. By this way, ultralong fibreguides of few micrometers of core diameter and with zero dispersion wavelength easily tunable from green to infrared wavelengths can be designed and produced at the industrial level[10]. The propagation of a high power laser radiation into those fibreguides gives rise to nonlinear interaction mainly due to Kerr effect with large spectral broadening.

In the normal dispersion regime, the nonlinear Kerr response manifests as a complex interplay between self-phase modulation, Raman effect and four-wave mixing. In the anomalous dispersion regime instead, the main observed nonlinear phenomena are modulation instability, soliton propagation and soliton self-frequency shift.

Solitons, which results from the balance between dispersion and nonlinearity are very interesting phenomenon because of their particle-like behaviour. Any complex mixing between all these particles, by means of temporal attraction, repulsion, and fusion, may significantly change

[9]J.M. Dudley, L. Provino, N. Grossard, H. Maillotte, R.S. Windeler, B.J. Eggleton, S. Coen, "Supercontinuum generation in airâĂŞsilica microstructured fibers with nanosecond and femtosecond pulse pumping," JOSA B, Vol. 19, pp.765-771 (2002).

[10]T.A. Birks, J.C. Knight, and P.St.J. Russell, "Endlessly single-mode photonic crystal fiber," Opt. Lett., Vol. 22, 961âĂŞ963(1997).

the velocity of the interacting waves[11]. In these conditions, the frequency conversion efficiency is drastically modified with a direct impact on the overall spectral broadening.

Additionally, the fibre chromatic dispersion, leading to different group and phase velocities for distinct wavelengths, has another strong impact on the spectral broadening. Dispersion may lead to a progressive distribution of the radiation in different time windows, causing serious issues in nonlinear conversion efficiency. Fibre dispersion has then to be considered to improve the energetic properties of supercontinuum sources.

In this context, I have first studied new types of nonlinear solitonic and simultonic propagations by means of sum-frequency generation. This unusual dynamics of propagation allows group velocity compensation between all the interacting waves. In a second step, I have investigated the nonlinear solitonic propagations in optical microstructured fibers leading to spectral broadening toward the infrared region of the spectrum. Part of this work has been carried out in the framework of an European project called "NextGenPCF". My PhD thesis has been done under a joint supervision program (Cotutelle-de-Thése) between the Universities of Brescia and Limoges. My work has been also partially supported by the Université Franco-Italienne under the program "Vinci".

In the **first chapter** of this thesis, I will introduce a theoretical approach on soliton propagation in media with quadratic non-linearity. I will briefly introduce these special solutions from a mathematical point of view and I will describe some basics on three wave interaction.

In the **second chapter**, I will present an experimental demonstration of the existence of two particular solitonic solutions obtained in nonlinear crystal cut for second harmonic generation. I will show the experimental

[11] M.N. Islam, G. Sucha, I. Bar-Joseph, M. Wegener, J.P. Gordon, and D.S. Chemla, "Femtosecond distributed soliton spectrum in fibers," JOSA B, Vol. 6, 1149-1158 (1989).

demonstration of the existence of Zakharov-Manakov solitons, which result from the mixing of three waves travelling with their own linear group velocity, and interacting just for a short overlap time. Then I will show some experimental evidences on the existence of simultons, which result from the mutual trapping of waves at three different frequencies thus travelling while locked together with a common group velocity.

The **third chapter** concerns with a direct application of the Zakharov-Manakov solitons. I will present an experimental evidence of mode-locking operation of a flash-lamp pumped Nd:YAG laser. I show that this type of solitonic propagation displayed in a laser resonator may be used as a fast saturable absorber allowing picosecond pulse generation.

The **fourth chapter** introduces the physical principles governing infrared supercontinuum generation in terms of the nonlinear processes involved in the spectral broadening of an initial monochromatic input optical pulse. This spectral broadening is obtained by means of particular microstructured waveguides, called photonic crystal fibre (PCF). It allows supercontinuum generation from UV to infrared domains.

In the **fifth chapter** the impact of pump pulse duration on supercontinuum generation is theoretically and numerically investigated. This study is realized in the anomalous dispersion regime, where solitonic propagation is dominant and by using picosecond or subnanosecond pump pulses whose peak power is fixed. From numerical simulations I have identified the mechanisms responsible for the formation of the infrared part of the continuum spectrum.

The **last chapter** concerns a simplified analytical model to describe the mechanisms that govern the building of the supercontinuum spectrum towards the infrared. A qualitative comparison between experimental, nu-

merical and analytical results will be presented. This model may help in the optimization of spectral broadening by controlling the soliton-soliton interaction during their propagation in an optical fibre.

CHAPTER 1

Basics on quadratic solitons

Contents

In this chapter I present some basic theoretical concepts necessary for understanding the experimental results which will be illustrated in the next chapter. This chapter is organized as follows: first, we derive the coupled equations for the three-wave resonant interaction. Next we present some unusual soliton-like solution for these equations, and finally we try to explain some techniques that could be used for sum-frequency generation.

1.1 Three-wave resonant interaction

The three-waves resonant interaction (TWRI) is a process which appears in various branch of physics, such as fluid dynamics and optics. It describes the nonlinear mixing of three quasi-monochromatic waves in weakly nonlinear and dispersive media. In optics, the resonant interaction may occur in any medium where nonlinear effects may be assumed as weak perturbations of a linear propagation model.

The model describing the TWRI is derived from Maxwell equations in a dielectric medium with quadratic nonlinear susceptibility $\chi^{(2)}$. If $\mathbf{P}(\mathbf{r}, t)$ is the dielectric polarization vector field induced by an electromagnetic wave,

the charge and current densities in the medium are defined as:

$$\rho = -\nabla_r \cdot \mathbf{P}\ ,\ \mathbf{J} = \mathbf{P}_t. \tag{1.1}$$

Under the assumption of a homogeneous anisotropic medium, and limiting the frequency dependence only to the first order susceptibility, Maxwell's equations can be reduced to a single vector equation for the electric field $\mathbf{E}(\mathbf{r}, t)$ (the notation $\mathbf{E}_{tt}$ and $\mathbf{P}_{tt}$ denotes the second derivative respect to the temporal coordinate t)

$$\mathbf{E}_{tt} - c^2[\triangle_r \mathbf{E} - \nabla_r(\nabla_r \cdot \mathbf{E})] = -\frac{1}{\varepsilon_0}\mathbf{P}_{tt}. \tag{1.2}$$

Under the assumption that non-linearity dispersion is neglected, the dielectric polarization field components P_j are related to the electric field by:

$$P_j(\mathbf{r}, t) = \varepsilon_0 \int_{-\infty}^{t} \chi_{jn}^{(1)}(t - t_1) E_n(\mathbf{r}, t_1) dt_1 + \varepsilon_0 \chi_{jnm}^{(2)} E_n(\mathbf{r}, t) E_m(\mathbf{r}, t). \tag{1.3}$$

By means of the slowly varying amplitude approximation [1] we can separate the electric field by using three quasi-monochormatic waves (carrier waves) which are modulated by the slowly varying amplitudes $A^{(\alpha)}$, $\alpha = 1, 2, 3$. We also assume that only the wave amplitudes are affected by nonlinear dynamics and that the polarization state vectors $B_j^{(\alpha)}$, $\alpha = 1, 2, 3$ are spatial and time independent. The electric field envelope takes the form:

$$\begin{aligned} E_j(\mathbf{r}, t) =& \eta[A^{(1)}(\xi, \tau) B_j^{(1)} e^{\imath(\mathbf{k}_1 \cdot \mathbf{r} - \omega_1 t)} + A^{(2)}(\xi, \tau) B_j^{(2)} e^{\imath(\mathbf{k}_2 \cdot \mathbf{r} - \omega_2 t)} \\ &+ A^{(3)}(\xi, \tau) B_j^{(3)} e^{\imath(\mathbf{k}_3 \cdot \mathbf{r} - \omega_3 t)}] + c.c. + O(\eta^2), \end{aligned} \tag{1.4}$$

where η is a small perturbative parameter that rescales the spatial coordinate $\xi = \eta \mathbf{r}$ and the time variable $\tau = \eta t$. The wave-number vectors k_1, k_2, k_3, the frequencies ω_1, ω_2, ω_3 and the polarization state vectors $B_j^{(1)}$, $B_j^{(2)}$,

$B_j^{(3)}$ satisfy the following dispersion relation:

$$(\omega^2 - c^2\mathbf{k}\cdot\mathbf{k})B_j + c^2\mathbf{k}\cdot\mathbf{B}k_j + \omega^2\widehat{\chi}_{jn}^{(1)}(\omega)B_n = 0, \tag{1.5}$$

where the function $\widehat{\chi}_{jn}^{(1)}(\omega)$ is the Fourier transform of the linear susceptibility $\chi_{jn}^{(1)}(t)$:

$$\widehat{\chi}_{jn}^{(1)}(\omega) = \int_{-\infty}^{+\infty} e^{-\imath\omega t}\chi_{jn}^{(1)}(t)dt. \tag{1.6}$$

Now, we substitute eq. 1.4 into eq. 1.2 and collecting all terms up to order $O(\eta^2)$ in the expression 1.4, we obtain:

$$\begin{aligned}
\frac{\partial A_1}{\partial\tau} + \mathbf{v}_1\cdot\nabla_\xi A_1 &= \imath\gamma_1 A_2^* A_3 e^{-\imath\Delta\mathbf{k}z} \\
\frac{\partial A_2}{\partial\tau} + \mathbf{v}_2\cdot\nabla_\xi A_2 &= \imath\gamma_2 A_1^* A_3 e^{-\imath\Delta\mathbf{k}z} \\
\frac{\partial A_3}{\partial\tau} + \mathbf{v}_3\cdot\nabla_\xi A_3 &= \imath\gamma_3 A_1 A_2 e^{\imath\Delta\mathbf{k}z}
\end{aligned} \tag{1.7}$$

These coupled equations are derived assuming a resonant interaction between the three waves such as $\omega_1 + \omega_2 = \omega_3$. The vectors $\mathbf{v}_1$, $\mathbf{v}_2$, $\mathbf{v}_3$ are the group velocities of the three carrier waves, while the nonlinear coefficients γ_1, γ_2, γ_3 are function of the wave numbers, and of the linear and quadratic susceptibility coefficients $\chi_{jn}^{(1)}$ and $\chi_{jnm}^{(2)}$. The term $\Delta\mathbf{k}$ represents the phase mismatch per length unit and is defined as:

$$\Delta\mathbf{k} = \mathbf{k}_1 + \mathbf{k}_2 - \mathbf{k}_3. \tag{1.8}$$

The maximum conversion efficiency is obtained through the exact phase matching between the three waves:

$$\mathbf{k}_1 + \mathbf{k}_2 = \mathbf{k}_3 \tag{1.9}$$

The system of equations 1.7 represents a full three dimensional three-waves resonant interaction that has been largely investigated by Kaup [2]. To study the time-dependent solution of eq. 1.7, we assume that the three

amplitudes A_1, A_2, A_3 are function of two independent variables ξ and τ for space and time respectively. Now, we transform amplitudes and coordinates so as to display the coefficients δ_1, δ_2, δ_3 which are proportional to the inverse of the group velocities, and we set the coupling constants equal to unit, $\gamma_\alpha = 1$. In such a way we derive a dimensionless form of eq. 1.7 that is useful for the analysis of particular solutions presented in the next sections:

$$\begin{aligned}
\frac{\partial A_1}{\partial \xi} + \delta_1 \frac{\partial A_1}{\partial \tau} &= \imath A_2^* A_3 \\
\frac{\partial A_2}{\partial \xi} + \delta_2 \frac{\partial A_2}{\partial \tau} &= \imath A_1^* A_3 \\
\frac{\partial A_3}{\partial \xi} + \delta_3 \frac{\partial A_3}{\partial \tau} &= \imath A_1 A_2
\end{aligned} \tag{1.10}$$

We take into consideration the three-wave with $\delta_1 < \delta_3 < \delta_2$ [3] in a coordinate system such that $\delta_1 = 0$.

This system of equations is not only of great interest because of its broad applicability, but it exhibits unusual mathematical properties. Indeed it has been demonstrated [4] that this system of equations is an integrable Hamiltonian system which can be solved by the spectral methods of soliton theory both in the class of bright solitons (when light intensity reaches a maximum value at the centre of the soliton and it decays to zero in the asymptotic regions) and dark solitons (light intensity has a minimum at the center of the soliton and a nonvanishing constant asymptotic regions). Another important point is that eq. 1.10 posses an infinite number of conservation laws and explicit known solutions [5–7].

1.2 Quadratic solitons

In physics, the term "soliton" is currently used as synonymous of a solitary wave that propagates without deformation in a nonlinear and dispersive media. This particular propagation comes from the perfect balance between nonlinear and linear effects. In optics, we can identify two main categories of solitons:

- quadratic solitons, where the nonlinear effects come from the second-order susceptibility $\chi^{(2)}$;

- Kerr solitons, where the nonlinear effects come from the third-order susceptibility $\chi^{(3)}$.

These solitons may exist in time and space domains. Temporal solitons may result from the balance between dispersion and nonlinearity, whereas spatial solitons may arise from the compensation of diffraction with nonlinearity. Solitons may also involve several spectral regions. Here we want to focus our attention to the case of quadratic solitons, which are formed by mutual trapping and locking of multiple-frequency waves. The simplest case correspond to the process of second harmonic generation (SHG) where a fundamental wave and its second-harmonic are able to compensate diffraction effects [8–10]. The resulting soliton contains both the fundamental and second harmonic fields, for this reason they are intrinsically multicolor entities. One of the properties of quadratic solitons is the energy sharing between the multicolor beams, depending on the total energy and the existing material wave-vector mismatch [11].
The first demonstration, of such a kind of solitons, was carried out by W. Torruellas in 1995 [12, 13]. Torruellas observed a spatial soliton formed by parametric wave interaction (the beam-trapping mechanism was due to the energy exchange between the fundamental and second harmonic component) in crystals with quadratic nonlinearities (KTP crystals), previously predicted by Karamzin and Sukhorukov in the 70s [14]. After this demonstration, several research groups have theoretically studied the mechanisms that allow this regime of propagation, with the introduction of new theoretical concepts. Different families of solutions have been found by Buryak et al. [15, 16]. Moreover, in 1989, Belashenkov demonstrated that, under particular conditions, the propagation of an optical beam in a quadratic medium may be described as the propagation in a medium with third-order nonlinear susceptibility by using the concept of cascad-

ing effects [17, 18]. This concept suggested the existence of much richer families of quadratic solitons.

In recent years, quadratic solitons have been the subject of an intense renewal of interest from experimental and theoretical point of view because of their particle-like behaviour, which enables the coherent energy transport and processing. In the next sections we will focus on two classes of TWRI solitons, that were first predicted by Zakharov and Manakov [4] and Nozaki [19]. These solitary waves result from an energy exchange between dispersionless (or diffractionless) waves of different velocities. The first type of solitons, Zakharov-Manakov solitons (ZM solitons), describes the mixing of three waves that travel with their respective linear group velocity, and interact just for a short time [4, 20–22]. The second type of solitons, also known as simultons, are formed as a result of the mutual trapping of waves at three different frequencies which travel locked together with a common group velocity [19, 23]. Such kind of soliton solution are similar to the well known "walking solitons", where the quadratic solitons are able to counteract the spatial walk-off existing between the multiple signals needed to form the solitons. Nevertheless, the walking solitons, exist in the presence of non-negligible diffraction and group velocity mismatch whereas the simultons exist only with non negligible group velocity mismatch.

1.3 Zakharov-Manakov solitons

Compression and amplification of ultra-short laser pulses during sum-frequency (SF) generation in presence of group velocity mismatch (GVM) was theoretically predicted [24, 25] and observed in several experiments. The temporal collision of two short pulses in a quadratic nonlinear crystal permits to generate a short and time-compressed SF pulse. This kind of collision may lead to the formation of a ZM-soliton. This type of soliton is intrinsically unstable since its energy decays back into the two incident

pulses after a relatively short distance. Let's note that the shapes, intensities and widths of the input pulses are unchanged in spite of their interaction. In figure 1.1 we show a typical example of the ZM-soliton generation

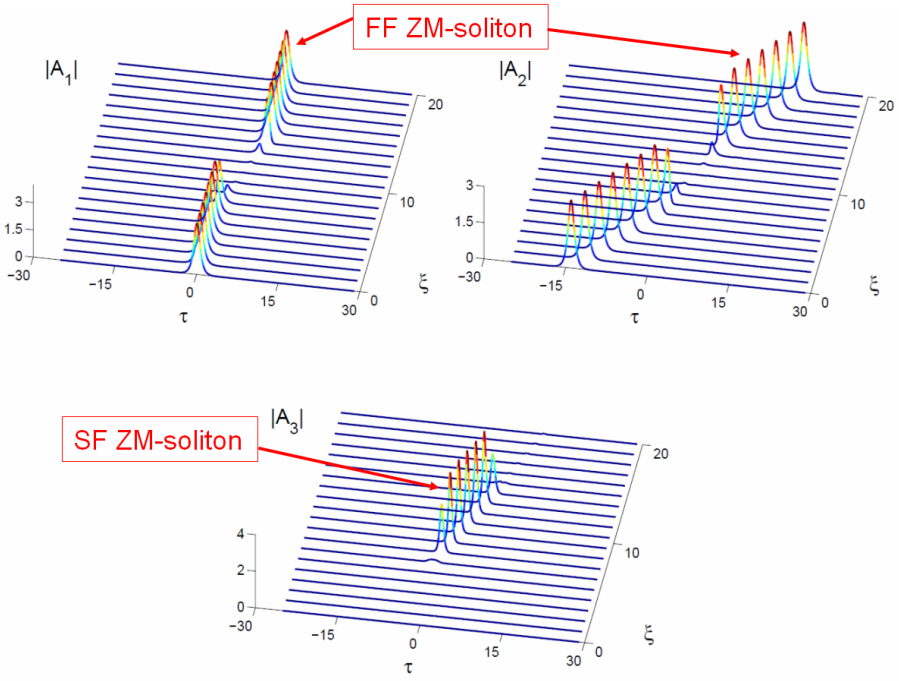

Figure 1.1: Sum-frequency generation at ω_3 from parametric interaction of two short optical signals at ω_1 and ω_2. The normalized delays are $\delta_1 = 0$, $\delta_2 = 2$, $\delta_3 = 1$.

through SF interaction between two optical pulses [26]. In this scenario, whenever the faster pulse A_2 overtakes the slower one A_1, an idler pulse A_3 at the SF is generated and propagates with a velocity given uniquely by the linear part of the susceptibility (named linear velocity). At high intensity the SF pulse generation leads to the formation of a ZM-soliton. Rigorously speaking, the ZM-soliton is composed only by the SF pulse. For further propagation distance the SF wave (ZM-soliton) decays back into the two original isolated ZM-solitons at frequencies ω_1 and ω_2 (see fig. 1.1). These

ZM-solitons are an exact solution of eq. 1.10, and they are defined as:

$$\begin{aligned} A_1 &= -\imath\frac{\Delta}{4p}\frac{\delta_2-\delta_3}{\delta_2\delta_3}A_2^*A_3, \\ A_2 &= \imath\frac{4p\delta_3}{\Delta}\sqrt{\frac{\delta_2}{\delta_2-\delta_3}}e^{\imath q_2\tau_2}exp\left[-2\imath\frac{\delta_3}{\delta_2-\delta_3}(k-\imath p)\tau_2\right], \\ A_3^* &= \imath\frac{4p\delta_2}{\Delta}\sqrt{\frac{\delta_3}{\delta_2-\delta_3}}e^{\imath q_3\tau_3}exp\left[2\imath\frac{\delta_2}{\delta_2-\delta_3}(k+\imath p)\tau_3\right], \end{aligned} \tag{1.11}$$

where

$$\begin{aligned} \Delta &= 1+exp\left(-\frac{4p\delta_3}{\delta_2-\delta_3}\tau_2\right)+exp\left(-\frac{4p\delta_2}{\delta_2-\delta_3}\tau_3\right), \\ q_n &= q(\delta_{n+1}-\delta_{n+2}), \quad n=1,2,3mod(3), \\ \tau_n &= -\tau+\delta_n\xi. \end{aligned} \tag{1.12}$$

For a given choice of the linear group velocities, the ZM-soliton is identified by three parameters p, k, q. The parameter p is associated with the re-scaling of the wave amplitudes, and the coordinates τ and ξ. The value of k and q adds a linear phase shift in τ and ξ.

The ZM-soliton is then generated under perfect conditions for SF generation i.e. with a perfect walk-off compensation between initial waves. The decay of the SF pulse which is shown in fig. 1.1 appears at a given nonlinear crystal length depending on the input pulses characteristics. This limited time of existence can be a significant drawback for applications. The temporal duration of the SF pulse is reduced with respect to the input pulse widths, depending on the time widths and intensities of the input pulses.

1.4 Simultons

In this section we introduce the concept of simulton. We limit our explanation to the simplest case of SF generation. Indeed, in the presence of GVM, the parametric SF conversion with a pulsed signal and a quasi-CW pump generally leads to the generation of an idler pulse with low intensity, whose duration is associated to the interaction distance in the crystal. By

increasing the input intensity, we obtained the sum frequency generation with the compensation of the GVM between all of the waves representing the simultonic solution. Figure 1.2 illustrates the generation of a simulton from the parametric SF conversion of an optical signal and a CW background control wave with an arbitrary intensity level. We injected in the quadratic nonlinear crystal a short signal A_2 at frequency ω_2, with a delayed and relatively long pump-control pulse A_1 at frequency ω_1. The SF

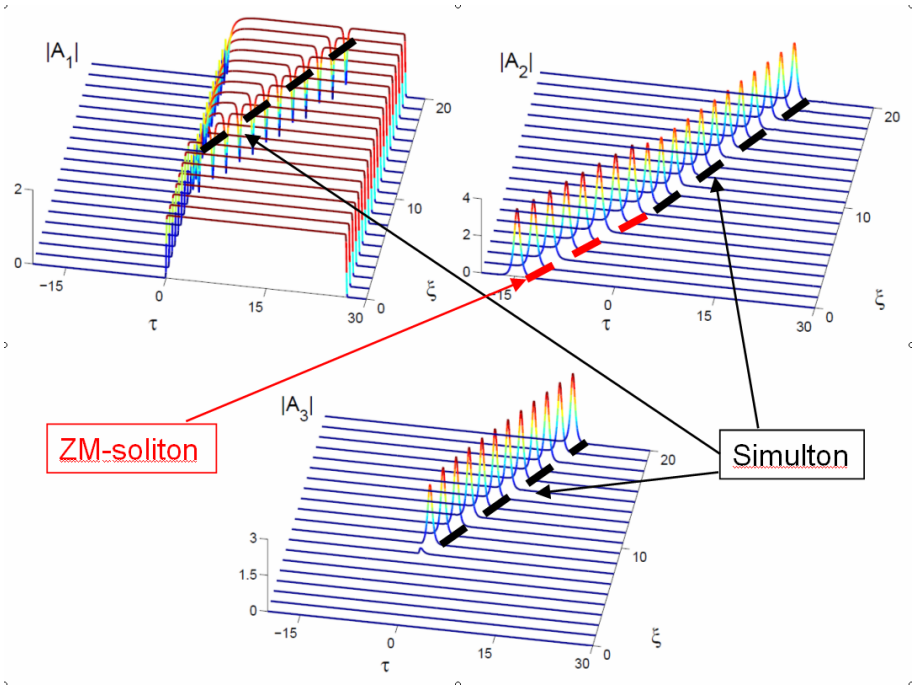

Figure 1.2: Simulton generation at ω_3 from parametric interaction of a short pulse at ω_2 and quasi-CW control at ω_1. The normalized delays are $\delta_1 = 0$, $\delta_2 = 2$, $\delta_3 = 1$.

process displayed in fig. 1.2 leads to stable generation of a simulton in both time and space domain.

When the faster pulse A_2 at ω_2 recover its initial delay and overtakes the quasi-CW background A_1 at ω_1 (at $\tau = 0$, in fig. 1.2), their collision leads to the generation of a short idler pulse A_3 at the SF ω_3, and a depletion is observed on the quasi-CW wave at ω_1. Additionally, the propagation speed, the intensity and duration of the input wave A_2 are modified. By following

the notation of eq. 1.10, the simulton solution is:

$$\begin{aligned} A_1 &= \{1+\frac{2pb^*}{|b|^2+a^2}[1-tanh[B(-\tau+\delta\xi)]]\}\frac{\imath a g_1 exp(\imath q_1\tau_1)}{g(\delta_2-\delta_3)},\\ A_2 &= \frac{2pa}{\sqrt{|b|^2+a^2}}\frac{g_2}{g(\delta_2-\delta_3)}\frac{exp[\imath(q_2\tau_2+\chi\tau+\omega\xi)]}{cosh[B(-\tau+\delta\xi)]},\\ A_3 &= \frac{2pb^*}{\sqrt{|b|^2+a^2}}\frac{g_3}{g(\delta_2-\delta_3)}\frac{exp[-\imath(q_3\tau_3+\chi\tau+\omega\xi)]}{cosh[B(-\tau+\delta\xi)]}, \end{aligned} \tag{1.13}$$

where

$$\begin{aligned} b=(Q-1)\left(p+\frac{\imath k}{Q}\right),\ r=p^2-k^2-|a|^2,\\ Q=\frac{1}{p}\sqrt{\frac{1}{2}\left[r+\sqrt{r^2+4k^2p^2}\right]},\\ B=\frac{p\delta_2+\delta_3-Q(\delta_2-\delta_3)}{\delta_2-\delta_3},\\ \delta=\frac{2\delta_2\delta_3}{\delta_2+\delta_3-Q(\delta_2-\delta_3)},\\ \chi=\frac{k\left(\delta_2+\delta_3-\frac{\delta_2-\delta_3}{Q}\right)}{\delta_2-\delta_3},\\ \omega=\frac{-2k\delta_2\delta_3}{\delta_2-\delta_3},\ \tau_n=-\tau+\delta_n\xi,\\ q_n=q(\delta_{n+1}-\delta_{n+2}),\ g_n=|(\delta_n-\delta_{n+1})(\delta_n-\delta_{n+2})|^{-1/2},\\ g=g_1g_2g_3,\ n=1,2,3mod(3). \end{aligned} \tag{1.14}$$

The simulton is then composed by two bright pulses at ω_2 and ω_3 plus a dark pulse all of them running with a common speed δ.

For a given choice of the linear group velocities, the simulton is identified by four parameters p, a, k, q. The parameter p is associated with the re-scaling of the wave amplitudes, and coordinates τ and ξ. Whereas the parameter a measures the amplitude of the CW background of wave A_1 (namely $a\sqrt{\delta_2\delta_3}$). The value of k is related to the soliton wavenumber. The parameter q adds a linear phase shift in both τ and ξ (see [21] for details). We may describe the initial wave A_2 as a single ZM-soliton [4], which interaction with the quasi-CW generates a simulton or in this assumption a stable TWRI simulton [21]. So, we may analytically predict the parameter p, k, q, a of the generated TWRI simulton from the corresponding parame-

ters of the initial ZM-soliton:

$$A_1 = 0,\ A_2 = 2P\sqrt{\rho\delta_2\delta_3}\frac{e^{\imath\rho\phi\tau_2}}{cosh(2P\rho\tau_2)},\ A_3 = 0, \tag{1.15}$$

where

$$\rho = \frac{\delta_3}{\delta_2 - \delta_3},\ \tau_2 = -\tau + \delta_2\xi. \tag{1.16}$$

For a given choice of the three linear group velocities, or characteristic delays δ_j, the above ZM-soliton is determined in terms of the two real parameters P, ϕ. The parameter P is always positive and fixes both the soliton peak amplitude and its temporal width. Whereas the parameter ϕ corresponds to a phase shift which is linear in both τ and ξ coordinates. On the other hand, the quasi CW wave at frequency ω_1 can be described by

$$A_1 = \frac{Ce^{-\imath\gamma\tau}}{2}\left[tanh\left(\frac{\tau-\tau_i}{\tau_r}\right) - tanh\left(\frac{\tau-\tau_f}{\tau_r}\right)\right],\ A_2 = 0,\ A_3 = 0, \tag{1.17}$$

where C is the complex amplitude and γ is the frequency shift with respect to the quasi-CW signal A_1; τ_i (τ_f) and τ_r are the switch-on (switch-off) time and the rise/fall time of the quasi-CW signal, respectively (see fig. 1.3). We consider the case for which $|C|^2 < P^2\delta_2\delta_3$. We suppose that the initial ZM

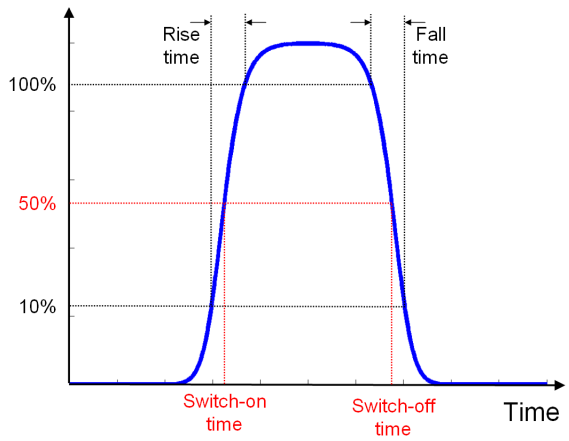

Figure 1.3: Definition of rise/fall, switch-on and switch-off time for the case of quasi-CW signals.

soliton (wave A_2) adiabatically (i.e., without emission of radiation) reshapes into a simulton after its collision with the quasi-CW pump at a given point in time (say, at $\tau = 0$), and hence:

- the energy of the initial ZM soliton (wave A_2) is conserved in the generated simulton;

- the phase of initial ZM soliton (wave A_2) and the generated simulton are continuous across their time interface (at $\tau = 0$, where A_2 reshapes into a simulton);

- the amplitude and phase of the control pump C are properly chosen to obtain simultonic propagation.

If we consider the above three conditions, we obtain the following relations that connect the parameters of the incident ZM soliton and those of the transmitted simulton:

$$p = P,\ a\sqrt{\delta_2\delta_3} = |C|,\ q(\delta_2 - \delta_3) = \gamma,\ q(\delta_2 - \delta_3) - 2k = \phi, \tag{1.18}$$

with $|C| < P\sqrt{\delta_2\delta_3}$.
The important consequence of this result is that we may analytically predict and control the characteristic of the generated idler pulse at ω_3 (namely, its velocity, time duration and energy) simply with the intensity level of the CW pump. It is important to underline that the stability of the generated simulton is ensured by the stability of the whole SF idler conversion process [27]. Simultons represent an entirely new family of quadratic solitons, indeed the most remarkable physical property is that their speed can be continuously varied by means of adjusting the energy of the two short pulses (A_2 and A_3).

1.5 Phase matching

The efficiency of the conversion processes described by eq. 1.7 strongly depends on the parameter Δk. Indeed by integrating the third equation of eq. 1.7 on the length L of the dielectric structure, and by neglecting losses at frequencies ω_1 and ω_2, we obtain an intensity relation between the three waves (eq. 1.19).

$$I^{\omega_3}(z=L) \propto aI^{\omega_1}(z=0)I^{\omega_2}(z=0)sinc^2\left(\frac{\Delta kL}{2}\right). \tag{1.19}$$

The efficiency is maximum for $\Delta k = 0$, when the photon momentum is conserved. We can reformulate such condition in the following way:

$$\begin{aligned} k(\omega_3) &= k(\omega_1) + k(\omega_2), \\ \omega_3 &= \omega_1 + \omega_2. \end{aligned} \tag{1.20}$$

These conditions can not be simultaneously satisfied in an isotropic medium due to the frequency dependence of the refractive index (or the wavevector). For this reason, in our experimental work, we exploit the natural birefringence of a given crystal to reach the phase matching conditions of eq. 1.20. This technique uses the anisotropy of the material for compensating the dispersion of refractive index. To satisfy the condition of velocity matching, which ensures the conversion process, we set the linear polarization states of the incident waves along the main crystal axis.
We call collinear phase matching whenever eq. 1.20 is satisfied by waves propagating in the same direction. Differently, when waves have different propagation directions, the phase matching is non-collinear. Another technique commonly called quasi phase matching (QPM) uses a periodic dielectric structures, to compensate the phase mismatch between the interacting wave. In this thesis, only the non-collinear phase matching method will be considered.

Bibliography

[1] A. Degasperis, "Multiscale expansion and integrability of dispersive wave equations," in *Integrability* (A. Mikhailov, ed.), vol. 767, pp. 215–244, Berlin, Heidelberg: Springer Berlin Heidelberg, 2009.

[2] D. Kaup, "The solution of the general initial value problem for the full three dimensional three-wave resonant interaction," *Physica D: Nonlinear Phenomena*, vol. 3, pp. 374–395, July 1981.

[3] D. Kaup, A. Reiman, and A. Bers, "Space-time evolution of nonlinear three-wave interactions. i. interaction in a homogeneous medium," *Reviews of Modern Physics*, vol. 51, pp. 275–309, Apr. 1979.

[4] V. Zakharov and S. Manakov, "Resonant interaction of wave packets in nonlinear media," *Sov. Phys. JETP Lett.*, vol. 18, pp. 243–245, 1973.

[5] D. Kaup, A. Reiman, and A. Bers, "Space-time evolution of nonlinear three-wave interactions. i. interaction in a homogeneous medium," *Reviews of Modern Physics*, vol. 51, pp. 275–309, Apr. 1979.

[6] F. Calogero and A. Degasperis, "New integrable equations of nonlinear Schrödinger type," *Studies in Applied Mathematics*, vol. 113, pp. 91–137, July 2004.

[7] A. Degasperis, M. Conforti, F. Baronio, and S. Wabnitz, "Stable control of pulse speed in parametric Three-Wave solitons," *Physical Review Letters*, vol. 97, Aug. 2006.

[8] L. Torner, "Stationary trapping of light beams in bulk second-order nonlinear media," *Optics Communications*, vol. 121, pp. 149–155, Dec. 1995.

[9] A. Buryak, Y. Kivshar, and V. Steblina, "Self-trapping of light beams and parametric solitons in diffractive quadratic media," *Physical Review A*, vol. 52, pp. 1670–1674, Aug. 1995.

[10] L. Torner and E. Wright, "Soliton excitation and mutual locking of light beams in bulk quadratic nonlinear crystals," *Journal of the Optical Society of America B*, vol. 13, p. 864, May 1996.

[11] L. Torner, "Stationary solitary waves with second-order nonlinearities," *Optics Communications*, vol. 114, pp. 136–140, Jan. 1995.

[12] W. Torruellas, Z. Wang, D. Hagan, E. VanStryland, G. Stegeman, L. Torner, and C. Menyuk, "Observation of Two-Dimensional spatial solitary waves in a quadratic medium," *Physical Review Letters*, vol. 74, pp. 5036–5039, June 1995.

[13] R. Schiek, Y. Baek, and G. Stegeman, "One-dimensional spatial solitary waves due to cascaded second-order nonlinearities in planar waveguides," *Physical Review E*, vol. 53, pp. 1138–1141, Jan. 1996.

[14] Y. Karamzin and A. Sukhorukov, "Mutual focusing of high-power light beams in media with quadratic nonlinearity," *Sov. Phys. JETP*, vol. 41, pp. 414–420, 1976.

[15] A. Buryak, "Solitons due to second harmonic generation," *Physics Letters A*, vol. 197, pp. 407–412, Feb. 1995.

[16] D. Pelinovsky, A. Buryak, and Y. Kivshar, "Instability of solitons governed by quadratic nonlinearities," *Physical Review Letters*, vol. 75, pp. 591–595, July 1995.

[17] C. Clausen, O. Bang, and Y. Kivshar, "Spatial solitons and induced kerr effects in Quasi-Phase-Matched quadratic media," *Physical Review Letters*, vol. 78, pp. 4749–4752, June 1997.

[18] N. Belashenkov, S. Gagarskii, and M. Inochkin, "Nonlinear refraction of light on second-harmonic generation," *Opt. Spectrosc. (USSR)*, vol. 66, p. 1383, 1989.

[19] K. Nozaki and T. Taniuti, "Propagation of solitary pulses in interactions of plasma waves," *Journal of the Physical Society of Japan*, vol. 34, pp. 796–800, Mar. 1973.

[20] J. Armstrong, S. Jha, and N. Shiren, "Some effects of group-velocity dispersion on parametric interactions," *IEEE Journal of Quantum Electronics*, vol. 6, pp. 123–129, Feb. 1970.

[21] A. Degasperis and S. Lombardo, "Exact solutions of the 3-wave resonant interaction equation," *Physica D: Nonlinear Phenomena*, vol. 214, pp. 157–168, Feb. 2006.

[22] D. Kaup, "The Three-Wave Interaction - A nondispersive phenomenon," *Stud. Appl. Math.*, vol. 55, pp. 9–44, 1976.

[23] Y. Ohsawa and K. Nozaki, "Propagation of solitary pulses in interactions of plasma waves. II," *Journal of the Physical Society of Japan*, vol. 36, pp. 591–595, Feb. 1974.

[24] Y. Wang and R. Dragila, "Efficient conversion of picosecond laser pulses into second-harmonic frequency using group-velocity dispersion," *Physical Review A*, vol. 41, pp. 5645–5649, May 1990.

[25] A. Stabinis, G. Valiulis, and E. Ibragimov, "Effective sum frequency pulse compression in nonlinear crystals," *Optics Communications*, vol. 86, pp. 301–306, Nov. 1991.

[26] E. Ibragimov and A. Struthers, "Second-harmonic pulse compression in the soliton regime," *Optics Letters*, vol. 21, p. 1582, Oct. 1996.

[27] F. Baronio, A. Degasperis, S. Wabnitz, and M. Conforti, "Inelastic scattering and interactions of Three-Wave parametric solitons," *Phys-*

ical Review E - Statistical, Nonlinear and Soft Matter Physics, vol. 74, no. 6 Pt 2, p. 065602, 2006.

CHAPTER 2

Experimental study on Zakharov Manakov soliton and simulton generation

Contents

Here we present the experimental demonstrations for the first time of our knowledge of the existence of ZM solitons and simultons. These experiments were carried out at the beginning of my PhD. Such kind of solitons result from the energy exchange between waves with different velocities in the limit where diffraction is negligible. In this case the nonlinear effect may balance the spatial walk-off between the interacting waves.

The first important step was to define the general conditions for observing both phenomena and to identify a suitable optical medium allowing these nonlinear propagations.

In this chapter we first present the result concerning the solution given in eq. 1.11 and then the simulton solution as expressed in eq. 1.13. The last section of this chapter is denoted to a practical application onto

new mode-locking technique. The experimental results will be compared with numerical simulations. The theoretical results have been obtained in strong collaboration with Matteo Conforti and Fabio Baronio, two researchers from the University of Brescia, Italy.

2.1 General conditions

To obtain the experimental conditions suitable for soliton and simulton propagation, we determined several parameters regarding:

- the laser source;
- the quadratic nonlinear crystal;
- the SF conversion process.

The observation of the solitonic and simulton propagation required relatively high pulses intensity, so we opted for a Q-Switched mode-locked Nd:YAG laser source. The mode-locking operation is assured by a semiconductor Bragg mirror (SESAM) acting as an ultrafast saturable absorber. Such laser delivers a train of pulses, 40 ps wide, with a gaussian shape and a central wavelength of 1064 nm. A Pockels cell selects the more powerful pulse out of a train of them. Such pulse is then amplified by a single-pass amplifier. This pulse is used as a source of our experiments.
In all experiments, we considered second-harmonic generation (SHG) process which is a particular case of SF conversion in which the two initial beams have the same frequency $\omega = \omega_1 = \omega_2$.
We choose a potassium titanyl phosphate ($KTiOPO_4$), or KTP crystal. KTP crystals are commonly used in frequency doubling process owing to their high nonlinear coefficient ($d_{eff} \sim 3\, pm/V$), wide transparency window (from 350 to 2700 nm), broad angular and spectral acceptances ($\sim$20 $mrad\,cm$ and $\sim$6 cm respectively). In particular, these crystals are suitable for SHG because their conversion efficiency is rather good (80%) and their damage

threshold is high ($\sim 15\ J/cm^2$). The KTP that we used is a type II nonlinear crystal exhibiting extraordinary and ordinary axes. The crystal excitation is realised on both axes whereas the second harmonic wave is obtained with polarisation vectors parallel to the extraordinary axis.

Remembering the resonant condition presented in eq. 1.9 and the characteristics of each beam velocity, we choose to use a spatial non-collinear geometry. It consists of exciting the crystal with two beams at the funda-

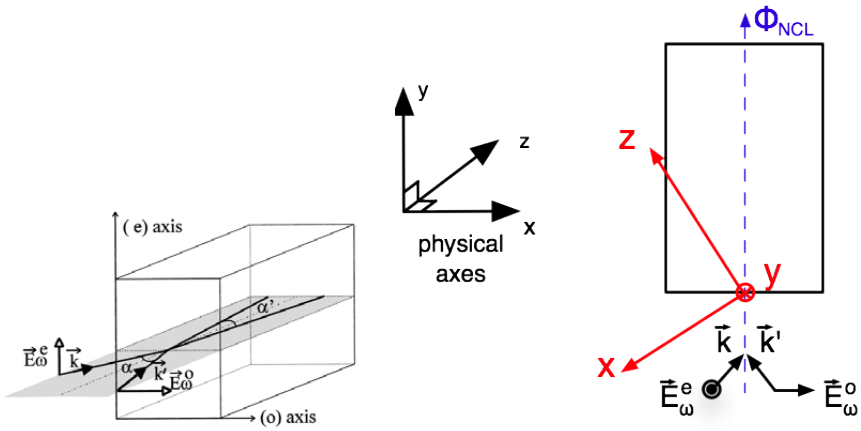

(a) (b)

Figure 2.1: Schematic representation of input conditions on KTP crystal: a) representation of the optical non collinear TWRI interaction; b) orientation of physical axes of KTP with respect to the propagation direction.

mental frequency with orthogonal polarization state aligned on the neutral crystal axes (see fig. 2.1(a)). The two beams propagate inside the crystal with its linear velocities and forming an angle α' between them, defined by

$$\alpha' = \frac{\alpha}{2}\left(\frac{1}{n^e} + \frac{1}{n^0}\right). \tag{2.1}$$

The non-collinear type II interaction between the fundamental beams of type (o) and (e) gives rise to a SH on the direction ϕ^{NCL} defined by the vector sum $\mathbf{k}^{\mathbf{o}}_{\omega} + \mathbf{k}^{\mathbf{e}}_{\omega}$. In this direction the wave vector for SH is $\mathbf{k}^{\mathbf{e}}_{\mathbf{2}\omega} = \frac{\mathbf{2}\pi}{\lambda}\mathbf{n}^{\mathbf{e}}_{\mathbf{2}\omega}(\phi^{\mathbf{NCL}})$, where $n^e_{2\omega}(\phi^{NCL})$ is the refractive index for the SH defined by the direction

ϕ^{NCL}. The phase matching condition reads as:

$$\Delta \mathbf{k}^{\mathbf{NCL}} = \mathbf{k}^{\mathbf{o}}_{\omega} + \mathbf{k}^{\mathbf{e}}_{\omega} - \mathbf{k}^{\mathbf{e}}_{\mathbf{2}\omega} = \mathbf{0} \tag{2.2}$$

In our spatial non-collinear scheme, the spatial walk-off of each wave corresponds to a spatial velocity represented by an angle formed by the direction of propagation and the phase matching direction (see Fig. 2.2). In that configuration the condition of simulton existence on the time delays $\delta_1 < \delta_3 < \delta_2$ in eq. 1.10 is transformed into the following condition on the spatial velocities $V_2 < V_3 < V_1$, which is perfectly respected.

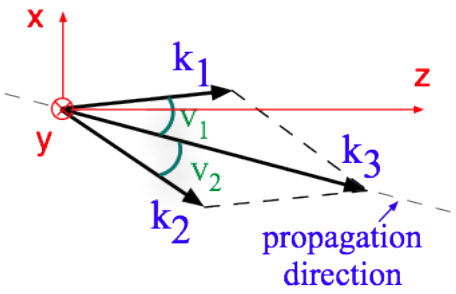

Figure 2.2: Representation of spatial walk-off of the three waves with respect to the physical axes of the crystal (red). In this case $V_3 = 0$.

2.2 Zakharov Manakov solitons by using SHG

2.2.1 Experimental setup

The experimental setup used in these experiments is presented in fig. 2.3. The laser beam diameter at the input face of the crystal exhibits a 300 μm diameter measured at full width half maximum of intensity (FWHMI) and obtained by a spatial telescope made by two lens L_1 and L_2. The diaphragm placed between L_1 and L_2 ensures a spatial unimodal Gaussian shape of the input beam. The total intensity of the beam is controlled by an attenuator composed by a half-wave plate and a Glan polarizer. After the light has passed through a second attenuator, we obtain two

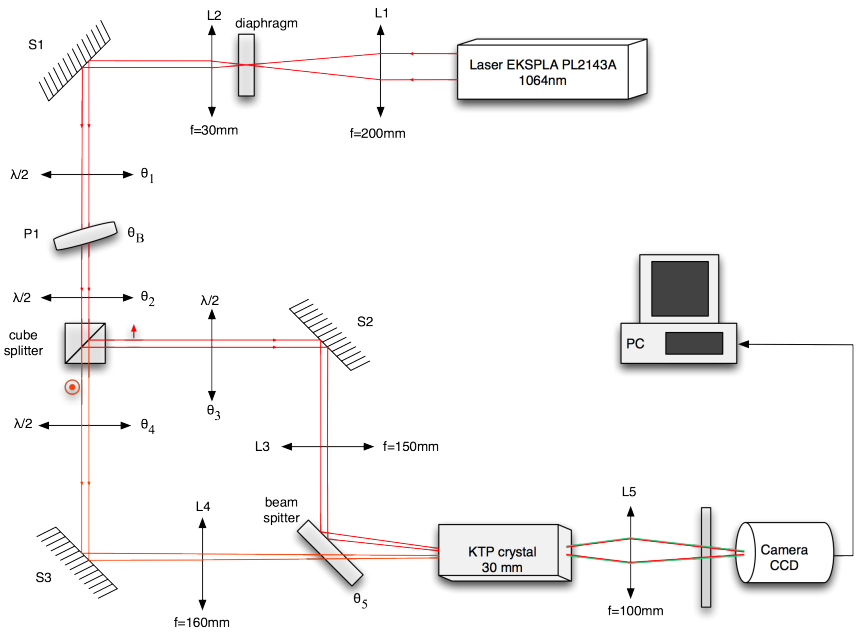

Figure 2.3: Experimental setup used to study ZM soliton propagation obtained under sum-frequency process in a type II crystal.

independent beams with orthogonal linearly polarized states. A half-wave plate placed before the polarizer P_1 and before the prism serves to adjust the total intensity of the beam and the intensity balance between the two beams. By means of two highly reflecting mirrors, a beam splitter and lens L_3 and L_4, both beams are focused and spatially superimposed in the plane of their beam waist with a circular shape of 120 μm width FWHMI. An interferometric scheme is used to temporally superimpose the two beams. A 3 cm long type II KTP crystal cut for SHG is positioned such that its input face coincides with the plane of superposition of the two input beams. The crystal was oriented for perfect non-collinear phase matching. The direction of the linear polarization state of the two beams are adjusted to coincide with the ordinary and the extraordinary axes of the KTP crystal. The wave vectors of the input fields were tilted at angles of $\theta_1 = 0.7\,\mathrm{deg}$ and $\theta_2 = -0.7\,\mathrm{deg}$ (in the crystal) with respect to the direction of perfect collinear phase matching for the extraordinary and ordinary components, respectively. Inside the crystal these parameters corresponded to a tilt

between the input beams equal to 3.7 times the natural spatial walk-off which is introduced along the ordinary noncritical plane. The direction of the sum frequency wave vector lies in between the input waves directions. In these conditions, the spatial diffraction, temporal dispersion and GVD can be neglected. The condition $V_2 < V_3 < V_1$ between the waves E^o_ω, $E^e_{2\omega}$ and E^e_ω is also satisfied. The spatial waves' patterns at the output of the crystal were imaged with magnification onto a CCD camera and analysed. We alternately used different filters and polarizers to select either the IR or green output.

2.2.2 Experimental observation

All the results that we present here have been obtained under the same conditions of incidence angle, polarization states of each beams and phase matching. Only the incident intensities are modified. In tab. 2.1 we report the intensities calculated from the measured energy at the input and output faces of the crystal for the fundamental beams and the SH beam, respectively. The energy meter error rate is close to 10%.

test number	$\mathbf{I^o_\omega[MW/cm^2]}$	$\mathbf{I^e_\omega[MW/cm^2]}$	$\mathbf{I^e_{2\omega}[MW/cm^2]}$
1	3.36	3.97	0
2	9.37	11.10	0.15
3	10.90	14.40	0.23
4	55.60	69.00	1.52
5	182.00	236.00	7.38
6	1210.00	1580.00	67.60
7	7110.00	6960.00	212.00
8	8030.00	8360.00	243.00

Table 2.1: Calculated intensities of the input beams, A_1 and A_2 @1064 nm, and the third beam A_3 @532 nm.

For an accurate analysis of the measurements we compare the experimental data with the parabolic function that defines the relation between the input intensities and the generate SH intensity for the case of a weak

nonlinear regime (see fig. 2.4):

$$I^e_{2\omega} = a * L^2 I^e_\omega * I^o_\omega \tag{2.3}$$

where L is the distance of propagation and a is a function which depends on the refractive indexes, the frequency ω and the nonlinear response of the medium.

In the first test the input intensities are too low to excite a nonlinear process, so we do not observe a non-collinear SHG process. We identify the same behaviour from the analysis of the recorded spatial output profile of the extraordinary polarized wave at the sum frequency 2ω, the profile of the extraordinary polarized component and the profile of the ordinary polarized component at frequency ω (fig. 2.5 and fig. 2.6). Fig. 2.6(a)

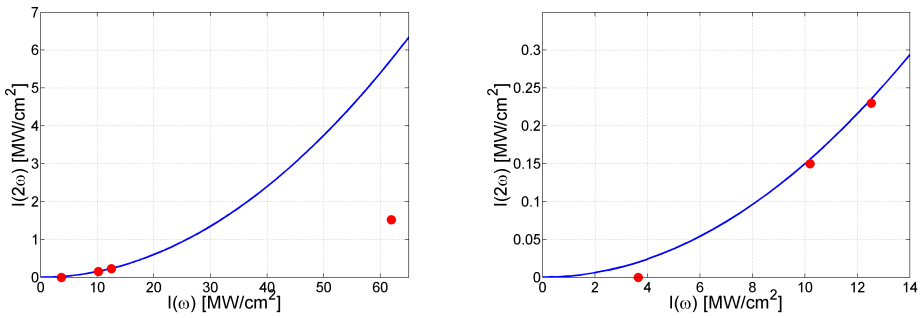

(a) (b)

Figure 2.4: a) Theoretical curve (blue) compared with experimental measurement (red point), b) zoom for low input intensities.

shows the waves E^e_ω and E^o_ω, overlapped at the crystal entrance, spatially separated at the crystal output because of linear spatial walk-off in the ordinary plane. For low intensity (fig. 2.5(a)) no component at frequency 2ω is observed. At moderate input intensities, the experimental data agree with the theoretical prediction (see fig. 2.4(b)). At the output face of the crystal we observe that the fundamental components are spatially separated and a weak SH component, whose position lies in between the out-

put position of the two fundamental waves. The generated SH has the same spatial profile as those of the fundamental waves, when increasing the input intensities, the experimental measurements of the SH intensity do not follow the standard quadratic evolution (fig. 2.4(b)). This discrep-

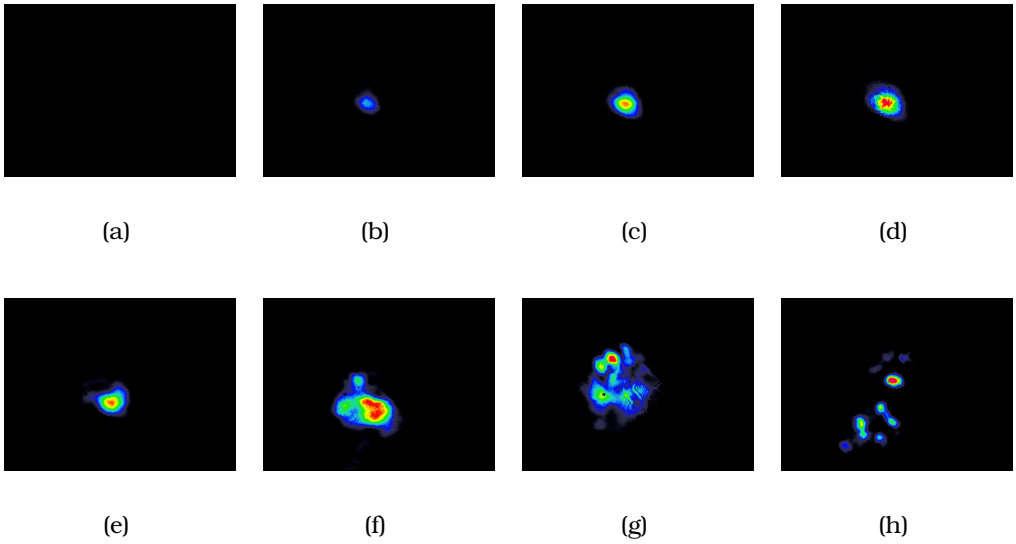

Figure 2.5: Evolution of the generated SH wave for different input intensities corresponding to the test (a) # 1, (b) # 2, (c) # 3, (d) # 4, (e) # 5, (f) # 6, (g) # 7, (h) # 8.

ancy arises from the fact that eq. 2.3 is not suitable in a strong nonlinear regime (fig. 2.5(e)). Additionally, we note the presence of a spatial deformation of the SH component. Such a distortion is more evident when we increase the input intensities (fig. 2.5(h)). This spatial deformation cannot be explained by the well know SHG theory, which only predicts saturation of the nonlinear conversion. Moreover, we observed the apparition of two well defined ordinary and extraordinary fundamental waves E^e_ω and E^o_ω, which turned out to be spatially shifted with respect to the initial fundamental components (fig. 2.6(h)).

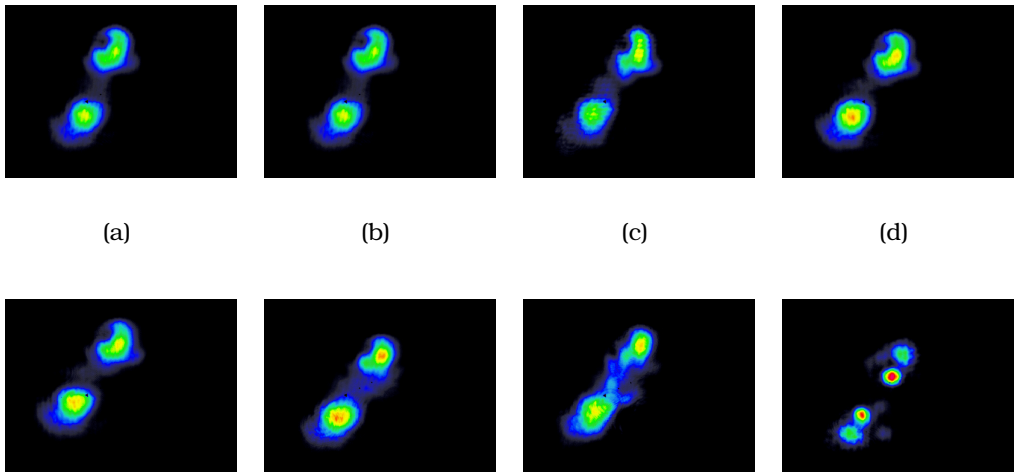

Figure 2.6: Evolution of the FF waves for different input intensities corresponding to the test (a) # 1, (b) # 2, (c) # 3, (d) # 4, (e) # 5, (f) # 6, (g) # 7, (h) # 8.

2.2.3 Discussion

In the last section we identified three different regime of propagation depending on the input intensities. For low intensities (I=$3MW/cm^2$) the input waves do not interact and propagate in absence of noticeable diffraction in the KTP crystal, following their own characteristic velocities V_1 and V_2 (fig. 2.7). At moderate input intensity (I=$10MW/cm^2$), the beams at frequency ω interact and generate a steady field at the sum frequency 2ω.

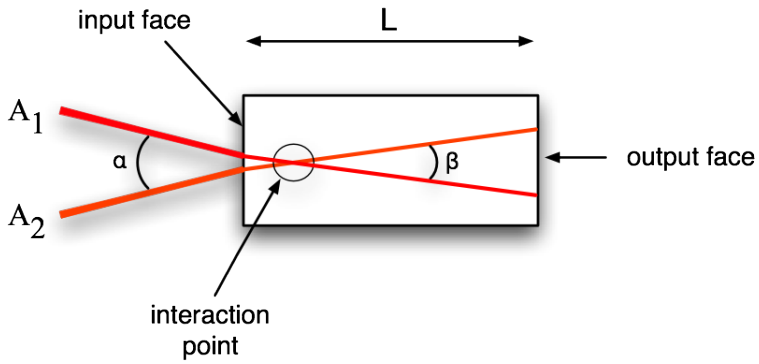

Figure 2.7: Linear interaction between two fundamental beams.

When the faster wave overtakes the slower one, we observe an energy conversion to the sum frequency wave A_3; next the three waves propagate alone with their own characteristic velocities (see fig. 2.8). At high input intensity (I=$0.2GW/cm^2$), the beams at frequency ω interact and generate a field at the sum frequency 2ω. Each input wave split into a linear component, travelling at its own linear velocity, and a nonlinear component that takes part in the formation of a TWRI soliton. The observation of the two new spatially shifted waves provides a clear evidence that a TWRI soliton is generated at the sum frequency inside the crystal: the sum frequency wave has enough energy to sustain at least one soliton. Such soliton has subsequently decayed into two solitons at the fundamental wavelength right before the end face of the crystal (fig. 2.9(a)). In that configuration,

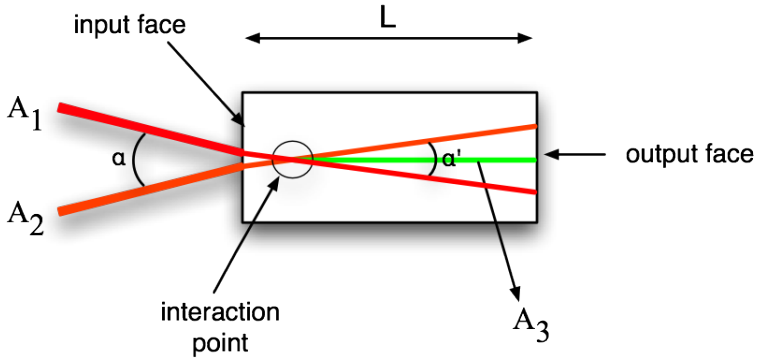

Figure 2.8: Non collinear SHG.

the second harmonic wave is strongly depleted because of a non collinear difference frequency process. By removing the attenuation filters used to protect the camera, the deformation observed on the SH beam is a component generated mainly through type I SHG by the extraordinary and ordinary waves at ω (fig. 2.9(b).

Now it is interesting to interpret the result by the inverse scattering transform (IST) which allows certain nonlinear problems to be treated by what are essentially linear methods [1–3]. In particular, this method allows to decompose a given solution of the partial differential equation (PDE) in its continuum spectrum component (radiation) and in discrete spectrum

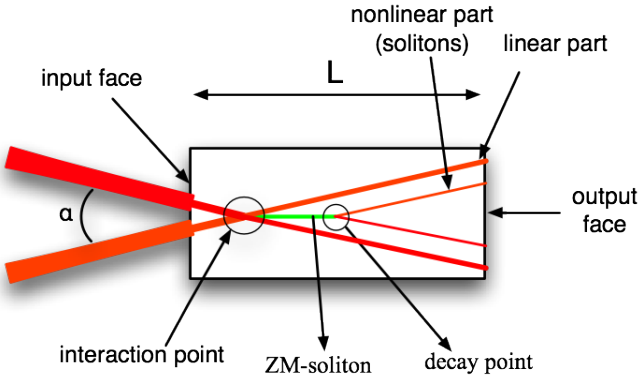

(a)

(b)

Figure 2.9: (a) spatial representation of the propagation of the three waves in the $x-z$ plane and (b) experimental output profile of E_ω for I=$0.2GW/cm^2$ (left) and $E_{2\omega}$ (right).

component (solitons). From a IST point of view, the input waves contain one soliton each plus radiation. The solitons in the waves E^e_ω and E^o_ω interact and generate a soliton in the wave $E^e_{2\omega}$ which, due to its finite lifetime, decays into solitons in the wave E^e_ω and E^o_ω.

In order to provide a theoretical confirmation of the experimental results, numerical simulation of eq. 1.10, with $\delta_1 = -\delta_2$ and $\delta_3 = 0$, in the $x-z$ plane corresponding to the initial data at $z = 0$ ($A_1(x,0) \neq 0$, $A_2(x,0) \neq 0$, $A_3(x,0) = 0$) are performed for three different input intensities (see fig. 2.10), corresponding to the three regimes previously identified. The numerical intensity level required to reach the linear ($I = 1MW/cm^2$), frequency conversion ($I = 0.1GW/cm^2$) and solitonic regime ($I = 2.5GW/cm^2$)

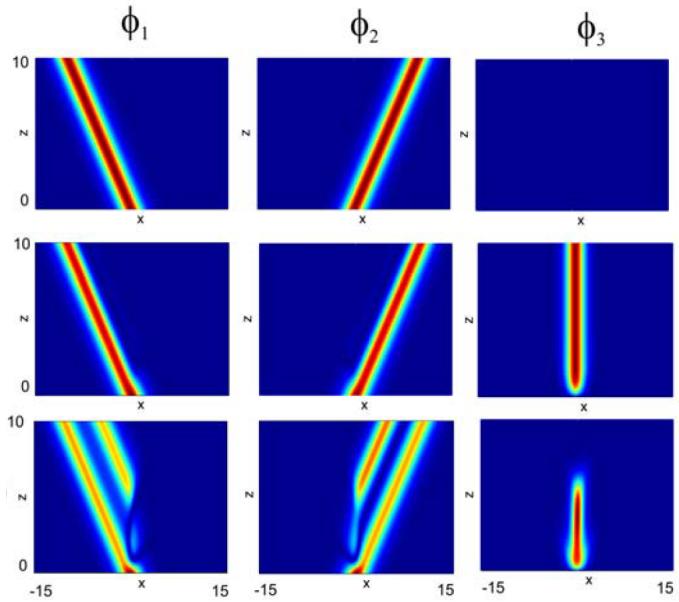

Figure 2.10: Numerical $x-z$ TWRI dynamics of waves at frequency ω_1, ω_2 and ω_3. (a) Linear, (b) frequency conversion, and (c) solitonic regime.

are quite different from the measured ones. This difference may be explained by different reasons: fluctuation of the laser pump, errors coming from energy meter, incertitude on the nonlinear coefficient value. Disregarding these minor discrepancies, the numerical simulation confirms the existence of the three different regimes namely linear (I=$1MW/cm^2$), frequency conversion (I=$0.1GW/cm^2$) and soliton (I=$2.5GW/cm^2$). In fig. 2.11 we compare the experimental beam profiles recorded at the output face of the KTP crystal with the calculated profiles solving eq. 1.10.

2.2.4 Conclusion

In conclusion, we have investigated the spatial dynamics of two beams at frequency ω, mixed to generate a field at the sum frequency 2ω. The numerical simulation well reproduces the experimental results. Depending on the input intensities, three different propagation regimes exist: linear, frequency conversion and solitonic regime. Our experimental results demonstrate the possibility of reaching soliton regimes in non-diffractive

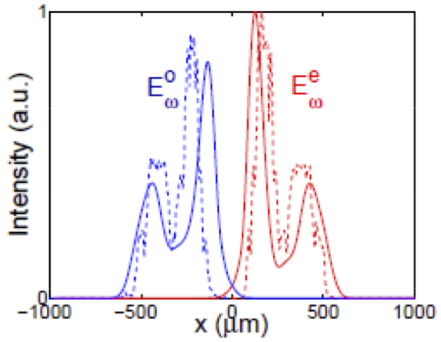

Figure 2.11: Experimental (dashed lines) and numerical (solid lines) spatial output profile at the exit face of the KTP crystal along x, intersection between the exit face of the crystal and the ordinary plane. E^e_ω (red lines) and E^o_ω (blue lines).

TWRI systems. We demonstrated that when the generated field at 2ω can sustain a TWRI soliton, which subsequently decays into fundamental solitons at ω. This is the first evidence of transition from a steady frequency wave generation to solitonic decay in nonlinear optics.

2.3 Simultons in SHG regime

2.3.1 Experimental setup

Fig. 2.12 shows the experimental setup used for the observation of simulton as a solution of the TWRI equation. The laser output pulse passes through a spatial diaphragm that adjust the beam diameter to 2.2 mm at FWHMI. The waves E^o_ω and E^e_ω are focused and spatially superimposed on the input face of the KTP crystal with a circular shape of 2.2 mm and 200 μm FWHMI respectively. An interferometric scheme, composed by a cube splitter and a series of three mirrors M2, M3, M4, is used for temporally superimpose the two beams. The half-wave plate and the quarter-wave plate, positioned on the arms of the interferometer, serve to adjust the intensity of the waves E^e_ω and E^o_ω, respectively. By orienting a second cube splitter, we adjust the incidence angle α. The wave vector of the input

waves are tilted at angles of θ_1=2.1deg and θ_1=-2.1deg with respect to the direction of perfect collinear phase matching for the extraordinary and the ordinary components, respectively. Inside the crystal these parameters correspond to a tilt between the input beams which is greater than the natural walk-off angle and it is introduced in the plane exhibiting the lowest critical phase matching. The sum-frequency direction lies in between the input directions ($\theta_3 \cong 0.4\,\mathrm{deg}$). By this way we fix the relation $V_1 < V_3 < V_2$ between the spatial velocities of the three waves. The rest of the setup is similar to that of fig. 2.3.

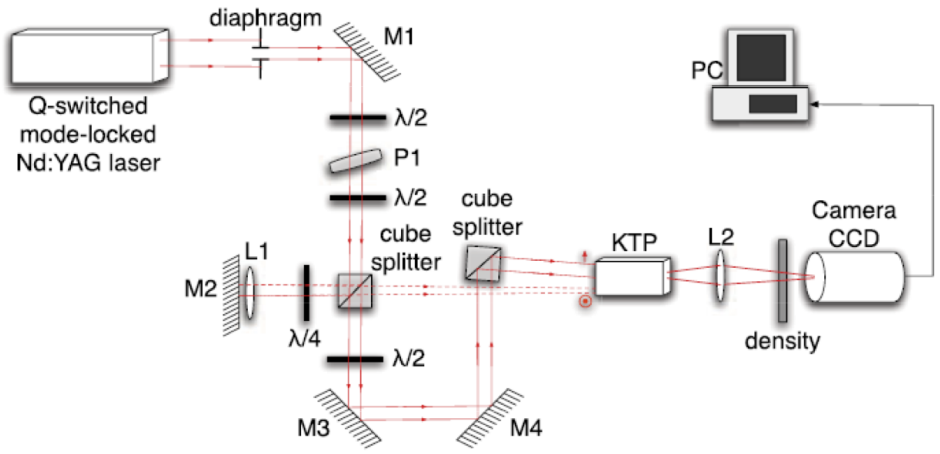

Figure 2.12: Experimental setup used for demonstrating the existence of simultons.

2.3.2 Experimental observation

Here, in tab. 2.2, we report the corresponding output intensities of the waves E^e_ω and E^o_ω, and the output intensities of the generated $E^e_{2\omega}$ wave. These values have been calculated from our measurements in energy and taking into account the laser pump parameters.

We realized several tests, keeping fixed the polarization state of each wave, the incidence angle and the phase matching conditions. Only the input intensity of fundamental waves has changed. We observe in tab. 2.2 that

test number	I^o_ω[MW/cm^2]	I^e_ω[MW/cm^2]	$I^e_{2\omega}$[MW/cm^2]
1	0.005	1.20	0
2	0.005	2.70	0.049
3	0.007	3.52	0.102
4	0.014	8.57	0.296
5	0.022	12.70	0.559
6	0.033	18.70	0.842
7	0.053	24.80	1.45
8	0.077	33.40	2.50
9	0.176	101.20	5.72

Table 2.2: Estimated intensities from measured energies of the input beams, A_1 and A_2 @1064 nm, and the third beam A_3 @532 nm.

the second harmonic component grows larger with the input intensities. Indeed, for low input intensities the waves E^e_ω and E^o_ω do not interact and no SH component is created (see fig. 2.13(a)). When increasing the input intensities, we observe in the spatial output profile that a dip appears on the E^o_ω component and correspondingly a SH beam appears with a polarization state along the extraordinary axis. The initial point of interaction between the beams E^e_ω and E^o_ω corresponds to the left part of the dip in the ordinary input component (red circle fig. 2.14(c)) . Whereas the final point of interaction is represented by the right part of the dip (black circle fig. 2.14(c)). Indeed in the x-y plane the wave E^e_ω propagates from left to right. When the input intensities are relatively high we observe in the dip of the wave E^o_ω the birth of an ordinary component at frequency ω. At the same time a deformation of the generated SH beam takes place. The spatial wave pattern of the wave $E^e_{2\omega}$ is gradually reshaped to a well defined horseshoe-like shape as the input intensities increase. For higher input intensities the formation of multiple horseshoes in the wave $E^e_{2\omega}$ is observed as shown in fig. 2.13(i). The same behaviour is found on the ordinary fundamental wave (see fig. 2.14(i)).

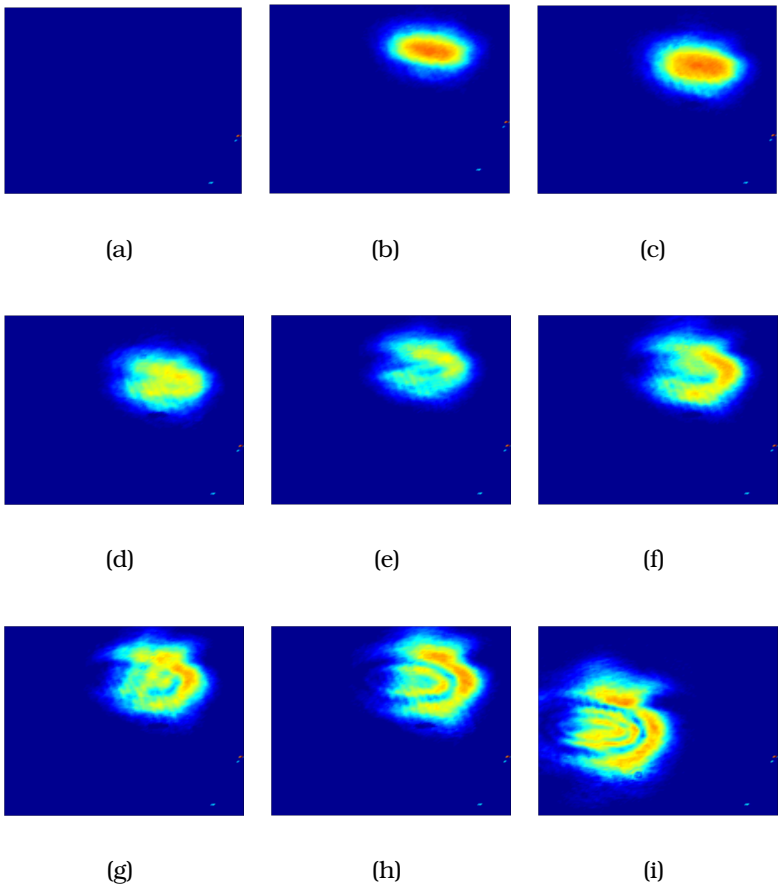

Figure 2.13: Evolution of the generated SH wave for different input intensities corresponding to the test (a) # 1, (b) # 2, (c) # 3, (d) # 4, (e) # 5, (f) # 6, (g) # 7, (h) # 8, (i) # 9..

2.3.3 Discussion

By the interpretation of the experimental results, we have identified for low input intensities ($I_\omega^o = 1.20MW/cm^2$ and $I_\omega^e = 0.005MW/cm^2$) a linear regime of propagation. Indeed, the recorded output spatial profiles show that the fundamental beams propagated without diffraction in the KTP crystal, following their own characteristic spatial directions. We do not observe nonlinear effects owing to the low values of input intensities.

When the input intensities are high enough to excite a weak non linear response of the KTP ($I_\omega^o = 2.7MW/cm^2$ and $I_\omega^e = 0.005MW/cm^2$), we observe the typical behavior of a noncollinear SHG: the input waves propagate with

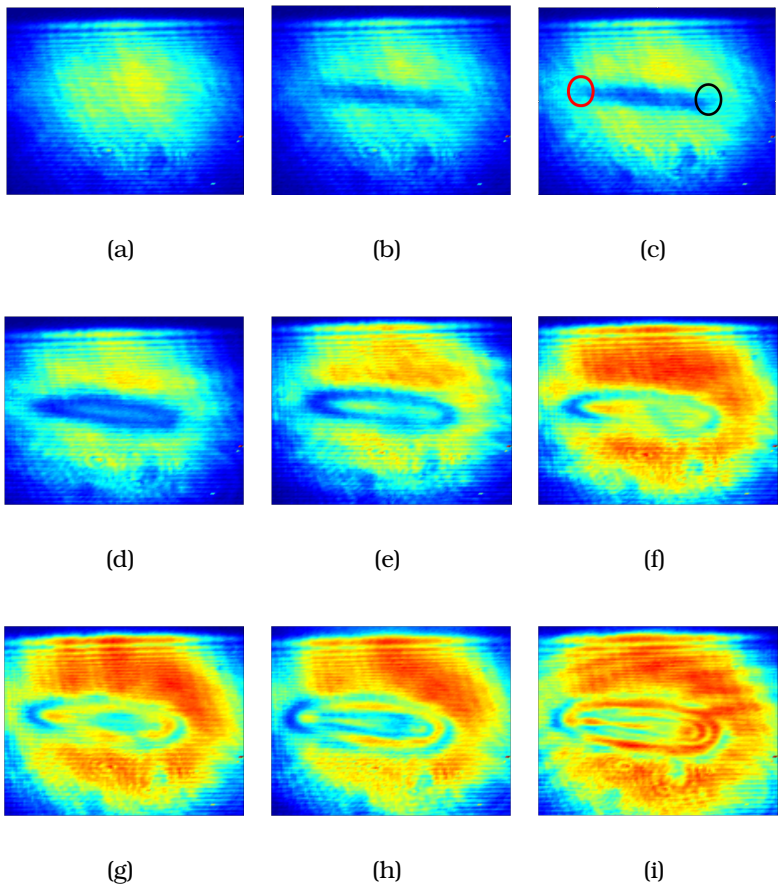

Figure 2.14: Evolution of ordinary FF wave for different input intensities corresponding to the test (a) # 1, (b) # 2, (c) # 3 (the red circle and the black one indicate the initial and the final point of interaction, respectively), (d) # 4, (e) # 5, (f) # 6, (g) # 7, (h) # 8, (i) # 9..

their own spatial velocity (V_1 and V_2 for the waves E^o_ω and E^e_ω respectively) and a SH beam is generated as long as the wave E^e_ω overtakes the wave E^o_ω. Indeed, the spatial width of the SH beam (fig. 2.13(c)) is directly dependent on the interaction length between the two fundamental waves.

For high input intensities ($I^o_\omega = 0.014 MW/cm^2$ and $I^e_\omega = 8.57 MW/cm^2$) instead, the interaction of the input beams leads to the generation of a narrow SH beam and to the formation of narrow dip in the wave E^o_ω observable at the output of the KTP crystal. Fig. 2.14(e) and fig. 2.13(e) reveal that the intensity, the width and the propagation direction of the E^e_ω wave are

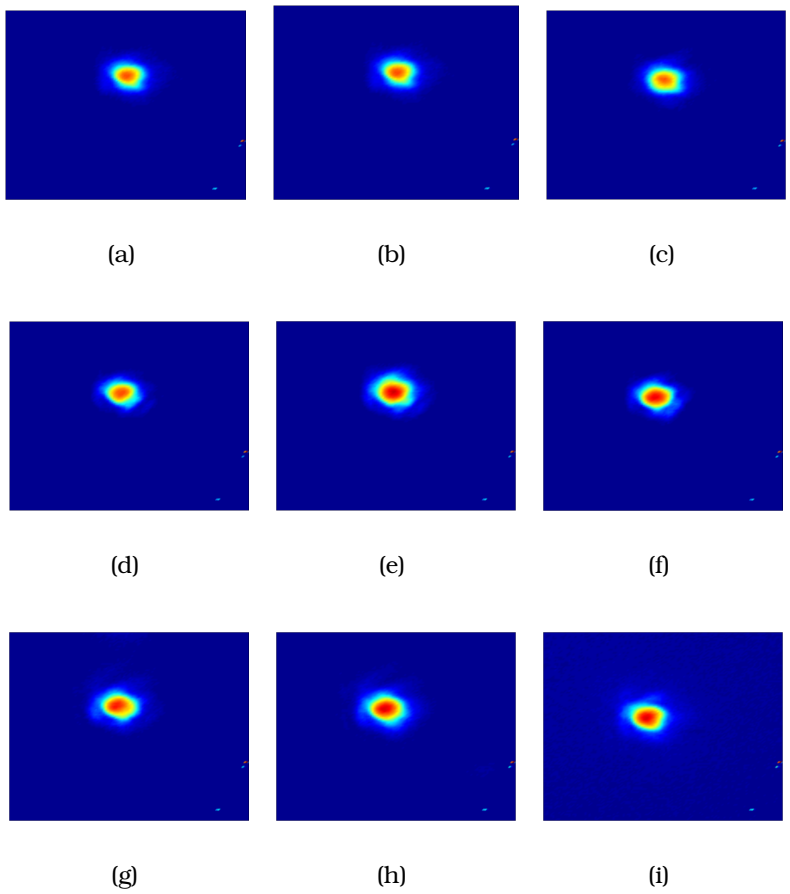

Figure 2.15: Evolution of extraordinary FF wave for different input intensities corresponding to the test (a) # 1, (b) # 2, (c) # 3, (d) # 4, (e) # 5, (f) # 6, (g) # 7, (h) # 8, (i) # 9..

modified. This is a clear evidence of a stable bright-dark-bright solitary triplet generation moving with a locked spatial nonlinear velocity (nonlinear walk-off angle) that lies between the input beams velocities [4]. This solitary wave, called simulton, results from the energy exchange between diffractionless waves of different spatial velocities. The horseshoe shape of the generated SH beam (fig. 2.13(e)) is another important consequence of simulton formation and propagation. The spatial modification of the propagation direction of the waves is also a clear signature of simulton generation. The left side of the horseshoe represents the place where the SH wave is generated with moderate intensity levels of the E_{ω}^{e} wave. This

SH part is moving under a velocity set by the linear response of the susceptibility . In contrast, the central part represents the wave $E^e_{2\omega}$ forming the solitary triplet. The simulton velocity, as described in Ref. [4] varies between the velocity V_2 and V_3 of the waves E^e_ω and $E^e_{2\omega}$, respectively. The nonlinear spatial walk-off which partially compensates the linear one increases when approaching the center of the beam.

At input intensities $I^o_\omega = 0.176 MW/cm^2$ and $I^e_\omega = 101.20 MW/cm^2$ the shape

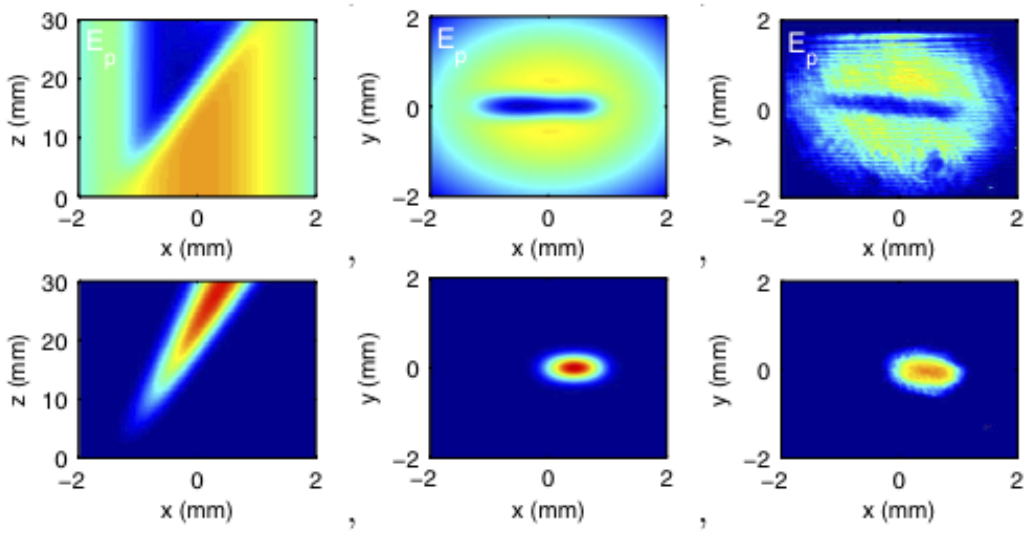

Figure 2.16: Numerical dynamics in the x-z plane (right) and x-y plane (center), compared to the experimental results (right) for the frequency conversion regime; the numerical results are obtained with $I^o_\omega = 0.03 MW/cm^2$ and $I^e_\omega = 10 MW/cm^2$.

of spatial pattern of the wave $E^e_{2\omega}$ (fig. 2.13(i)) reveals that two different simultons are generated: each horseshoe corresponds to a pairs of simultons. In the equation 1.10, it exists several couple of intensity and velocity permitting to obtain simulton propagation. Then by increasing the input energy, our spatial noncollinear scheme make possible propagations of independent simultons.

From a IST (Inverse Scattering Transform [1–3]) point of view, in the frequency conversion regime, the wave packet is composed only of radiations propagating independently with their own velocity. In the simulton regime

the wave packet is composed of both a radiation and a number N of discrete solutions (solitons). The number N of solitons depends on the input intensities: for $I_\omega^o = 0.022MW/cm^2$ and $I_\omega^e = 12.70MW/cm^2$, $N = 1$ instead for $I_\omega^o = 0.176MW/cm^2$ and $I_\omega^e = 101.20MW/cm^2$, $N = 2$.

In order to confirm the interpretation of the experimental results, we per-

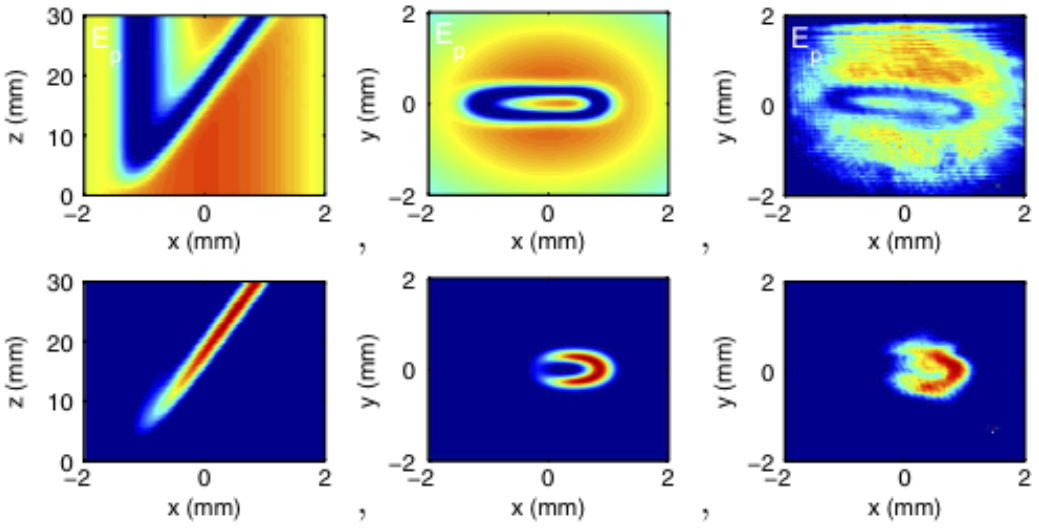

Figure 2.17: Numerical dynamics in the x-z plane (right) and x-y plane (center), compared to the experimental results (right) for the simulton regime with N=1; the numerical results are obtained with $I_\omega^o = 0.1MW/cm^2$ and $I_\omega^e = 50MW/cm^2$.

formed some numerical simulations of eq. 1.10 in the x-z and x-y plane. We show the results for the regime of frequency conversion (fig. 2.16) and simulton formation (for N=1 see fig. 2.17, for N=2 see fig. 2.18). Similarly to what happened for ZM-solitons, we observed even for this case a discrepancy between the experimentally measured beam intensities and the values obtained by numerical simulations. We believe that this fact is due to the incertitude in the real nonlinear response of the crystal, to the power jitter of the laser pump, as well as to the experimental errors in measurements. Nevertheless, the numerical results confirm the existence of the different regimes of propagation.

The displayed results of the figure 2.18 show experimental evidences of

velocity locked solitary triplets in a quadratic crystal, in the limit where diffraction is negligible.

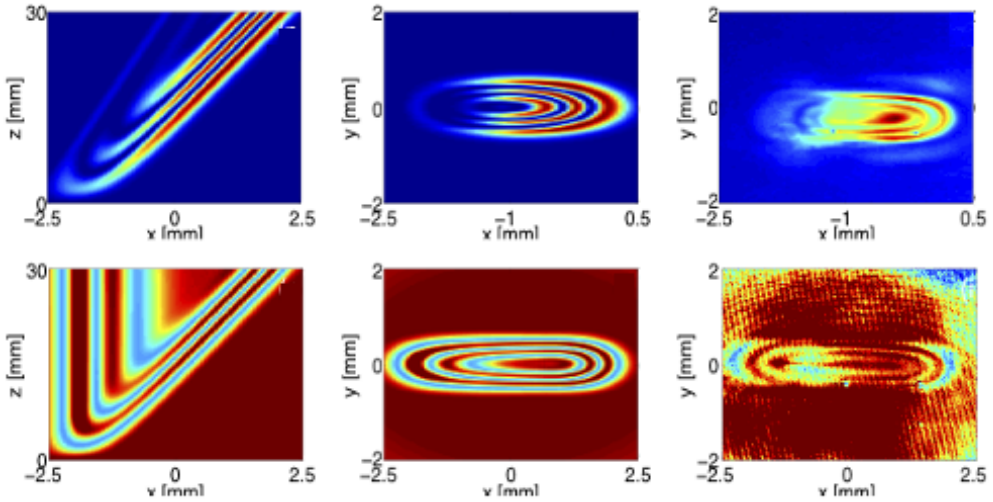

Figure 2.18: Numerical dynamics in the x-z plane (right) and x-y plane (center), compared to the experimental results (right) for the simulton regime with N=2; the numerical results are obtained with $I_\omega^o = 5MW/cm^2$ and $I_\omega^e = 500MW/cm^2$.

2.3.4 Conclusion

In conclusion, we have shown the existence of simulton solution in quadratic media. The theoretical description of that unusual type of propagation is obtained by resolving the coupled equations 1.10. These solitary waves, predicted in the 1970's [5], are stable velocity locked bright-bright-dark spatial triplets, obtained by the balance between the energy exchange rate and the velocity mismatch between the interacting waves. In particular three different regimes of propagation depending on the input intensities have been identified: linear regime, frequency conversion regime, simulton regime.

The concept of three-wave solitons may be useful to describe the interaction between either three beams in the spatial domain (diffractionless solitary waves) or three optical pulses in the time domain (dispersionless solitary waves).

To our knowledge this is the first experimental observation of efficient SF generation based on simultons.

Bibliography

[1] M. Ablowitz and H. Segur, *Solitons and the inverse scattering transform*. Philadelphia, Pa.: Society for Industrial and Applied Mathematics (SIAM, 3600 Market Street, Floor 6, Philadelphia, PA 19104)„ 1981.

[2] V. Zakharov, "What is Integrability? berlin etc., Springer-Verlag," *ZAMM - Journal of Applied Mathematics and Mechanics / Zeitschrift fÃijr Angewandte Mathematik und Mechanik*, vol. 73, no. 2, pp. 76–76, 1991.

[3] A. Mikhailov, ed., *Integrability*, vol. 767. Berlin, Heidelberg: Springer Berlin Heidelberg, 2009.

[4] A. Degasperis, M. Conforti, F. Baronio, and S. Wabnitz, "Stable control of pulse speed in parametric Three-Wave solitons," *Physical Review Letters*, vol. 97, Aug. 2006.

[5] K. Nozaki and T. Taniuti, "Propagation of solitary pulses in interactions of plasma waves," *Journal of the Physical Society of Japan*, vol. 34, pp. 796–800, Mar. 1973.

CHAPTER 3

Application of Zakharov Manakov solitons in mode-locked laser

Contents

Here we present a direct application of the soliton concept expressed in chapter 2. We show results on mode-locking operation of a flash-lamp pumped Nd:YAG laser using soliton decay in KTP crystal. In this chapter we first briefly introduce some basic concepts on solid-state laser, then we illustrate experimental results obtained with a particular resonator configuration. The last sections are dedicated to elucidate the operating principle of our mode-locked laser.

3.1 Solid-state lasers

At the present time solid-state lasers are the most versatile lasers, widely used in many applications as nonlinear spectroscopy, nano-periodic structuring, micromachining or nonlinear conversion etc. Indeed the size and shape of the active material can be chosen to achieve particular gain, pulse duration, wavelength, repetition rate, peak power.

In analogy to the maser, the name "laser" was coined by its inventor, T. Maiman, in 1960, as an abbreviation of light amplification by stimulated emission of radiation. The first solid-state laser was build-up with a ruby crystal, optically pumped by a helical flash-lamp that surrounded the cylindrical laser crystal. The parallel ends of the ruby crystal were silvered, with a small hole at one end for observing the radiation. The laser emission was in the visible domain near 694 nm.

The output of the first ruby laser systems consisted of a series of irregular spikes, extending over the duration of the pump pulse. In 1961 R.W. Hellwarth discovered a method called Q-switching for concentrating the output energy from the ruby laser into a single pulse. The Q-switching is an optical shutter which prevents laser action during the flash-lamp pulse, and therefore the population inversion can reach large values. If the shutter is opened, stored energy will be released in a time characterized by a few round-trips between the resonator mirrors [1].

Later, the ruby crystal was replaced by a more efficient neodymium doped glass (Nd:glass). The best choice of a host for neodymium ions is yttrium aluminium garnet (Nd:YAG) with a main output emission close to 1064 nm. Nd:YAG crystal has several advantages as: large fluorescence duration, good thermal conductivity, laser efficiency and can be grown with relative facility [2].

In 1965, a technique called "mode-locking" was invented. It permits to transform the random phase fluctuations of the longitudinal modes of a given resonator into a uniform and unique phase value leading to short pulses with a duration inversely proportional to the laser emission bandwidth.

3.1.1 Q-switching

A mode of laser operation commonly employed for the generation of high pulse power is known as Q-switching. It has been so called because the

optical quality factor Q of the resonator cavity is altered when this technique is used. Indeed resonators are characterized by the quality factor Q, which is defined as 2π times the ratio between the stored energy E_{st} and the dissipated energy E_d per period T_0 (where $E_d = E_{st}(1 - exp(-\frac{T_0}{\tau_c}))$ and τ_c represents the average lifetime of the photons in the resonator):

$$Q = 2\pi \frac{E_{st}}{E_d} = 2\pi \left[1 - exp\left(-\frac{T_0}{\tau_c}\right)\right]^{-1} \approx \frac{2\pi\tau_c}{T_0} = 2\pi\nu_0\tau_c. \tag{3.1}$$

Assuming that the finite lifetime of the photons determine the minimum bandwidth of the passive resonator according to the Fourier transform $\Delta\omega = \frac{1}{\tau_c}$, the Q factor can be defined as [3]:

$$Q = \frac{\nu_0}{\Delta\omega}. \tag{3.2}$$

In the technique of Q-switching, the energy is stored in the amplifying medium by optical pumping while the cavity Q factor is lowered to prevent the onset of laser emission. Although the energy stored and the gain in the active medium are high,the cavity losses are also high. Consequently the lasing action is blocked and the population inversion may reach levels far above the threshold of a normal lasing action. When a high cavity Q is restored, the stored energy is suddenly released in the form of very short pulse of light, in a extremely short time. This is the reason why with the Q-switching method, one can obtain high peak power.

Figure 3.1 shows a typical time sequence of the generation of a Q-switched pulse. The typical pulse duration obtained with such kind of method is mainly driven by the cavity length and is between 100 ps and several hundreds of nanoseconds. It is also well known that gain switching in a passive optical resonator acts as Q-switching effect leading also to short pulse generation [4].

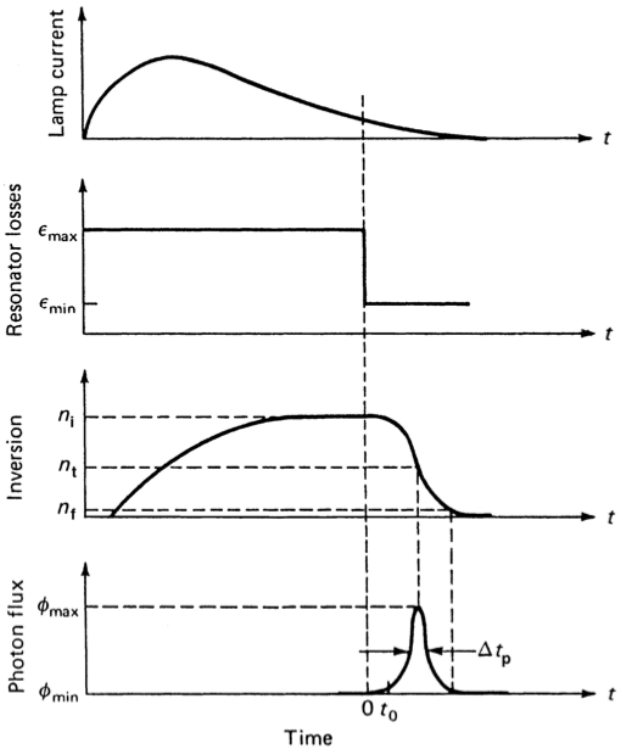

Figure 3.1: Development of a Q-switching laser pulse. Shown the flash-lamp output, resonator loss, population inversion, and photon flux as a function of time [3].

3.1.2 Mode-locking

The instantaneous output peak power emitted from laser oscillators is subjected to strong fluctuations which originate from the interference of longitudinal resonator modes exhibiting random phase relations. By establishing a fixed phase relationship among the longitudinal modes a powerful well-defined single pulse circulating in the resonator can be generated. Mode-locking requires a mechanism able to produce ultrafast modulation loss in the resonator to favour intense radiations compared to the average intensity. The speed of this modulator has to be shorter than the time round-trip of the light contained in the resonator.

The process of pulse formation starts from amplification of noise coming from laser radiation. The fluctuations experience a strong absorption and are gradually suppressed: then the strongest peak power reach the inten-

sity level for which the mode-locking mechanism lower the cavity losses (see fig. 3.2). This result in a phase-locking between all the longitudinal modes and in narrowing of the existing pulse. The shortest pulse duration is inversely proportional to the gain bandwidth of the laser $\Delta\nu_L$ (eq. 3.3): indeed it is said to be transform limited.

$$t_p \approx \frac{1}{\Delta\nu_L} \approx \frac{t_r}{N}, \tag{3.3}$$

where $N = \Delta\nu_L t_r$ is the number of axial mode that are contained within the oscillating bandwidth, $t_r = \frac{2L}{c}$ is the round-trip time in the optical resonator, L is the cavity length and c is the speed of light.

This mode-locking mechanism can be achieved by an externally driven optical resonator (active mode-locking) or by an ultrafast saturable absorber (passive mode-locking). In pulsed solid-state lasers, the presence of a saturable absorber results not only in mode-locked, but also in Q-switched operation. Indeed for each flash-lamp pulse, a short packed of mode-locked pulses is generated, for this reason the laser source is called Q-switched mode-locked laser.

Only few mode-locking techniques, among all existing ones, are used in flash-lamp pumped lasers. Indeed, high laser gain requires the use of fast saturable absorbers exhibiting a large evolution of their absorption. The oldest mode-locking method used in flash-lamp pumped laser is based on saturable absorption obtained by means of an optical cell with a dye solution [5, 6]. Unfortunately this method give rise to large instabilities in time because of the fast deterioration of the saturable element. Another possibility to reach mode-locking regime is to use solid-state nonlinear elements like nonlinear semiconductor Fabry-Perot saturable absorber (SESAM) [7, 8] or frequency-doubling crystal combined with a dichroic mirror [9, 10] or a polarizer to mimic the effect of an intensity dependent mirror [11, 12]. If SESAM's are particularly well adapted to diode pumped systems, their use in flash-lamp pumped lasers are more prob-

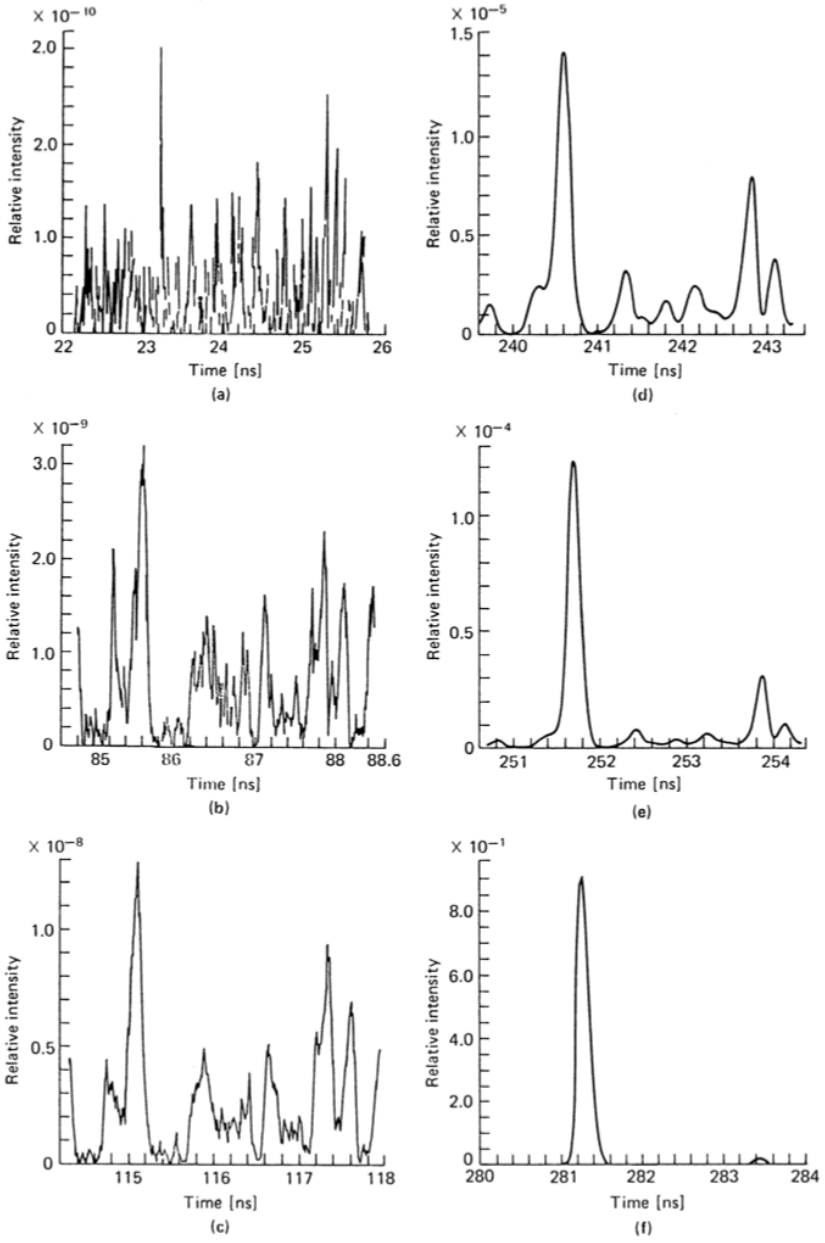

Figure 3.2: Numerical simulation of the process of mode-locked pulse formation from noise using nonlinear absorber: (a-c) linear amplification, (d-e) nonlinear absorption, (f) nonlinear amplification, saturation of the nonlinear absorber [3].

lematic because of large pumping fluctuation leading to the appearance of extreme pulses able to damage the nonlinear component. Nonlinear crystal cut for second harmonic generation offers an interesting alternative to reach mode-locking regime in laser exhibiting large gain with strong intensity [9–11].

3.2 Mode-locking operation with Zakharov-Manakov solitons

Here, we present a new mode-locking method based on TWRI obtained in a type II KTP crystal cut for second harmonic generation. Indeed, we exploit the decay process of Zakharov-Manakov solitons presented in chapter 2.

3.2.1 Experimental setup and results

The resonator configuration used to obtain the mode-locked regime is presented in fig. 3.3.

The laser consists of two flat mirrors M1 and M2, having respectively

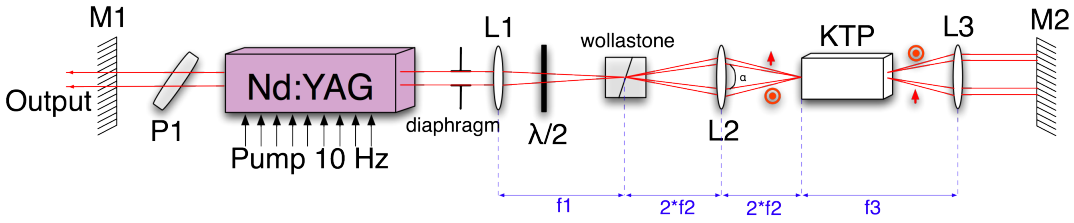

Figure 3.3: Schematic setup of the flash-lamp-pumped Nd:YAG laser operating in the mode-locked regime by means of TWRI solitonic decay. L1,L2,L3 lenses; P1 polarizer; M1, M2 mirrors.

80% and 90% reflectivity at 1064 nm and 6% for the second harmonic. The active medium is a 1.1% atomic doped Nd:YAG rod of 100 mm length, transversely pumped by two flash lamps with a typical energy of 25 J. The repetition rate is 10 Hz. Single-transverse-mode operation is ensured by a diaphragm of 1 mm in diameter. The laser output is delivered through mirror M1. A Brewster polarizer is used to ensure the linear polarization

of the beam. We used a Wollaston cube polarizer and a half-wave plate to obtain, after passage of the light through L1, two separated beams with perpendicular linear polarization states. A lens L2 is used to focus and spatially superimpose the two beams on the input face of the 3 cm long type II KTP crystal cut and oriented for exact phase matching and for SHG in a non-collinear geometry.

In this configuration, the two beam waists are spatially located at the input face with a circular shape of 120 μm (FWHMI). The directions of the linear polarization state of the two beams are adjusted so to coincide with the ordinary and the extraordinary axes of the KTP crystal. The wave vectors of the input fields were tilted at angles of θ_1 =0.7° and θ_2 =-0.7° (in the crystal) with respect to the direction of perfect collinear phase matching for the extraordinary and the ordinary components, respectively. Lens L3 ensures the initial beam re-composition after reflection on the end cavity mirror M2.

The mechanism of TWRI solitonic decay illustrated in chapter 1 is here used to obtain an intensity-dependent transmission after the beam round-trip through the diaphragm, the Wollaston cube, the KTP crystal and the two lenses. For low pump energies a stable intra-cavity beam is generated. After its division in two components inside the Wollaston cube and their superimposition at the input face of the crystal, a third beam at SH is generated in the median direction between the two fundamental waves. In this condition no solitonic propagation is obtained and no nonlinear transmission behaviour is observed. Then a slight misalignment of the cavity by means of the L3 lens shift is realized to increase the resonator losses.

By increasing the pump energy above a threshold level, we observe at the laser output a train of energetic pulses, with an envelope duration of 180 ns (see fig. 3.4(a)). This is a clear signature that the mode-locked regime is reached. Indeed, the shortest pulse observed, in the central part of the pulse train, exhibits duration of 100 ps FWHMI (see fig. 3.4(b)), which is typical of a mode-locked regime. In this case the mode-locked regime is si-

multaneously accompanied by a repetitive 10 Hz Q-switching like regime, due to the flash pumping repetition rate (in fact the envelope duration of fig. 3.4(a) is typical of a Q-switching regime). The stability of peak power from shot to shot is close to 80 %. All experimental results were measured with a fast oscilloscope and a photodiode with minimum bandwidth of 12 GHz.

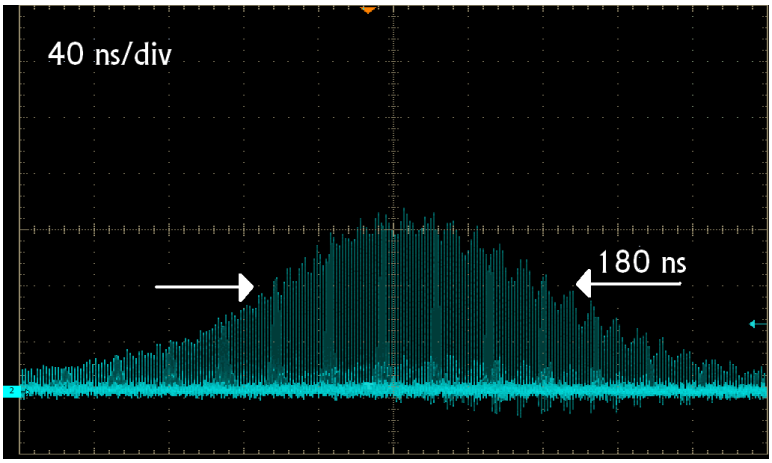

(a)

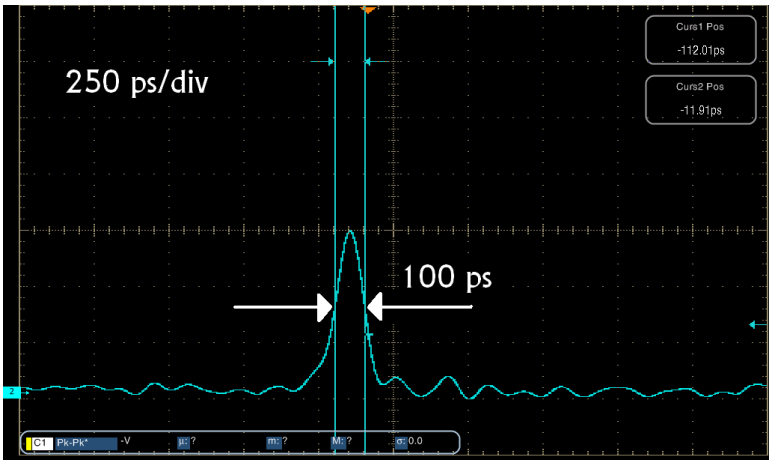

(b)

Figure 3.4: Experimental results obtained with the setup of fig. 3.3: (a) characterization of the pulse train delivered by the mode-locked flash-lamp-pumped Nd:YAG laser; (b) characterization of the profile and duration of a pulse selected in the central part of the delivered pulse train.

3.2.2 Discussion

The reached Q-switched mode-locked regime is clearly due to the intensity-dependent transmission created by the solitonic decay. Indeed, the soliton threshold is reached leading to spatial reorientation of the two beams inside the cavity. In this case the misalignment induced by lens L3, is compensated by solitonic dynamics and in a way similar to what is commonly observed with a saturable absorber. The mode-locking regime is reached by increasing the pump level above an intensity threshold. The threshold intensity for mode-locked operation is estimated to be about $800MW/cm^2$. As a proof, the repetition rate of the mode-locked pulse (measured to 136 MHz), matches with the cavity round-trip time.

Numerical simulation were performed to characterized the solitonic dynamics, inside the laser resonator. In fig. 3.5 we show the calculated intensity-dependent transmission curve induced by soliton propagation. This results are obtained considering the effect induced by the combination of KTP crystal and lens $L3$ represented by a numerical filter which provide 100 % transmission of the soliton components and 15 % transmission of the linear components (spatial filtering). This data corresponds to a single-pass transmission through the setup. The intracavity soliton dynamics shown in section 2.2 is shown in fig. 3.5. For a linear regime of propagation (a of fig. 3.5) the low transmission is due to the strong losses imposed by the cavity. When increasing the pump intensity, a part of the fundamental beams is converted into SH (frequency conversion regime), which is partially transmitted by the mirror M2. This corresponds to increase the loss of the resonator (b of fig. 3.5). For higher intensity, the soliton threshold formation is reached (solitonic regime, c) and d) of fig. 3.5), so all the energy is enclosed in the soliton components, which are totally reflected. Additionally, the weak initial misalignment of the resonator is compensated by the solitonic propagation which decreases instantaneously the resonator losses and gives rise to picosecond pulses.

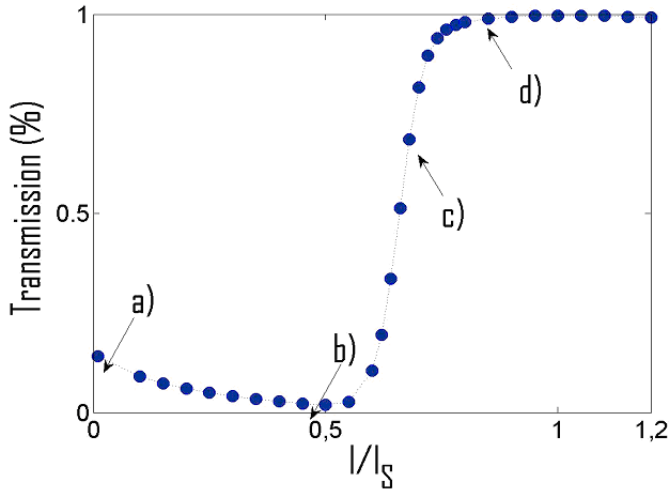

Figure 3.5: Numerical data representing the intensity-dependent transmission of the setup of fig. 3.3. I is the intensity of the input beams, I_s define the ZM soliton threshold.

3.3 Conclusion

In conclusion we have demonstrated, for the first time, the passive Q-switched mode-locked operation of a flash-lamp pumped Nd:YAG laser thanks to TWRI solitonic dynamic in a type II phase-matched KTP crystal. The mode-locked regime produced pulse train with duration close to 100 ps, repetition rate of 136 MHz and modulation depth almost 100 %. The mode-locked pulses are modulated with a longer 180 ns pulse envelope with repetition rate of 10 Hz. The intensity threshold for mode-locking is imposed by solitonic threshold formation which depends on the input condition of waves travelling through the nonlinear crystal.

Bibliography

[1] F. McClung and R. Hellwarth, "Giant optical pulsations from ruby," *Journal of Applied Physics*, vol. 33, p. 828, 1962.

[2] J. Geusic, H. Marcos, and L. Van Uitert, "Laser oscillations in Nd-doped Yttrium Aluminum, Yttrium Gallium and Gadolinium Garnets," *Applied Physics Letters*, vol. 4, p. 182, 1964.

[3] W. Koechner and M. Bass, *Solid-state lasers : a graduate text*. New York: Springer, 2003.

[4] B. Garside, "Laser mode locking using saturable absorbers," *Journal of Applied Physics*, vol. 44, p. 2335, 1973.

[5] S. Oda, Y. Segawa, N. Kodama, P. Kim, and S. Namba, "Passive Mode Locking of a Flashlamp-Pumped Ti:Sapphire Laser," *Japanese Journal of Applied Physics*, vol. 28, pp. L1977–L1978, Nov. 1989.

[6] M. Demchuk, A. Demidovich, N. Zhavoronkov, V. Mikhailov, A. Shkadarevich, A. Ishchenko, and A. Sopin, "Passive mode locking in a flashlamp-pumped $Al_3O_2 : Ti^{3+}$ laser," *Soviet Journal of Quantum Electronics*, vol. 20, pp. 93–94, Feb. 1990.

[7] B. Bouma, A. Gouveia-Neto, J. Izatt, J. Russell, R. Sierra, U. Keller, and J. Fujimoto, "Hybrid mode locking of a flash-lamp-pumped $Ti : Al_2O_3$ laser," *Optics Letters*, vol. 19, p. 1858, Nov. 1994.

[8] U. Keller, D. Miller, G. Boyd, T. Chiu, J. Ferguson, and M. Asom, "Solid-state low-loss intracavity saturable absorber for Nd:YLF lasers: an antiresonant semiconductor FabryâĂŞPerot saturable absorber," *Optics Letters*, vol. 17, p. 505, Apr. 1992.

[9] K. Stankov, "A mirror with an intensity-dependent reflection coefficient," *Applied Physics B Photophysics and Laser Chemistry*, vol. 45, pp. 191–195, Mar. 1988.

[10] K. Stankov, "Mode locking by a frequency-doubling crystal: generation of transform-limited ultrashort light pulses," *Optics Letters*, vol. 14, p. 359, Apr. 1989.

[11] V. Kubeček, V. Couderc, B. Bourliaguet, F. Louradour, and A. Barthélémy, "4-W and 23-ps pulses from a lamp-pumped Nd:YAG laser passively mode-locked by polarization switching in a KTP crystal," *Applied Physics B: Lasers and Optics*, vol. 69, pp. 99–102, Aug. 1999.

[12] V. Couderc, F. Louradour, and A. Barthélémy, "2.8 ps pulses from a mode-locked diode pumped Nd:YVO4 laser using quadratic polarization switching," *Optics Communications*, vol. 166, pp. 103–111, Aug. 1999.

CHAPTER 4

Supercontinuum generation in photonic crystal fibre

Contents

In this chapter we present the main characteristics of a particular phenomenon that leads to the extreme spectral broadening of an optical pulse, named supercontinuum (SC) generation. In particular we are interested in describing the nonlinear effects that are responsible for SC generation in an optical fibre. At the end of this chapter a brief historical overview of SC generation is introduced, a particular attention is given to the excitation regime.

4.1 Photonic crystal fibre

A major discovery for modern telecommunications is the optical fibre: a long filament of glass (or in some cases plastic) that guides light, usu-

ally over a long distance. Optical fibres are also used in other domains, ranging from medicine to astrophysics. Most of the optical fibres are composed by a central core that is surrounded by a cladding with low dielectric constant, which confines the light by total internal reflection (fig. 4.1(a)). Since 1980s, the interest of many researchers has been attracted by the ability to structure materials at the scale of the optical wavelength itself in order to develop new optical media, known as photonic crystals. Photonic crystals fibres (PCFs) rely on a regular microstructure, which alters its optical properties [1]. In such a fibre, the cladding is composed by a periodic structure of air holes that surround the silica core [2, 3] as shown in fig. 4.1(b). These air holes reduce the average index of refraction of the cladding thus allowing to guide the light inside the core.

In the next subsections, we will show how PCF geometry can modify the chromatic dispersion and nonlinear response.

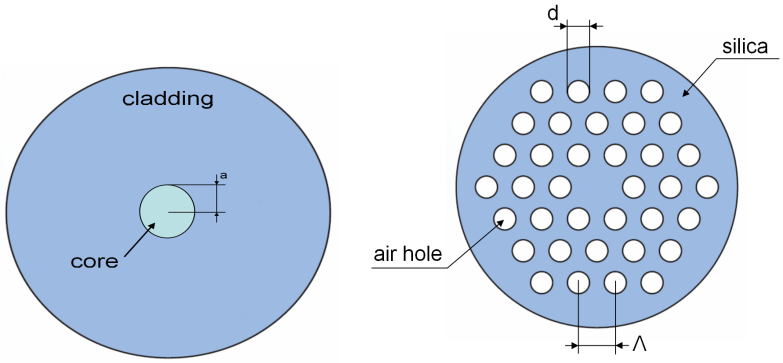

Figure 4.1: (a) Step index fiber with core radius a. (b) PCF with lattice period Λ and air-hole diameter d.

4.1.1 Dispersion

As I have presented in the first part of my thesis, the concept of group velocity plays an important role in nonlinear optics.

A pulse propagating inside a PCF undergoes a chromatic dispersion (dis-

persion due to the dependence of the refractive index versus the wavelength). This chromatic dispersion is mainly due to two contributions: the material dispersion D_m and the waveguide dispersion D_w. The total chromatic dispersion is:

$$D = -\frac{2\pi c}{\lambda^2}\beta_2 = D_m + D_g, \tag{4.1}$$

where

$$\begin{aligned} D_m &= -\frac{\lambda}{c}\frac{\partial^2}{\partial\lambda^2}(n_{silica}), \\ D_w &= -\frac{\lambda}{c}\frac{\partial^2}{\partial\lambda^2}(n_{eff}), \end{aligned} \tag{4.2}$$

with c the speed of light, n_{silica} the refraction index of the silica glass as a function of wavelength (normally calculated from the Sellmeier equation), n_{eff} the effective refraction index of the fundamental mode, β_2 the group velocity dispersion (evolution of group velocity as a function of wavelength) and it is calculated from the second order derivative of $\beta(\omega)$ upon angular frequency. More generally, far from resonances, we can approximate the dependency of wavenumber with angular frequency by a polynome:

$$\beta(\omega) = n_{eff}(\omega)\frac{\omega}{c} = \beta_0 + \beta_1(\omega-\omega_0) + \frac{1}{2}\beta_2(\omega-\omega_0)^2 + \frac{1}{6}\beta_3(\omega-\omega_0)^3 + ... \tag{4.3}$$

By properly changing the geometrical characteristics of the air holes in the PCF cross-section [4], the dispersion parameter can be significantly changed, thus obtaining wide tunability of the zero-dispersion wavelength (ZDW), as well as particular values of the dispersion curve slope [5]. The fibre can be tailored in relation to the laser source used: it is then possible to pump the fibre in the near infrared domain (800 nm-2 μm) in an anomalous dispersion regime. Most of PCF available at present days are extremely lossy with respect to standard fibres. Their applications are then limited to short segments. In fig. 4.2 we show a typical example where the dispersion curves of a conventional fibre is compared with the PCF ones. We call normal dispersion if $D < 0$ ($\beta_2 > 0$) or anomalous dispersion if

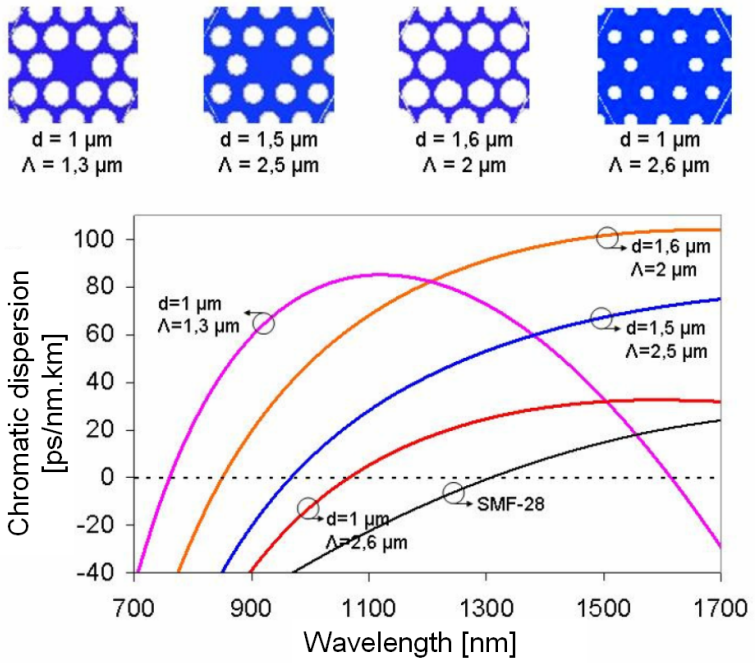

Figure 4.2: Chromatic dispersion curves of the fundamental mode for different PCFs and for a standard single mode fibre SMF-28 [6].

$D > 0$ ($\beta_2 < 0$). The case when $D = 0$ ($\beta_2 = 0$) corresponds to the ZDW. When a pulse propagates in the anomalous dispersion regime, the short wavelength tail of its spectrum travel faster than the long wavelength tail.

4.1.2 Non-linearity

One of the primary applications of PCFs has been to enhance the nonlinear optical effects. Nonlinear phenomena in fibres are typically due to the Kerr effect, in which the refractive index varies in proportion to the intensity of the light. Differently from what observed in chapter 2 for crystals, here the lowest order nonlinear contribution to the polarization vector comes from the third-order susceptibility $\chi^{(3)}$ which takes into account the nonlinear refractive index n_2 and the two-photon absorption coefficient α_2:

$$n_2 = \frac{3}{8n_0} Re\left(\chi^{(3)}_{xxxx}\right) \quad and \quad \alpha_2 = \frac{3\omega_0}{4n_0 c} Im\left(\chi^{(3)}_{xxxx}\right). \tag{4.4}$$

The coefficient α_2 is small for silica fibre and is usually neglected. The commonly used value for n_2 is $3.2 \times 10^{-20} m^2/W$ [7]. Silica based materials have rather weak non-linearities, and it is necessary to use very high intensity or to propagate over a very long distance before the effects of $n_2 I$ become significant. Large index contrast may then reduce the mode field diameter and then enhance the nonlinear effect: this is one of the interests for PCF.

Generally, the strength of the nonlinear effects for a given waveguide mode can be characterized by a single parameter γ, called nonlinear coefficient [7]:

$$\gamma = \frac{n_2 \omega_0}{c A_{eff}}. \tag{4.5}$$

where A_{eff} is the effective area of the propagation mode in the core which depends on fibre parameters such as the core radius and the core-cladding index difference but also varies with respect to the wavelength. So, for wavelengths much smaller than the core diameter, the propagation mode is mainly confined into the core. For wavelengths of the same order of the core diameter, the propagation mode tends to widen thus increasing the effective area [8]. Finally as the effective area is a function of wavelengths also the nonlinear coefficient turns to be wavelengths dependent.

A direct consequence of the intensity dependence of the refractive index is the nonlinear phase shift:

$$\phi_{NL}(\omega, t) = \frac{2\pi}{\lambda} n_2 I(t) L. \tag{4.6}$$

This nonlinear phase shift is self-induced by the propagation of an optical beam over a fibre distance L and modifies the cumulated phase as follows:

$$\begin{aligned} \phi(\omega, t) = n(\omega, t)\frac{\omega}{c}L = [n_0(\omega) + n_2 I(t)]\,\frac{2\pi}{\lambda}L = \\ = \underbrace{\frac{2\pi}{\lambda} n_0(\omega) L}_{\phi_L(\omega)} + \underbrace{\frac{2\pi}{\lambda} n_2 I(t) L}_{\phi_{NL}(\omega)}. \end{aligned} \tag{4.7}$$

4.2 Nonlinear Schrödinger equation

The propagation of electromagnetic field in a dieletric medium along the coordinate z is described by an extended version of the nonlinear Schrödinger equation (NLSE) [7] assuming a slowly varying envelope. By considering a moving frame centered on the pulse and moving at the speed $v_g = \frac{1}{\beta_1}$, the NLSE reads as:

$$\begin{aligned} \frac{\partial A(z,t)}{\partial z} - \sum_{n\geq 2} \beta_n \frac{i^{n+1}}{n!} \frac{\partial^n A(z,t)}{\partial t^n} + \frac{\alpha}{2} A(z,t) = \\ = \imath\gamma \left(1 + \frac{\imath}{\omega_0}\frac{\partial}{\partial t}\right) \left(A(z,t) \int_0^{+\infty} R(\tau)|A(z,t-\tau)|^2 \partial\tau\right), \end{aligned} \tag{4.8}$$

where α represents the loss inside the fibre, β_n are the Taylor expansion coefficients of the propagation constant β, γ is the nonlinear coefficient as expressed in eq. 4.5. In the eq. 4.8 it is included also the nonlinear response of the medium $R(t)$, defined as:

$$R(t) = (1 - f_R)\delta(t) + f_R h_R(t). \tag{4.9}$$

where $\delta(t)$ is the Dirac function and $h_R(t)$ is the Raman response function. The function $R(t)$ therefore includes the delayed vibrational contribution of the Raman response through the coefficient $f_R = 0.18$ and the instantaneous electronic contribution through the term $(1 - f_R)$.

In the next section, will be presented some nonlinear effects involved in the propagation of an optical pulse in a fibre. These examples will be useful to understand the experimental and theoretical work presented in the next chapter. It is proven useful to introduce two length scales, known as the dispersion length L_D and the nonlinear length L_{NL} [7].

$$L_D = \frac{T_0^2}{|\beta_2|}, \quad L_{NL} = \frac{1}{\gamma P_0}, \tag{4.10}$$

where T_0 and P_0 are the input pulse width and the peak power of the incident pulse, respectively. These two lengths, L_D and L_{NL}, provide the distance over which dispersive or nonlinear effects become important for a pulse evolution. Similary to what I did in the first part of my thesis in nonlinear crystals, it is necessary to compare these lengths. Here we identify four different regimes:

- if $L \ll L_{NL}$ and $L \ll L_D$ the nonlinear and dispersive effects do not play a significant role during pulse propagation;
- if $L \gg L_{NL}$ and $L \gg L_D$ dispersion and non-linearity act together as the pulse propagates along the fiber;
- if $L \ll L_{NL}$ and $L \sim L_D$ the pulse evolution is governed by GVD;
- if $L \sim L_{NL}$ and $L \ll L_D$ the pulse evolution is governed by nonlinear effects.

4.3 Nonlinear effects in optical fibre

This section presents some of the nonlinear effects involved during pulse propagation inside the fibre. These effects can be organized in two categories:

- elastic phenomena (self-phase modulation, cross-phase modulation, four wave mixing, modulation instability);
- inelastic phenomena (Raman effect).

We will also talk about solitonic effects in optical fibre, which is due to a combination of the effects mentioned in the above categories.

4.3.1 Self phase modulation

One of the first expression of the optical Kerr effect is the self-phase modulation (SPM): that is the instantaneous dependence of the refractive index

upon the intensity associated to the electric field. Taking into consideration only the instantaneous electronic contribution and neglecting the Raman term, the NLSE takes the form:

$$\frac{\partial A(z,t)}{\partial z} - \sum_{n\geq 2} \beta_n \frac{i^{n+1}}{n!} \frac{\partial^n A(z,t)}{\partial t^n} + \frac{\alpha}{2} A(z,t) = \imath\gamma \underbrace{A(z,t)|A(z,t)|^2}_{\textbf{SPM}}, \tag{4.11}$$

As expressed in eq. 4.6, the nonlinear phase shift is proportional to the pulse intensity. This phenomena leads to a modification of instantaneous frequency:

$$\omega(t) = -\frac{\partial \phi}{\partial t} = \omega_0 + \delta\omega(t) \propto \omega_0 - n_2 \frac{\partial |A(z,t)|^2}{\partial t} = \omega_0 - n_2 \frac{\partial I(t)}{\partial t}. \tag{4.12}$$

thereby, all frequencies lower than the central frequency of the pulse are generated on the leading edge of the pulse (Stokes side) instead all frequencies greater than the central frequency of the pulse are generated on the trailing edge (anti-Stokes side) as expressed in fig. 4.3.

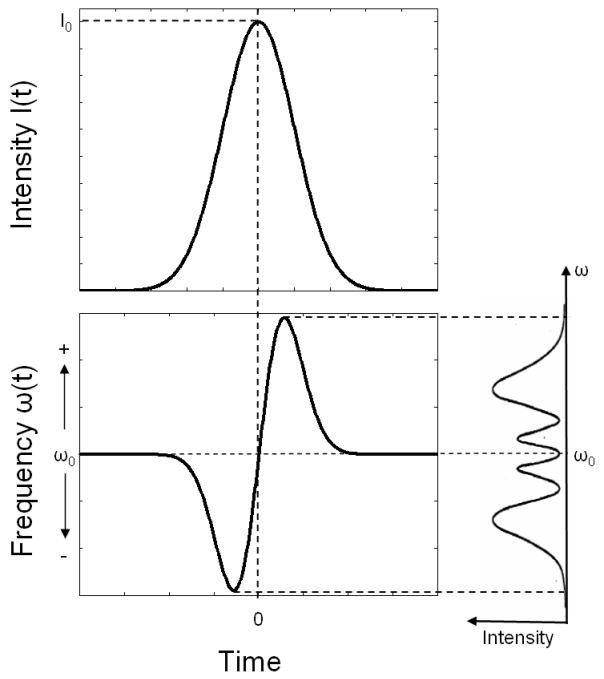

Figure 4.3: Effect of SPM on a gaussian input pulse: modification of the spectrum due to nonlinear phase shift.

Therefore the SPM could broaden the input spectrum by a factor $\delta\omega_{MAX}$, defined as the maximum of $\delta\omega(t)$ [7]:

$$\delta\omega_{MAX} \approx 0.86\,\Delta\omega_0\,\phi_{MAX}, \tag{4.13}$$

where $\Delta\omega_0$ is the $1/e$ half-width of the initial spectrum. The maximum spectral broadening is proportional to the numerical value of the maximum nonlinear phase shift ϕ_{MAX}.

4.3.2 Cross-phase modulation

If two waves, at different carrier wavelengths λ_1 and λ_2, travel simultaneously in the fibre, the nonlinear refractive index of the wave 1 is influenced by the intensity of both waves. This effect is called cross-phase modulation (XPM) and may be as twice as large than the SPM in a scalar model. Indeed when a field is constituted of two frequencies, the instantaneous intensity is composed of two part: two constant values related to the intensity of the two frequencies taken singularly plus two terms beating at the frequency detuning between the two channels. In a third order interaction these last terms provide a double effects of refractive index change for the same value of intensity per channel. Note that in principle both SPM and XPM have no direct equivalent in a $\chi^{(2)}$ crystal. Due to XPM the nonlinear phase of the wave 1 is:

$$\phi^1_{NL}(t) = \frac{2\pi}{\lambda} n_2 L \left[I_1(t) + 2I_2(t)\right]. \tag{4.14}$$

The same behaviour is expressed in the NLSE (still in the limit of the instantaneous response of the medium):

$$\begin{aligned} &\frac{\partial A_1(z,t)}{\partial z} - \sum_{n\geq 2} \beta_n \frac{i^{n+1}}{n!} \frac{\partial^n A_1(z,t)}{\partial t^n} + \frac{\alpha}{2} A_1(z,t) = \\ &\imath\gamma_1 \left[\underbrace{|A_1(z,t)|^2}_{\textbf{SPM}} + \underbrace{2|A_2(z,t)|^2}_{\textbf{XPM}} \right] A_1(z,t). \end{aligned} \tag{4.15}$$

4.3.3 Four wave mixing

The four-wave mixing (FWM) is a nonlinear process due to the third order nonlinear susceptibility, where the mixing of photons generates photons at different frequencies. This parametric generation is only observable if there is a matching between the different phase velocities of the waves and if the total energy is conserved. *FWM is the conceptual analog for fibre of the TWRI developed in the chapter 1 for nonlinear crystals. By following the same procedure one could formulate four (instead of three) coupled equations in which frequency conversion of pulse waveforms occurs only when a condition of temporal superposition is satisfied. In this context nonlinear interactions are limited by temporal walk-off while all waves have wavevectors oriented in the same direction. We now limit first our analysis to four monochromatic waves.* Two types of FWM exist. In the first one, the mixing of three photons at three different pulsations ω_1, ω_2, ω_3, gives rise to a fourth photon with angular frequency $\omega_4 = \omega_1 + \omega_2 + \omega_3$. This effect permits, for example, to explain the third-harmonic generation process in optical fibre. This type of FWM is difficult to obtain because of the phase matching condition which is not well satisfied in optical fibres. The second type of FWM permits the generation of two photons at frequency ω_3 and ω_4 from two photons ω_1 and ω_2 pertaining to two pump waves. This process is schematically represented in fig. 4.4(a). The scalar phase matching and the energy conservation condition read as:

$$\omega_1 + \omega_2 = \omega_3 + \omega_4, \quad \mathbf{k}_1 + \mathbf{k}_2 = \mathbf{k}_3 + \mathbf{k}_4. \tag{4.16}$$

The waves at ω_3 and ω_4 (assuming $\omega_3 > \omega_4$) are usually called Stokes and anti-Stokes waves. When the two pump waves are at the same frequency ω_1 the process is called degenerate FWM (see fig. 4.4(b)).

In the limit of the instantaneous response of the medium, the NLSE for

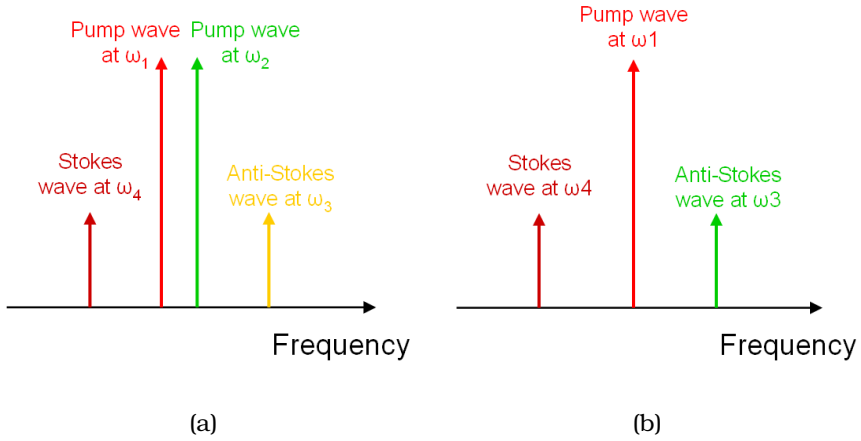

Figure 4.4: Schematic representation of FWM in the case with (a) two pump waves and (b) with only one pump wave (degenerate case).

field $A_1(z,t)$ read as:

$$\begin{aligned}\frac{\partial A_1(z,t)}{\partial z} - \sum_{n\geq 2}\beta_n \frac{i^{n+1}}{n!}\frac{\partial^n A_1(z,t)}{\partial t^n} + \frac{\alpha}{2}A_1(z,t) = \\ = \imath\gamma_1\left[\left(\underbrace{|A_1(z,t)|^2}_{\textbf{SPM}} + \underbrace{2|A_2(z,t)|^2}_{\textbf{XPM}}\right)A_1(z,t) + \right. \\ \left. + \underbrace{2A_2^*(z,t)A_3(z,t)A_4(z,t)e^{\imath(\mathbf{k}_3+\mathbf{k}_4-\mathbf{k}_1-\mathbf{k}_2)z}}_{\textbf{FWM}}\right]\end{aligned} \tag{4.17}$$

4.3.4 Modulation instability

Modulation instability (MI) is a noise-seed nonlinear phenomenon due to the interplay between SPM and dispersion which leads to the break-up of an input pulse. It was first discovered in fibres in 1986 [9], but MI can also be found in many areas of physics such as plasma waves and water surface waves [10, 11]. This phenomenon takes place only in the anomalous GVD region. Other forms of conditional stability arise in specific conditions involving polarization, high order dispersion and multiple pumps. MI can be interpreted as degenerate FWM in anomalous dispersion regime, where the phase matching is obtained thanks to the compensation of the linear

phase mismatch with SPM. Quasi CW pulses break-up and generate a train of pulses. A signature of this modulation is seen in the optical spectrum by the appearance of two symmetrically distributed sidelobes around the pump (see fig. 4.5). The frequency shift between the pump and the MI

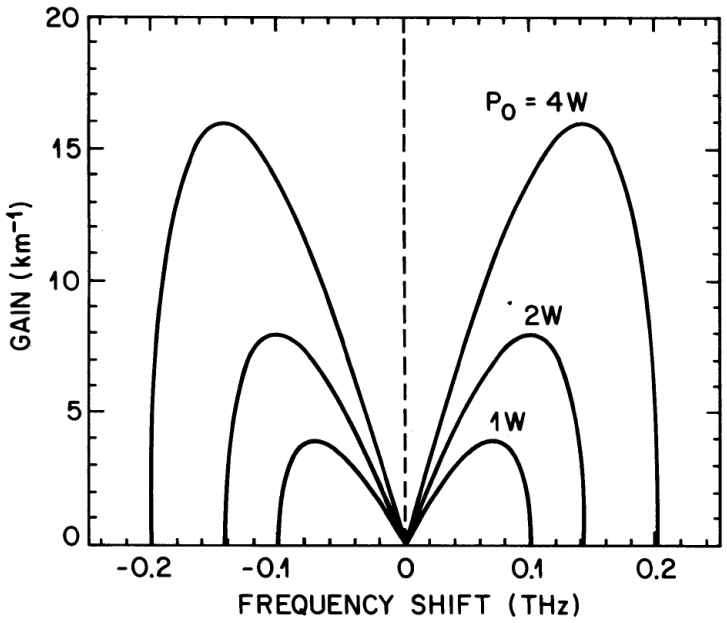

Figure 4.5: Gain spectra of modulation instability at three power levels with $\beta_2 = -20ps^2/km$ and $\gamma = 2W^{-1}/km$ [7].

gain frequencies is equal to the repetition rates of the pulses created in the break-up of the initial pulse. Neglecting high order effects, it is possible to predict the angular frequency shift of the peak of the MI gain using the following expression [7]:

$$\Omega_{max} = \pm\sqrt{\left(\frac{2\gamma P_0}{|\beta_2|}\right)}, \tag{4.18}$$

where Ω_{max} is the angular frequency detuning of the maximum gain from the pump.

4.3.5 Inelastic phenomena

The nonlinear response of the material is very fast but is not instantaneous. One part of the nonlinear response comes from the vibrational modes of the medium with a finite response time. When this vibration is associated with optical phonons, the phenomenon is called Stimulated Raman scattering (SRS). SRS is a nonlinear process due to the interaction between photons and phonons. It can transfer a fraction of power from one optical field to another field, whose frequency is downshifted (Stokes side) by an amount determinated by the vibrational modes of the medium. Molecules may absorb photons by changing their vibrational state. Differently from an other type of scattering (Rayleigh) the re-emitted photons may have different energies. For this reason this type of nonlinear scattering is called inelastic. Raman scattering can also transfer energy from a pump field to another field upshifted in frequency (anti-Stokes side), but this process is less efficient (in terms of emission probability) than the Stokes case, because it needs to take energy from the medium. The energy exchange, between the pump and the medium, is represented in fig. 4.6. The processes of Stokes and anti-Stokes generation may have a spontaneous counterpart, which is characterized by a small energy transfer. The energy transfer in silica medium is maximum for $\Delta\omega_R = \omega_p - \omega_S = 13.2THz$. This value corresponds to the peak value of the Raman gain spectrum (fig. 4.7(a)). *Differently from the case of short crystals SRS plays an important role in nonlinear optics in fibre due to the long interaction between light and matter. However if we focus our attention to the system of coupled equations between pump, Raman Stokes and anti-Stokes we find again a coupled system of three-wave mixing equations as those described in chapter 1. Despite the physical mechanism are different, the mathematical model of three-wave mixing has a sort of generality in nonlinear optics.* From a time domain point of view, the Raman effect is interpreted as the delayed nonlinear response of the medium. In this condition, the nonlinear polar-

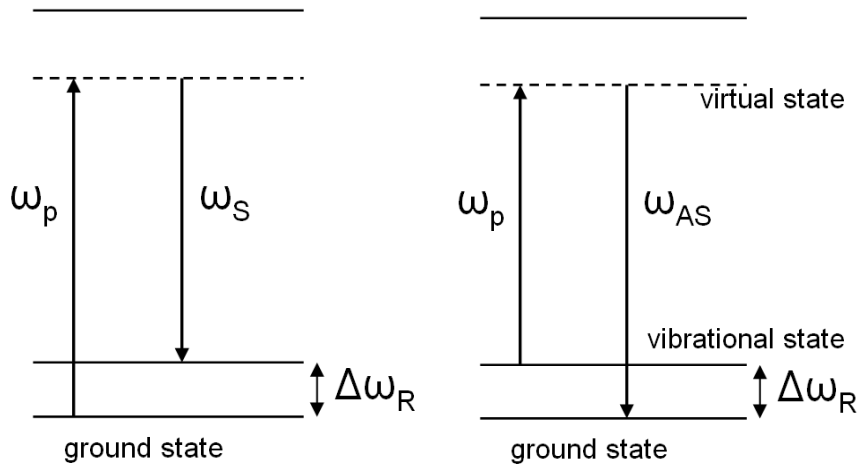

Figure 4.6: Energy level diagrams for (a) Stokes Raman scattering and (b) anti-Stokes Raman scattering.

ization corresponding to the Raman effect is:

$$\mathbf{P}_R^{(3)}(t) = \varepsilon_0 \mathbf{E}(\mathbf{r},t) \int_{-\infty}^{t} h_R(t-\tau)|\mathbf{E}(\mathbf{r},\tau)|^2 d\tau, \tag{4.19}$$

where the integral is calculated from $-\infty$ to t to satisfy causality: $h_R(t)$ is equal to zero for $\tau > t$. In the case of SRS, where we have to consider two waves (pump and Stokes), the total electric field is:

$$\mathbf{E}(\mathbf{r},t) = \frac{1}{2}\left[E_p(z,t)e^{\imath(k_p z-\omega_p t)} + E_S(z,t)e^{\imath(k_S z-\omega_S t)}\right]\mathbf{e}, \tag{4.20}$$

Substituting eq. 4.20 in eq. 4.19 and taking in consideration only the terms involved in the Raman effect, in the case of slowly varying envelope approximation, the coupled propagation equation considering only the Stokes wave read as (one for the pump and one for the Stokes):

$$\begin{aligned}
\frac{\partial A_p(z,t)}{\partial z} &= \imath\gamma_{R,p} A_S(z,t) \int_{-\infty}^{t} h_R(t-\tau) e^{-\imath\Omega_{pS}(t-\tau)} A_S^*(z,\tau) A_p(z,\tau) d\tau \\
\frac{\partial A_S(z,t)}{\partial z} &= \imath\gamma_{R,S} A_p(z,t) \int_{-\infty}^{t} h_R(t-\tau) e^{-\imath\Omega_{Sp}(t-\tau)} A_p^*(z,\tau) A_S(z,\tau) d\tau
\end{aligned} \tag{4.21}$$

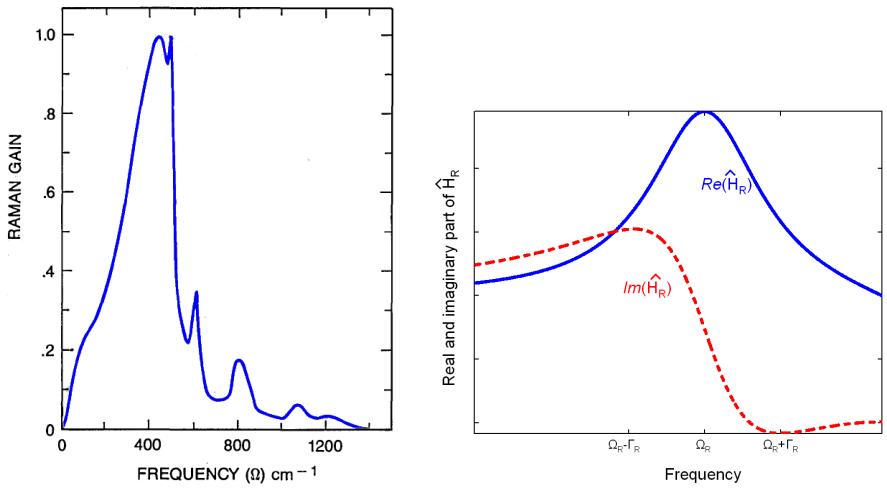

(a) (b)

Figure 4.7: (a) Measured Ramain gain curve ($Im(\widehat{H}_R)$ [12] and (b) calculated real and imaginary part of $\widehat{H}_R$.

where $\gamma_R = \frac{g_R \Gamma_R}{\Omega_R}$ and $\Omega_{pS} = \omega_p - \omega_S = -\Omega_{Sp}$. The coefficient g_R, Γ_R and Ω_R represent the Raman gain, the bandwidth of the Raman response and the Raman resonance frequency. The temporal Raman response is:

$$h_R(t) = \Omega_R^2 \tau_1 e^{\frac{-t}{\tau_2}} \sin(\frac{t}{\tau_1}) \tag{4.22}$$

where $\tau_2 = \frac{1}{\Gamma_R}$ and $\tau_1 = \frac{1}{(\Omega_R^2 - \Gamma_R^2)^{1/2}} \approx \frac{1}{\Omega_R}$ are two parameters and they have been chosen to provide a good fit to the Raman gain spectrum (fig. 4.7(a)). The values used in this manuscript are $\tau_1 = 12.2fs$ and $\tau_2 = 32fs$ [13]. The Raman response spectrum is obtained by Fourier transform of eq: 4.22:

$$\widehat{H}_R(\Omega) = \frac{\Omega_R^2}{\Omega_R^2 - \Omega^2 - 2\imath\Gamma_R\Omega}. \tag{4.23}$$

The real part of $\widehat{H}_R(\Omega)$ modifies the refractive index, while the imaginary part represents the gain as shown in fig. 4.7(b). The Raman effect can be

also integrated in the NLSE in the following form:

$$\frac{\partial A(z,t)}{\partial z} - \sum_{n\geq 2} \beta_n \frac{i^{n+1}}{n!} \frac{\partial^n A(z,t)}{\partial t^n} + \frac{\alpha}{2} A(z,t) = \\ = \imath\gamma \left(1 + \frac{\imath}{\omega_0}\frac{\partial}{\partial t}\right) \left(\underbrace{A(z,t) \int_0^{+\infty} R(\tau) |A(z,t-\tau)|^2 d\tau}_{\textbf{Raman effect}} \right). \tag{4.24}$$

where the terms proportional to $\frac{\imath}{\omega_0}\frac{\partial}{\partial t}$ takes into consideration the variation of the γ coefficient upon frequency.

4.3.6 Solitonic effects

When an optical fibre is pumped in the normal dispersion region ($D < 0$ and $\beta_2 > 0$), the SPM spectral broadening stops when the dispersion has spread the pulse. With PCFs it is possible to shift the zero dispersion wavelength toward the short wavelengths so as to make easy to inject a laser beam in the anomalous dispersion region ($D > 0$ and $\beta_2 < 0$). When a fibre is pumped in the anomalous dispersion region, the competition between dispersion and non-linearity may even balance giving rise to the formation of solitons. *Such solitons have a single wavelengths and they are not multicolor solutions as simulton described in chapter 1.* Optical fibre solitons are particular waves able to propagate without any deformation inside the fibre. We can explain the soliton formation considering that the only nonlinear effect involved is the SPM. More precisely, the spectral blue components, created on the trailing edge of the pulse by SPM, travel faster then the red components, and they are shifted to the leading edge of the pulse. Hence, if the phase induced by SPM compensates exactly the phase introduced by the dispersion, a wave propagating without changes in spectral profile and time duration is created. Such kind of wave is called soliton.

Considering only the group velocity dispersion (terms β_2 in eq. 4.3) and

the SPM, the NLSE take the form:

$$\frac{\partial A(z,t)}{\partial z} = -\beta_2 \frac{i}{2} \frac{\partial^2 A(z,t)}{\partial t^2} + \imath\gamma A(z,t)|A(z,t)|^2, \tag{4.25}$$

with $\beta_2 < 0$ and $\gamma > 0$. The soliton is a specific solution of the equation 4.25, and is defined as:

$$A(z,t) = \sqrt{P_0}\,\mathrm{sech}\left(\frac{t}{T_0}\right) e^{\imath\frac{z}{2L_D}}, \tag{4.26}$$

where P_0 is the peak power, T_0 is the soliton time width and L_D is the dispersion length defined in eq. 4.10. In solitons context, it is useful to normalize eq. 4.25 in soliton units, by introducing three dimensionless variables directly related to soliton features like peak power, dispersion length or temporal width:

$$U = \frac{A}{\sqrt{P_0}}, \;\; \xi = \frac{z}{L_D}, \;\; \tau = \frac{t}{T_0}, \tag{4.27}$$

so it is possible to write the NLSE in the following normalized form:

$$\imath\frac{\partial U}{\partial \xi} = \mathrm{sgn}(\beta_2)\frac{1}{2}\frac{\partial^2 U}{\partial \tau^2} - N^2|U|^2U, \tag{4.28}$$

where N is defined as

$$N^2 = \frac{L_D}{L_{NL}} = \frac{\gamma P_0 T_0^2}{|\beta_2|}. \tag{4.29}$$

The dispersion length L_D and the nonlinear length L_{NL} are defined in eq. 4.10. The parameter N represents the soliton order: a first order soliton (fundamental soliton) is obtained when L_D is equal to L_{NL} and high order soliton when L_D is greater then L_{NL}. First order solitons are able to propagate inside the fibre without any type of temporal and spectral deformation because the dispersive and nonlinear effects exactly compensate each other. Otherwise, a high order soliton is periodic in ξ with period

$\xi_0 = \frac{\pi}{2}$. In the normalized units the soliton period z_0 is:

$$z_0 = \frac{\pi}{2} L_D = \frac{\pi}{2} \frac{T_0^2}{|\beta_2|}. \tag{4.30}$$

This characteristic of high order solitons is called "breathing": the soliton, during its propagation, undergoes a periodic compression and broadening in time domain. This effect is shown in fig. 4.8 for a third order soliton.

High order solitons may be described as several fundamental solitons

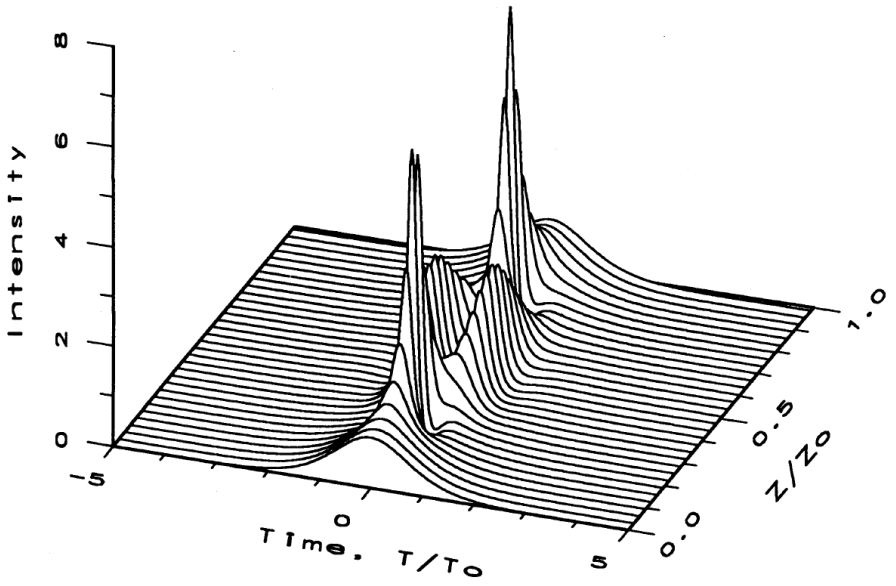

Figure 4.8: Temporal evolution of a third order soliton (N=3) over one soliton period [7].

which propagate in coupled manner [14], so a soliton of Nth order is composed by N fundamental solitons. The peak power and the temporal duration of each of these solitons are defined as:

$$P_k = \frac{(2N - 2k + 1)^2}{N^2} P_0 \ \ and \ \ T_k = \frac{T_0}{2N - 2k + 1}, \tag{4.31}$$

where $k = 1...N$ denote the k^{th} fundamental soliton constituting the soliton of order N with peak power P_0 and time duration T_0. These fundamental solitons have the same group velocity in absence of any perturbation dur-

ing its propagation, so the high order soliton can breath. If some perturbation affect the soliton propagation, this state of equilibrium can break. Ones of the effects responsible for this break up are the third and fourth order dispersion. High order solitons can then break into their N constituting fundamental solitons. This effect is the so called soliton fission or soliton break-up. It is possible to define a length for which the soliton fission takes place:

$$L_{fission} = \frac{L_D}{N}. \tag{4.32}$$

A soliton, propagating in an optical fibre, is subject not only to the Kerr effects which compensate the dispersion, but also to Raman effect. Indeed, when the soliton spectrum is so broad (typically for time duration $T_0 < 100fs$) to overlap the Raman gain spectrum, the longer-wavelength components experience Raman amplification to the detriment of the shorter wavelengths. This effect is called soliton self-frequency shift (SSFS), and causes an overall spectral shift of the soliton toward longer wavelengths. The strength of this effect depends strongly on the pulse duration, since shorter solitons exhibit a higher peak power and a broader optical spectrum. The latter is important because of the Raman gain is weak for small frequency offsets. During propagation, the rate of the frequency shift often slows down, because the pulse energy is reduced and the pulse duration increased due to losses inside the fibre. SSFS was first discovered in 1986 by Mitschke [15] and modelled by Gordon in the same year [16]. In particular the work done by Gordon shows that the frequency shift $\Delta\nu_0$ experienced by a soliton with time width T_0 after a distance z is:

$$\Delta\nu_0 = \frac{\lambda^2 D(\lambda) q(T_0) z}{T_0^4}, \tag{4.33}$$

where $D(\lambda)$ is the chromatic dispersion at the soliton carrier wavelength λ and $q(T_0)$ is the overlapping function between the soliton spectrum and the Raman spectrum.

Differently from multi-component solitons described in chapter 2, it is dif-

ficult to study the existence of multi-soliton solution in fibre. However we cannot deny that multiple self sustained solitons may interact one with each other giving rise to new frequency components.

4.4 Supercontinuum generation

The temporal as well as spectral evolution of optical pulses, propagating inside a highly nonlinear fibre, is affected not only by a multitude of nonlinear effects such as SPM, XPM, FWM and SRS, but also by the dispersive properties within the pulse spectrum. For sufficiently intense pulses, through the interaction of many nonlinear processes, the pulse spectrum may become extremely broad. Such extreme spectral broadening is referred to as supercontinuum generation (SC).

4.4.1 Hystorical review

The first remarkable spectral broadening of quasi-monochromatic laser pulse was obtained by Stoicheff in 1963, in a liquid medium [17]. However the attention of the scientists on this subject was attracted ten years later when Alfano and Shapiro demonstrated, for the first time, the generation of spectra ten times larger then the input one [18]. The experiment was carried out pumping a borosilicate glass (BK-7) with picoseconds pump pulse, obtaining an output spectra extended till the visible region. It is only in 1984 that the terms "supercontinuum" was coined by Manassah [19]. From the first demonstration, several investigation groups developed research concerning SC generation in different medium such as liquid, gas and solid [20–27]. The experiments were focused on the understanding of the physical phenomena which SC is based on, and several mathematical models were developed to explain the role played by the nonlinear effects involved in SC generation [28–32]. However, many points remained to be clarified on the global development of SC. It's in the 80s that the SC attract more interest. Indeed, because of optical fibre, is it possible to obtain

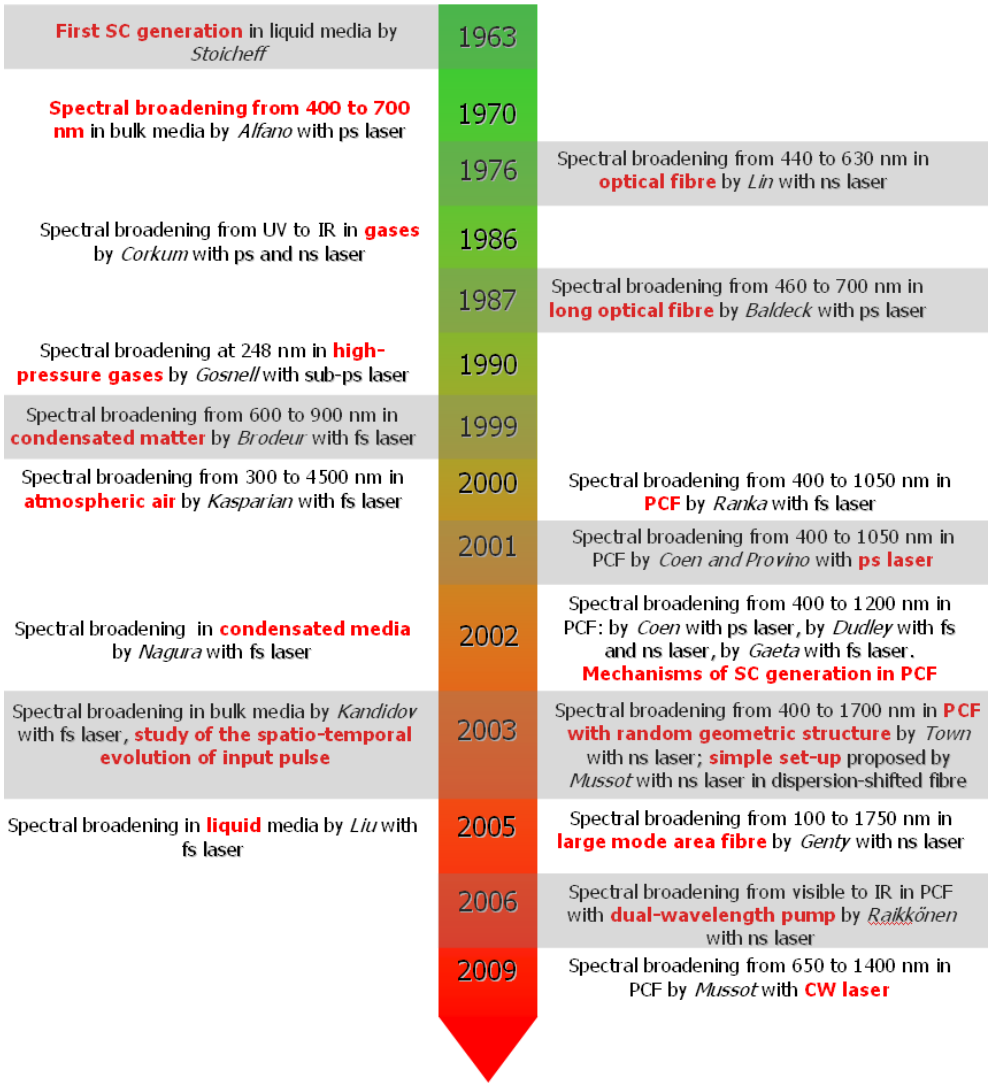

Figure 4.9: Chronological history of the main results (in red) concerning the SC generation.

wider spectral broadening but also to control some guide's features , for instance chromatic dispersion. The first SC generation in optical fibre was reported by Lin and Stolen [33], after that many effort have been done to achieve the simplest configuration that allows one to generate SC [34, 35]. Another important stage in the SC generation's history, is the invention of the photonic crystal fibre (PCF). The first report on PCFs was presented by Knight in 1996 [36]. As discussed in the previous chapter, these fibres

allow to reduce the fibre length and the peak power request for SC generation. Indeed, it is possible to control the nonlinear coefficient so as to increase the impact of nonlinear effects. In 2000, Ranka demonstrated the potential of PCF in SC generation [37]. After that many research groups have investigated on the characteristic of the SC spectra and on the nonlinear effects involved in the propagation [38–41].

Over the last decade, this effect has attracted much attention because of applications in many different fields, such as laser-frequency metrology, biology or medical imaging [42, 43]. In fig. 4.9 the main historical researches in SC generation are resumed, showing in red the most important results.

4.4.2 Specificity of pumping regimes

Spectral broadening over a spectral range of several hundreds of nano meters are been observed in nanosecond, picosecond and femtosecond, and also in a continuous wave (or quasi-continuous wave) regimes. Each type of excitation differs from the others in terms of nonlinear process involved, temporal and spectral characteristics. In SC generation, the type of excitation permits to control the importance of nonlinear effects respect to the dispersion effects. The ZDW of the fibre is another important parameter in SC generation process, which determine if the pump is in anomalous or normal dispersion region. In general, an efficient SC generation is obtained pumping the fibre close the ZDW because of the low impact of the dispersion on the powerful pulse shape.

Since the early experiences of SC generation using femtosecond pump lasers [37], alternative regimes of inputs have been investigated to cover a full range of possible durations including picosecond, nanosecond and CW laser sources which potentially benefit from more compactness and low costs [38, 44, 45]. The CW laser source delivers smaller peak power than the pulsed laser. In order to counteract this difference, it is essential

to use very long highly nonlinear fibre. This is exactly what Avdokhin [46] demonstrated in 2003 using a CW laser source pumping in the anomalous dispersion region, obtaining high spectral density (12 mW/nm) and a spectral broadening higher than 400 nm. The first experiment in the nanosecond regime was carried out by Lin and Stolen in 1976 [33], which has opened a new research interest. A major effort was done demonstrating the interest to use different laser sources and different optical fibers [47–50], with the purpose to obtain a SC with high average power. The picosecond regime permits to control the spectral evolution highlighting the non-linearity (with shorter fibre length) or increasing the dispersion (with longer fibre length) [51]. But these different time durations are usually associated with qualitatively different nonlinear mechanisms.

Femtosecond regime

The femtosecond regime has been extensively studied with the advent of PCFs. Because of the possible control of ZDW position, it is possible to pump the PCF close to it. This allows to preserve the peak power of the ultra-short pulse over a distance of several centimeters. Indeed, with such kind of pulse (generated by a Ti:sapphire or ytterbium doped fibre lasers), it is possible to obtain very high peak power (> 15 kW) that leads to the generation of very broad spectrum. The temporal profile is composed by multiple sub-pulses whereas the spectral profile is not flat, as shown in fig. 4.10. The main nonlinear processes involved in this regime of propagation are SPM, solitonic effects, SSFS and dispersive wave generation [52]. Initially, the pulse is injected into the fibre in the anomalous dispersion region and close to the ZDW, and propagates as a high order soliton. In the first centimeters of the fibre, the pulse experiences a spectral broadening due to SPM (fig. 4.10 left, label A). This spectral broadening is accompanied by temporal compression. The perturbation induced by high order dispersion and by SRS leads to the break-up of N-order soliton into N fun-

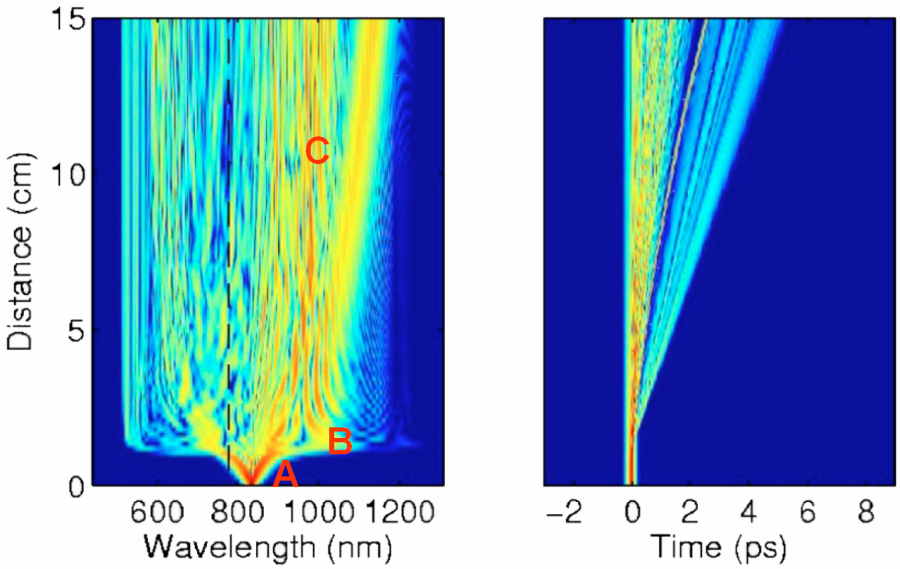

Figure 4.10: Numerical simulation showing SC spectral and temporal evolution with a pump pulse with duration (FWHM) of 100 fs (with peak power of 10 kW and pump wavelength of 835 nm. The dashed line shows the fibre ZDW [42].

damental solitons with different time duration and peak power as defined in eq. 4.31 (fig. 4.10 left, label B). Now, the central wavelengths of the fundamental solitons are shifted toward IR region due to SSFS (fig. 4.10 left, label C). So, each fundamental soliton has different central wavelength and different group velocity, depending on the time duration and the peak power. The soliton that experience the largest frequency shift and the bigger time delay is the fundamental soliton which has the shortest time duration and the highest peak power. In that regime of excitation, the lowest wavelengths propagating in the normal dispersion regime are mainly created by dispersive wave generation [52].

Picosecond, nanosecond, continuous-wave regimes

For longer pulse (from picosecond to continuous-wave) the IR supercontinuum generation process cannot be explained in terms of SPM or soliton fission only. Indeed for longer excitation pulse located in the anomalous

dispersion regime, the SPM starts first followed by MI [42]. Because MI process is based on amplification of noise and not of the pump itself, the coherence of the output pulse is drastically damaged. The periodicity of MI impose the soliton number and rate whereas the total energy obtained in an MI period is confined into a single soliton. This will produce a distribution of fundamental soliton with peak power higher than the pump pulse (fig. 4.11 left). Generally, the strongest soliton is created in the central part of the pump pulse, where the peak power is higher. In a second step, the fundamental solitons starts to red shift due to Raman gain effect.

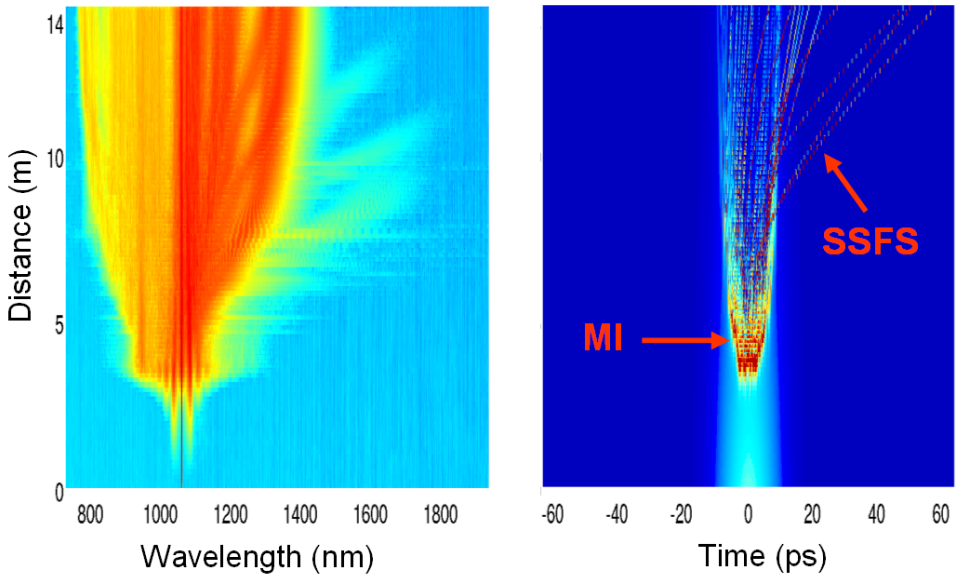

Figure 4.11: Numerical simulation showing SC spectral and temporal evolution with a pump pulse with duration (FWHM) of 16 ps (with peak power of 300 W and pump wavelength of 1060 nm and ZDW at 1025 nm).

Bibliography

[1] J.C. Knight. Photonic crystal fibres. *Nature*, 424(6950):847–851, August 2003.

[2] J.C. Knight, T.A. Birks, P.St.J. Russell, and D.M. Atkin. All-silica single-mode optical fiber with photonic crystal cladding. *Optics Letters*, 21(19):1547, October 1996.

[3] J.C. Knight, T.A. Birks, P.St.J. Russell, and D.M. Atkin. All-silica single-mode optical fiber with photonic crystal cladding: errata. *Optics Letters*, 22(7):484, April 1997.

[4] P. Russell. Photonic crystal fibers. *Science*, 299(5605):358–362, January 2003.

[5] T.A. Birks, J.C. Knight, and P.St.J. Russell. Endlessly single-mode photonic crystal fiber. *Optics Letters*, 22(13):961, July 1997.

[6] V. Tombelaine. Etude de rayonnements à large bande spectrale induits dans les fibres optiques microstructurées air-silice. *PhD Thesis*, 2007.

[7] G. Agrawal. *Nonlinear fiber optics*. Academic Press, San Diego, 2nd ed. edition, 1995.

[8] N.A. Mortensen. Effective area of photonic crystal fibers. *Optics Express*, 10(7):341–348, 2002.

[9] K. Tai, A. Hasegawa, and A. Tomita. Observation of modulational instability in optical fibers. *Physical Review Letters*, 56(2):135–138, January 1986.

[10] T.B. Benjamin and K. Hasselmann. Instability of periodic wavetrains in nonlinear dispersive systems. *Proceedings of the Royal Society A:*

Mathematical, Physical and Engineering Sciences, 299(1456):59–76, June 1967.

[11] A. Hasegawa. Observation of Self-Trapping instability of a plasma cyclotron wave in a computer experiment. *Physical Review Letters*, 24(21):1165–1168, May 1970.

[12] R.H. Stolen, J.P. Gordon, W.J. Tomlinson, and H.A. Haus. Raman response function of silica-core fibers. *Journal of the Optical Society of America B*, 6(6):1159, June 1989.

[13] K.J. Blow and D. Wood. Theoretical description of transient stimulated raman scattering in optical fibers. *IEEE Journal of Quantum Electronics*, 25(12):2665–2673, December 1989.

[14] Y. Kodama and A. Hasegawa. Nonlinear pulse propagation in a monomode dielectric guide. *IEEE Journal of Quantum Electronics*, 23(5):510–524, May 1987.

[15] F.M. Mitschke and L.F. Mollenauer. Discovery of the soliton self-frequency shift. *Optics Letters*, 11(10):659, October 1986.

[16] J.P. Gordon. Theory of the soliton self-frequency shift. *Optics Letters*, 11(10):662, October 1986.

[17] B. Stoicheff. Characteristics of stimulated raman radiation generated by coherent light. *Physics Letters*, 7(3):186–188, November 1963.

[18] R. Alfano and S. Shapiro. Emission in the region 4000 to 7000 Å via Four-Photon coupling in glass. *Physical Review Letters*, 24(11):584–587, March 1970.

[19] J.T. Manassah, P.P. Ho, A. Katz, and R.R. Alfano. Ultrafast supercontinuum laser source. *Photonics spectra*, 18:53, 1984.

[20] R. Alfano and S. Shapiro. Observation of Self-Phase modulation and Small-Scale filaments in crystals and glasses. *Physical Review Letters*, 24(11):592–594, March 1970.

[21] P. Corkum, C. Rolland, and T. Srinivasan-Rao. Supercontinuum generation in gases. *Physical Review Letters*, 57(18):2268–2271, November 1986.

[22] T.R. Gosnell, A.J. Taylor, and D.P. Greene. Supercontinuum generation at 248 nm using high-pressure gases. *Optics Letters*, 15(2):130, January 1990.

[23] A. Brodeur and S.L. Chin. Ultrafast white-light continuum generation and self-focusing in transparent condensed media. *Journal of the Optical Society of America B*, 16(4):637, April 1999.

[24] J. Kasparian, R. Sauerbrey, D. Mondelain, S. Niedermeier, J. Yu, J.-P. Wolf, Y.-B. André, M. Franco, B. Prade, S. Tzortzakis, A. Mysyrowicz, M. Rodriguez, H. Wille, and L. Wöste. Infrared extension of the super continuum generated by femtosecond terawatt laser pulses propagating in the atmosphere. *Optics Letters*, 25(18):1397, September 2000.

[25] C. Nagura, A. Suda, H. Kawano, M. Obara, and K. Midorikawa. Generation and characterization of ultrafast White-Light continuum in condensed media. *Applied Optics*, 41(18):3735, June 2002.

[26] V.P. Kandidov, O.G. Kosareva, I.S. Golubtsov, W. Liu, A. Becker, N. Akozbek, C.M. Bowden, and S.L. Chin. Self-transformation of a powerful femtosecond laser pulse into a white-light laser pulse in bulk optical media (or supercontinuum generation). *Applied Physics B: Lasers and Optics*, 77(2-3):149–165, September 2003.

[27] J. Liu, H. Schroeder, S.L. Chin, R. Li, and Z. Xu. Nonlinear propagation of fs laser pulses in liquids and evolution of supercontinuum generation. *Optics Express*, 13(25):10248, 2005.

[28] G. Yang and Y.R. Shen. Spectral broadening of ultrashort pulses in a nonlinear medium. *Optics Letters*, 9(11):510, November 1984.

[29] A. Zozulya, S. Diddams, A. Van Engen, and T. Clement. Propagation dynamics of intense femtosecond pulses: Multiple splittings, coalescence, and continuum generation. *Physical Review Letters*, 82(7):1430–1433, February 1999.

[30] T. Brabec and F. Krausz. Intense few-cycle laser fields: Frontiers of nonlinear optics. *Reviews of Modern Physics*, 72(2):545–591, April 2000.

[31] C. Conti, S. Trillo, P. Di Trapani, G. Valiulis, A. Piskarskas, O. Jedrkiewicz, and J. Trull. Nonlinear electromagnetic X waves. *Physical Review Letters*, 90(17), May 2003.

[32] G. Méchain, A. Couairon, M. Franco, B. Prade, and A. Mysyrowicz. Organizing multiple femtosecond filaments in air. *Physical Review Letters*, 93(3), July 2004.

[33] C. Lin and R.H. Stolen. New nanosecond continuum for excited-state spectroscopy. *Applied Physics Letters*, 28(4):216, 1976.

[34] I. Ilev, H. Kumagai, K. Toyoda, and I. Koprinkov. Highly efficient wideband continuum generation in a single-mode optical fiber by powerful broadband laser pumping. *Applied Optics*, 35(15):2548, May 1996.

[35] A. Mussot, T. Sylvestre, L. Provino, and H. Maillotte. Generation of a broadband single-mode supercontinuum in a conventional dispersion-shifted fiber by use of a subnanosecond microchiplaser. *Optics Letters*, 28(19):1820, October 2003.

[36] J.C. Knight, T.A. Birks, Ph.St.J. Russell, and D.M. Atkin. All-silica single-mode optical fiber with photonic crystal cladding. *Optics Letters*, 21(19):1547, October 1996.

[37] J.K. Ranka, R.S. Windeler, and A.J. Stentz. Visible continuum generation in air-silica microstructure optical fibers with anomalous dispersion at 800 nm. *Optics Letters*, 25(1):25, January 2000.

[38] S. Coen, A.H.L. Chau, R. Leonhardt, J.D. Harvey, J.C. Knight, W.J. Wadsworth, and Ph.St.J. Russell. White-light supercontinuum generation with 60-ps pump pulses in a photonic crystal fiber. *Optics Letters*, 26(17):1356, September 2001.

[39] S. Coen, A.H.L. Chau, R. Leonhardt, J.D. Harvey, J.C. Knight, W.J. Wadsworth, and Ph.St.J. Russell. Supercontinuum generation by stimulated raman scattering and parametric four-wave mixing in photonic crystal fibers. *Journal of the Optical Society of America B*, 19(4):753, April 2002.

[40] J.M. Dudley, L. Provino, N. Grossard, H. Maillotte, R.S. Windeler, B.J. Eggleton, and S. Coen. Supercontinuum generation in airâĂŞsilica microstructured fibers with nanosecond and femtosecond pulse pumping. *Journal of the Optical Society of America B*, 19(4):765, April 2002.

[41] A.L. Gaeta. Nonlinear propagation and continuum generation in microstructured optical fibers. *Optics Letters*, 27(11):924, June 2002.

[42] J.M. Dudley and S. Coen. Supercontinuum generation in photonic crystal fiber. *Reviews of Modern Physics*, 78(4):1135–1184, October 2006.

[43] I. Hartl, X.D. Li, C. Chudoba, R.K. Ghanta, T.H. Ko, J.G. Fujimoto, J.K. Ranka, and R.S. Windeler. Ultrahigh-resolution optical coherence tomography using continuum generation in an airâĂŞsilica microstructure optical fiber. *Optics Letters*, 26:608, May 2001.

[44] E. Raikkönen, G. Genty, O. Kimmelma, M. Kaivola, K.P. Hansen, and S.C. Buchter. Supercontinuum generation by nanosecond dual-

wavelength pumping in microstructured optical fibers. *Optics Express*, 14(17):7914, 2006.

[45] A. Mussot and A. Kudlinski. 19.5 w CW-pumped supercontinuum source from 0.65 to 1.38 μ m. *Electronics Letters*, 45(1):29, 2009.

[46] A.V. Avdokhin, S.V. Popov, and J.R. Taylor. Continuous-wave, high-power, raman continuum generation in holey fibers. *Optics Letters*, 28(15):1353, August 2003.

[47] L. Provino, J.M. Dudley, H. Maillotte, N. Grossard, R.S. Windeler, and B.J. Eggleton. Compact broadband continuum source based on microchip laser pumped microstructured fibre. *Electronics Letters*, 37(9):558, 2001.

[48] P.A. Champert, S.V. Popov, M.A. Solodyankin, and J.R. Taylor. Multiwatt average power continua generation in holey fibers pumped by kilowatt peak power seeded ytterbium fiber amplifier. *Applied Physics Letters*, 81(12):2157, 2002.

[49] G.E. Town, T. Funaba, T. Ryan, and K. Lyytikainen. Optical supercontinuum generation from nanosecond pump pulses in an irregularly microstructured air-silica optical fiber. *Applied Physics B: Lasers and Optics*, 77(2-3):235–238, September 2003.

[50] G. Genty, T. Ritari, and H. Ludvigsen. Supercontinuum generation in large mode-area microstructured fibers. *Optics Express*, 13(21):8625, 2005.

[51] P. Baldeck and R. Alfano. Intensity effects on the stimulated four photon spectra generated by picosecond pulses in optical fibers. *Journal of Lightwave Technology*, 5(12):1712–1715, 1987.

[52] N. Akhmediev and M. Karlsson. Cherenkov radiation emitted by solitons in optical fibers. *Physical Review A*, 51:2602–2607, March 1995.

CHAPTER 5

Impact of pump pulse duration on SC generation

Contents

In this chapter we study how the pump pulse duration impacts the SC generation. After describing the motivation of this work, we present a first demonstration of the phenomenon in the nanosecond regime, from a both experimental and numerical point of view. Then we introduce a deeper investigation in the picosecond regime, including a direct comparison between experimental and numerical results.

5.1 Motivation

In the previous chapter, we have introduced the different nonlinear effects leading to SC generation and we have described the particularities of the short-pulse and long-pulse temporal regimes.

In the first case (short-pulse regime, pulse duration < 100 fs typically),

when a PCF is pumped in slightly anomalous dispersion regime, the spectral broadening - mainly driven by SPM and soliton fission - is well understood. Many experimental studies have been conducted by using a femtosecond Ti:sapphire laser, and they could often be corroborated by NLSE-based numerical modeling, which is an effective method when considering such input pulse duration. In particular, the emission of dispersive waves by the fundamental solitons, resulting from a fission process, has been extensively examined.

In the second case (long-pulse regime, pulse duration > 500 fs typically), still considering a pumping in anomalous dispersion regime, the spectral broadening is initiated by MI, giving birth to ultrashort pulses that may interact together and behave as solitons afterwards. The larger the input pulse duration is, the higher the number of ultrashort pulses brought into play is and more complex the SC generation process is. Furthermore, the numerical solving of NLSE for long pulses becomes difficult, especially in the case of the nanosecond regime (high number of samples, high computation time). For that reasons, the long-pulse regime lacks a thorough understanding of the spectral broadening mechanism because of the huge number of radiations propagating together. In particular, to the best of our knowledge, it is unknown what the effect of pump pulse duration is on this mechanism.

To get a new insight in this context, we study hereafter the influence of input pulse duration on SC generation by keeping the peak power at a constant value. Experimental results are supported by numerical simulations based on NLSE so as to identify the phenomenon having the strongest impact on the spectral broadening.

5.2 Impact of pump pulse duration: a first demonstration in the nanosecond regime

The work presented in this section has been realized in the frame of "NextGenPCF" European project, which was dedicated to the design, fabrication and use of PCF for biomedical applications, telecommunications and gas sensing. The SC experiments have been conducted by XLIM in collaboration with Multitel (Belgium) and Leukos (France).

5.2.1 Specifically designed adjustable pump laser source

In order to study the influence of the temporal characteristics of the pump source on SC generation, a versatile all-fibred laser source had been firstly designed and fabricated. For the purpose of this work, the pump laser (with carrier wavelength of 1060 nm) has to be adjustable in terms of pulse duration and repetition rate. We achieved this functionality using Master Oscillator Power Amplifier (MOPA) configuration, as described in fig. 5.1. The MOPA laser, developped by Multitel, can be divided into four blocks. The first block is an adjustable seed source which is then amplified in the next two blocks, referred to as the preamplifier and the booster. The last block is the fibred output.

The seed source is directly modulated by an opto-electronic modulator (OEM), and is composed by a laser diode (Lumics LU1055M200), that is heated to $41\,°C$ to reach the 1060 nm emission wavelength ($0.3\,nm/°C$ spectral shift with temperature). The OEM driver provides one adjustable parameter namely pulse width. The pulse duration can be continuously tuned from ~200 ps to ~2 ns and the repetition rate can be adjusted between 250 kHz and 1 MHz. The upper limit of the repetition rate is imposed by the driving electronics, whereas the lower limit is manually set so as to limit the peak power in the booster.

The preamplifier consists of two stages. The first stage is a single-pass

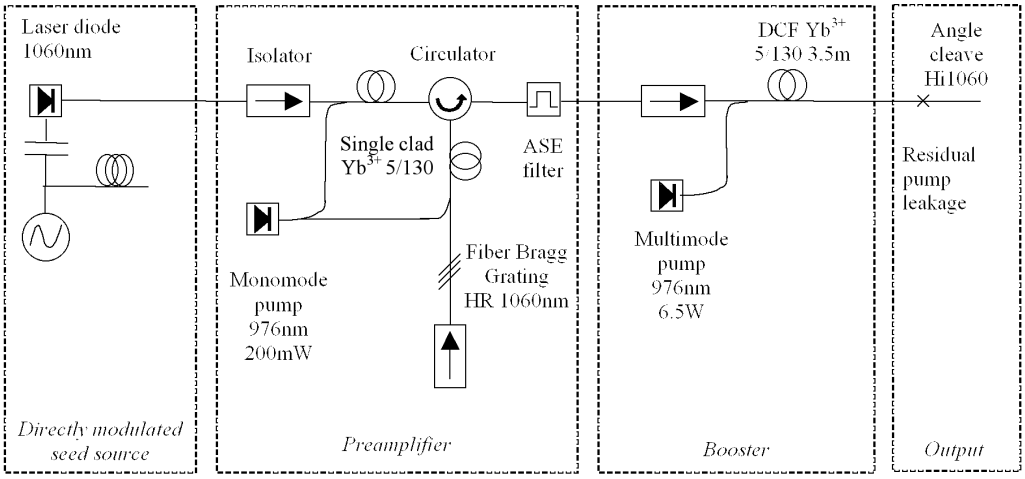

Figure 5.1: Scheme of the MOPA laser.

linear amplifier and the second stage is a round-trip amplifier, both stages being fed using one single monomode pump diode.

The booster is based on a double-clad Yb-doped fibre amplifier pumped by a multimode diode.

The last block is the fibre delivery, composed by HI1060 fibre, which allows to filter out the residual multimode pump power. Fig. 5.2 shows a picture of the complete adjustable laser source.

Figure 5.2: Picture of the complete adjustable laser source.

5.2.2 Experimental setup

The experimental setup used for studying SC generation in the nanosecond regime is presented in fig. 5.3(a). An external pulse generator, which

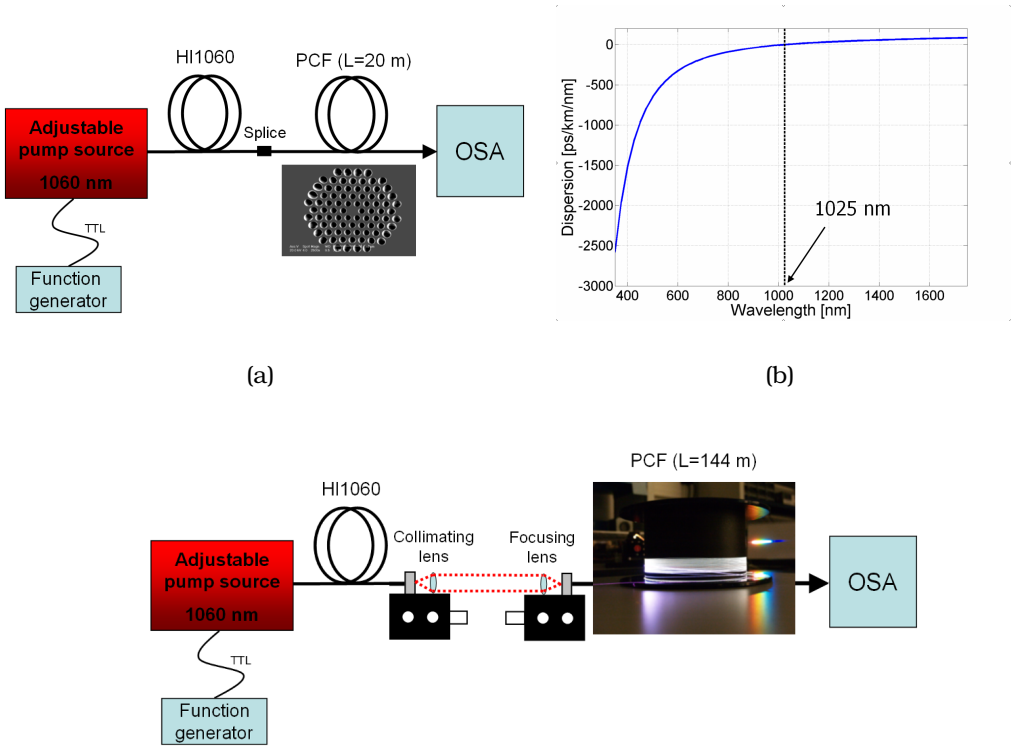

Figure 5.3: (a) Experimental setup used for studying SC generation with 20 m of PCF. (b) Calculated dispersion curve of the PCF used in the experiment. The dashed black line corresponds to the ZDW. (c) Experimental setup used for studying SC generation with 144 m of PCF.

provides a TTL signal, is connected to the seed source so as to set the repetition rate at 500 kHz. By controlling the DC current applied to the OEM driver through a potentiometer placed on the front panel of the laser, we set the pulse duration to 185, 658 ps and 1.16, 1.21, 1.41, 1.51, 1.75, 1.81 ns, measured at FWHM. The HI1060 fibre output beam of the laser source is launched into a nonlinear air-silica PCF, whose hole diameter

and period are 2.5 μm and 4 μm, respectively, the core diameter being 3 μm. The ZDW of the fundamental guided mode is located at 1025 nm (see fig. 5.3(b)), so that the fibre is pumped in the anomalous dispersion region (the pump wavelength is 1060 nm). Finally, the SC at the PCF output is measured by an optical spectrum analyser (350-1750 nm bandwidth, 1 nm resolution).

5.2.3 Experimental results

In a first step, the length of the PCF is fixed to 20 m and the latter is directly spliced with the HI1060 fibre (fig. 5.3(a)). The output spectral broadening is recorded as a function of the input pulse duration, the peak power of the pump laser being maintained to ~400 W. The results obtained are plotted in fig. 5.4. First of all, it is noticeable that the SC extension is contained roughly between the wavelengths of 1000 and 1670 nm. This IR broadening, essentially pointed towards the Stokes side of the pump, is mainly due to MI, SRS and SSFS. Consequently no significant energy is created on the anti-Stokes side of the pump. Furthermore, when the input

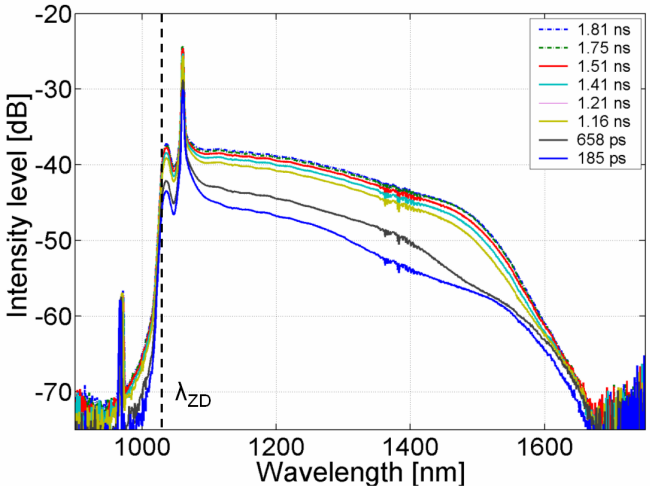

Figure 5.4: Experimental SC spectra generated as a function of pulse duration, with constant peak power of ~400 W.

pulse duration is varied, the SC spectral bandwidth remains roughly the

same. Only the spectral power density is modified, consistently with the variation of the pump average power. As a result, no impact of the pump pulse duration on the spectrum width can be observed on the nonlinear mechanism at this step of the study.

In a second step, the whole PCF coil is used, bringing the fibre length to 144 m. For technical reasons, no more splicing is made between the HI1060 fibre and the PCF. As an alternative, the coupling is operated in free space by using a collimating lens and a focusing lens, as depicted in fig. 5.3(c). Hereafter, we present the SC results achieved for different input pulse durations with three different values of the peak power, P_1 ~200 W, P_2 ~300 W, P_3 ~1 kW (see fig. 5.5). The two peaks present in the output spectra, situated at 976 nm (denoted as "A") and at 1060 nm (denoted as "B"), correspond with the residual CW multimode pump and the pulsed pump, respectively. Moreover, as already noted previously, the SC extends mostly towards the longer IR wavelengths.

For a fixed pulse duration, we observe that the SC spectrum is enlarged when the peak power is increased. For example, considering 185 ps input pulses, the longest wavelength of the spectrum is ~1400 nm, ~1470 nm and ~1750 nm for P_1, P_2 and P_3, respectively. Certainly, this behaviour is fully expected, since SC generation is based on nonlinear effects, as described in the previous chapter.

On the other hand, the evolution of the SC spectrum with the pulse duration, the peak power being constant, is not predictable. The examination of the graphs of fig. 5.5 reveals that, whatever the peak power is, the spectral bandwidth is increasing with the pulse duration. For example, in the case of fig. 5.5(a), the longest SC wavelength varies from ~1400 nm to ~1750 nm when the pulse duration is increased from 185 ps to 1.81 ns.

As a conclusion of this experimental study, it has been demonstrated that, beyond a certain PCF length, the spectral broadening depends on the input pulse duration. This non-obvious phenomenon would suggest that there exists a particular process in SC generation, which is affected by a

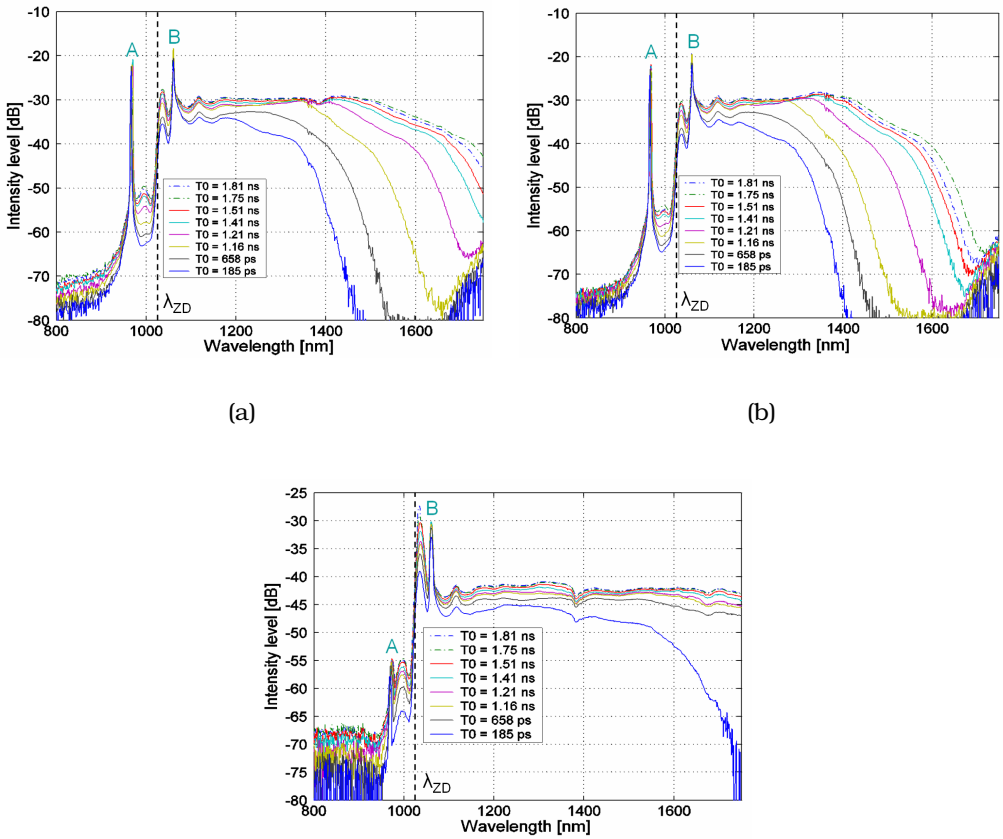

Figure 5.5: Experimental SC spectra generated as a function of pulse duration, with constant peak power (a) P_1 ~200 W, (b) P_2 ~300 W, (c) P_3 ~1 kW.

modification of the pulse duration.

5.2.4 Numerical study and discussion

In order to understand how the input pulse duration can have an impact onto the mechanism of SC build-up, numerical simulations based on solving the full NLSE (including full dispersion coefficient, SPM, Raman effect and fibre loss) using the split step Fourier method are performed. So as to keep reasonable computation time, the study is made in the picosecond regime and, consistently, with a reduced propagation length compared to

the nanosecond case. The input Gaussian pulse duration is fixed to 6, 8, 10, 13 and 15 ps (measured at FWHM) alternately. The PCF length and the input peak power are fixed to 14.4 m and 300 W respectively. Figure

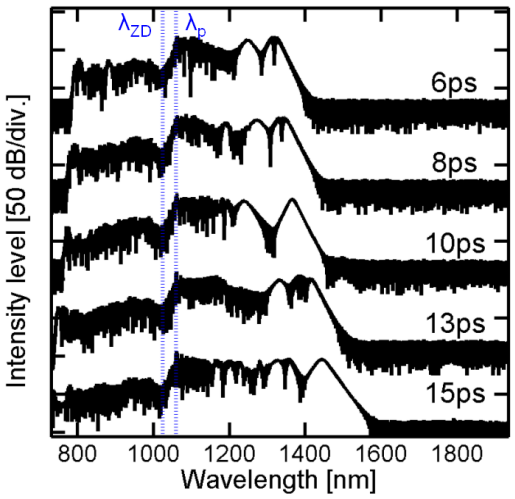

Figure 5.6: Numerical SC spectra for different input pulse durations and constant peak power of 300 W after a propagation distance of 14.4 m. The dashed line represents the ZDW.

5.6 shows the calculated SC spectra for the different values of pulse duration and at constant peak power. We can observe the progressive growing of the spectral IR bandwidth upon pulse duration: the longest SC wavelength varies from ∼1400 nm to ∼1600 nm when the pulse duration is increased from 6 ps to 15 ps. This displays the same tendency as for the experimental results. To determine which effect among dispersion and nonlinearity is predominant on the pulse propagation, the characteristic lengths L_D and L_{NL} are estimated. Using equation 4.10 with T_0=6 ps (L_D is minimum in this case) and β_2=-5.097e-27 s^2/m, it comes L_D ∼7 km. As well, equation 4.10 with $\gamma = 0.01521/W/m$, gives L_{NL} ∼22 cm for a peak power of 300 W. It means that the nonlinear effects affect the pulse propagation since the first centimetres of the fibre. As a matter of fact, when an intense optical pulse is injected into an optical fibre in the anomalous dispersion regime, the lowest threshold nonlinear effect is MI. The latter leads to the break-up of the initial pulse into a periodic train of ultrashort

pulses that may be considered as solitons. Afterwards Raman effect acts as a perturbation that breaks the symmetry of the soliton train and hence most of the energy takes the form of individual solitons shifting towards lower frequencies via SSFS. Since SSFS is proportional to the square of the soliton power, a soliton which is initially generated in the central part of the input pulse downshifts faster than the neighbouring solitons. Besides, because of the dispersion-induced slowing down, this central soliton may collide with other solitons of the train [1]. Another important consequence of Raman gain is that during each collision, the slower, lower-frequency central soliton acquires energy from a higher-frequency soliton while reducing its time width down to the femtosecond range, so as to keep the shape of a fundamental soliton [2]. As a result of all collisions, the most energetic solitons run away from the initial soliton train and a broad SC is thus generated. For better visualising the whole nonlinear mechanism, we have plotted in fig. 5.7 the temporal evolution of the input pulse along the fibre, in the case T_0=6 ps. In inset can be seen how MI breaks the initial temporal pulse profile and how the soliton train appears at the end of the fibre. To sum up, the collision-enhancement of the most energetic soliton down-shift rate is crucial for understanding the mechanism of SC generation in optical fibres. It is highlighted that the phenomenon cannot be explained in term of SSFS alone.

5.3 Deeper investigation in the picosecond regime

The experimental work presented in this section (laser development and SC experiments) has been carried out by Multitel in partnership with XLIM and Leukos.

5.3.1 Pump laser source

A simplified scheme, showing the composition of the laser used in this experiments, is presented in fig. 5.8. An oscillator, emitting 200 fs pulses

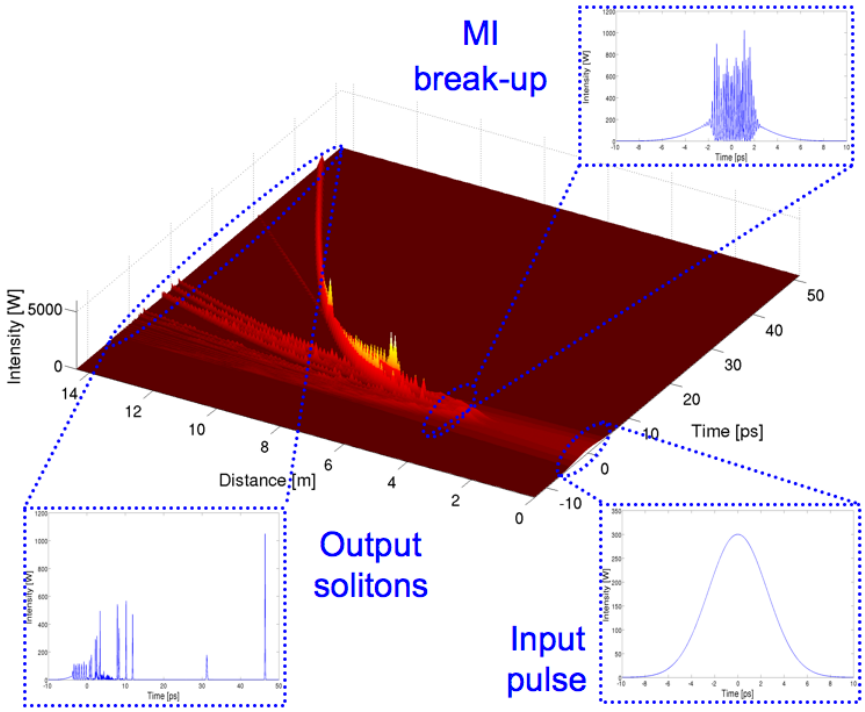

Figure 5.7: Numerical temporal evolution of the input pulse as a function of propagation distance for the case where $T_0 = 6\,ps$. Inset: temporal profile at different position along the fibre

Figure 5.8: Scheme of operating principle of the laser source.

at 1030 nm and 30 MHz, is directly connected with a stretcher, which raises the pulse duration up to 300 ps. The pulses are stretched to lower the peak power, because too high peak power could cause optical damage in the amplifier. Then, the stretched pulses pass through a pulse picker based on a Pockels cell, which reduces the repetition rate to 300 kHz. They are afterwards directed to Yb:KGW amplifier and finally to a compressor, composed by a diffraction grating mounted on a motorized translational

stage. This compressor allows to tune the pulse duration from 500 fs to 10 ps.

Thereby a (sub)picosecond pump laser source operating at 1030 nm with adjustable pulse duration is obtained. The peak power can be changed between 3 and 15 kW.

5.3.2 Experimental setup and results

In fig. 5.9(a) is represented the experimental setup used for collecting SC spectra for different pulse durations and fixed peak power. The output beam of the laser passes through a half-wave plate ($\lambda/2$) and a polarizing beam splitter (PBS), which allows to direct a part of the signal to an autocorrelator. This autocorrelator is used to measure the pulse duration before the injection into the PCF. A second pair of half-wave plate and PBS is employed to control the incident power. The beam is then coupled to a HI1060 singlemode fibre 99/01 splitter. The 1% output of the splitter is used for monitoring the power injected into the HI1060 fibre by means of a power meter (PWM). The 99% output is spliced to a PCF, the splice loss being about 2 dB. The PCF is 8 m long and is characterized by a 5 μm core diameter, a 3 μm hole-to-hole pitch and a 1.5 μm hole diameter. Its ZDW is located at 974 nm (see fig. 5.9(b)), the 1030 nm pumping being thus operated in the anomalous dispersion regime. Finally, an optical spectrum analyser (OSA, 350-1750 nm bandwidth, 1 nm resolution) and a PWM are used to measure the spectral power density, as a function of the wavelength, at the ouput of the PCF.

It is important to note that all the values of pulse duration (and corresponding peak power) are measured at the output of the laser, before the injection into the fibre splitter. Therefore these values are different from the ones that would be obtained at the PCF input, because of nonlinear effects in the short piece of HI1060 fibre in one hand and splice loss on the other hand. The expected impact of nonlinear effects is not negligible

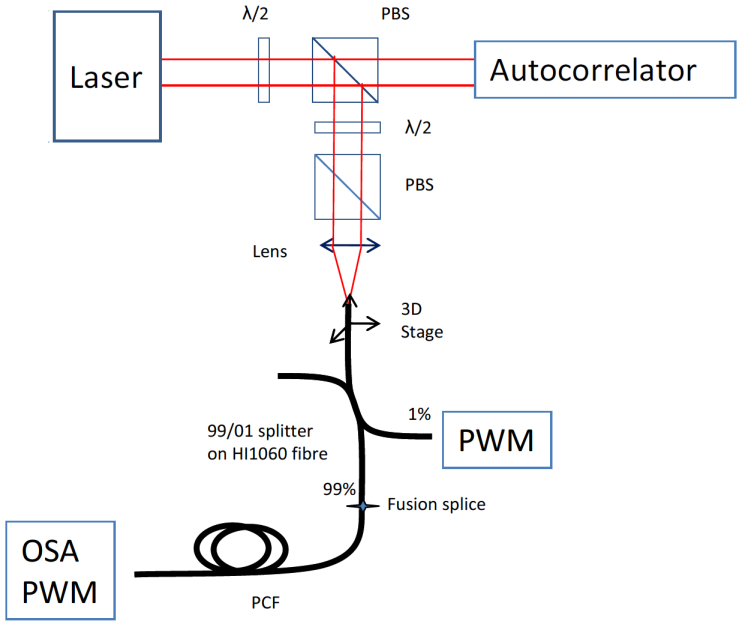

(a)

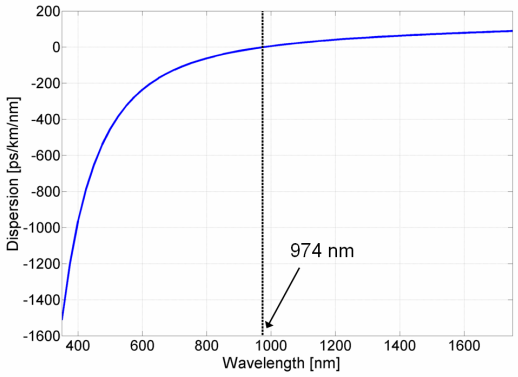

(b)

Figure 5.9: (a) Experimental setup used for the SC generation in sub-picosecond regime. (b) Calculated dispersion curve of the PCF used in the experiment. The dashed black line corresponds to the ZDW.

indeed, since the fibre length (40 cm from the splitter input to the 99% output) is distinctly superior to the nonlinear length ($\sim$1 cm for 15 kW peak power). The most likely nonlinear phenomena are SPM and SRS, given that pulses propagate in normal dispersion regime. Moreover, the

expected effect of HI1060 fibre dispersion on pulse duration is not negligible (80 fs stretching for 500 fs input pulse duration, without taking nonlinear effects into account).

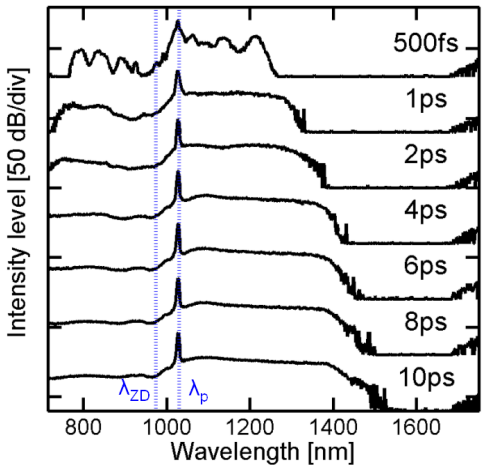

Figure 5.10: Experimental output SC spectra for different input pulse durations and constant input peak power after the propagation in 8 m pf PCF.

In fig. 5.10 we show the SC spectra obtained for pulse duration of 500 fs, 1, 2, 4, 6, 8 and 10 ps , the peak power being fixed to 3 kW. As pointed out in the nanosecond regime, the spectral broadening is enlarged with respect to the pulse duration. The main difference here is that, due to the higher incident peak power, some energy is generated on the anti-Stokes side of the pump. In the case of 10 ps pulses, the output spectrum extends roughly from 650 to 1500 nm. It is also clear that the spectral broadening tends to saturate when the pulse duration exceeds $\sim$6 ps. Furthermore, the input pulse duration visibly affects the shape and the smoothness of the spectrum, which appears to be more perturbed for short pulses.

5.3.3 Comparison with numerical results

The same numerical method as previously, based on the full NLSE, is employed to simulate the pulse propagation in the PCF. Here, the actual value of the input pulse duration (i.e., the one used in the experiment) can be

used, contrary to the nanosecond case. So we consider Gaussian pulses with duration of 500 fs, 1, 2, 4, 6, 8 and 10 ps. The peak power is fixed to 140 W and the fibre length is 18 m. The SC spectra obtained are plotted in fig. 5.11. To facilitate the comparison with experimental results, each spectrum results from an average calculated over ten different noise seeds. The first noticeable point is that the Stokes bandwidth increases with respect to the input pulse duration, with an excellent agreement with the experimental results. Additionally the agreement between simulation and experiment relates to the smoothness of the SC spectra, which is enhanced when the pulse duration is enlarged. Again, the characteristic lengths L_D

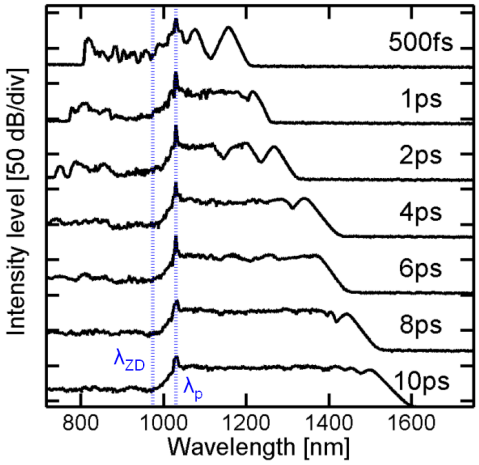

Figure 5.11: Numerical SC spectra for different input pulse durations (from 500 fs to 10 ps) and constant peak power of 140 W after a propagation distance of 18 m. The dashed line represents the ZDW.

and L_{NL} show the predominant role played by the nonlinear effects during the propagation: L_D is minimum for T_0=500 fs and is ∼34 m, whereas L_{NL} ∼15 cm for 140 W peak power, considering $\beta_2 = -7.234\,e^{-27}\,s^2/m$ and $\gamma = 0.04581/W/m$. Once more, the lowest threshold nonlinear effect is MI, with subsequent creation of a train of fundamental solitons. Next Raman gain acts as a perturbation that breaks the symmetry of the soliton train, and individual solitons undergo SSFS towards lower frequencies. The whole nonlinear mechanism is exhibited in fig. 5.12(a) in the case of a

2 ps pulse duration. Soliton collisions are the enhancement factor of SSFS, bringing additional energy to the slower soliton (see fig. 5.12(b)). At the

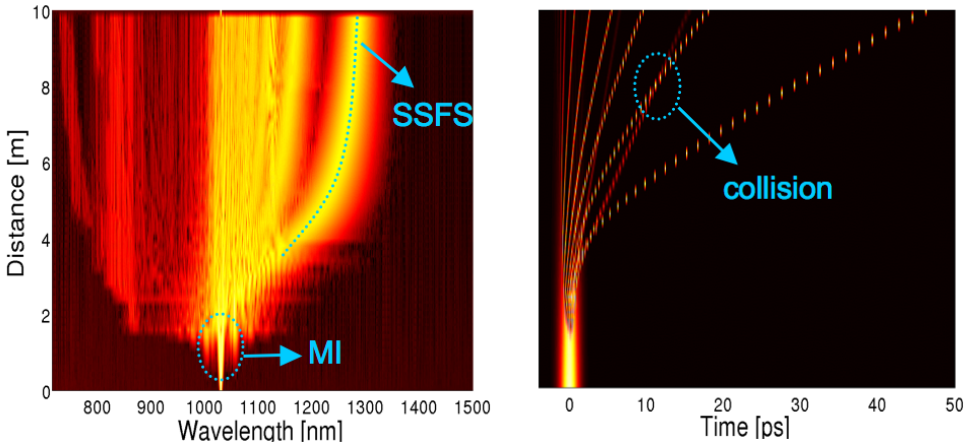

(a) (b)

Figure 5.12: Numerical spectral (a) and temporal (b) evolution over the distance of propagation for an input pulse with $T_0 = 2\,ps$. In evidence the effect of MI, the spectral trajectory of the most red-shifted soliton due to SSFS, and a temporal soliton collision.

output of the fibre, whatever the pulse duration, the Stokes bound of the spectral broadening coincides with the spectral position of the most energetic fundamental soliton generated initially from the central part of the input pulse. This statement is clearly confirmed by the spectro-temporal representation of fig. 5.13, which also shows the matching between the temporal position of all solitons with the different spectral peaks. Finally, it is obvious in fig. 5.14 that the number of solitons is increasing with the input pulse duration, and accordingly the IR spectrum becomes smoother (fig. 5.11).

5.3.4 Conclusion

In this chapter, we have introduced a new insight of the nonlinear mechanism which resides behind long-pulse SC generation in PCF. In the case of nanosecond and picosecond regimes, we have pointed out the impact

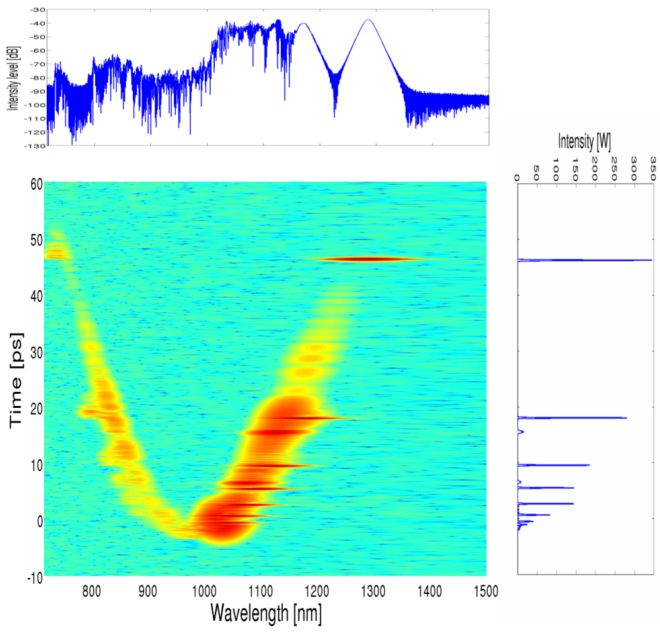

Figure 5.13: Calculated spectrogram at $z = 18\,m$ for a pulse with duration of 2 ps. The spectrogram is calculated following the procedure expressed in Ref. [3].

of input pulse duration on the spectral broadening, both numerically and experimentally. Beyond the key involvement of MI and SSFS, the effect of multiple soliton collisions has been highlighted, the longest IR wavelength being raised by the most energetic soliton, which is initially created in the central part of the input pulse. Basically, the number of solitons produced by MI explains why a longer input pulse leads to a larger IR bandwidth at the output: more solitons means more collisions, so more possibilities to exacerbate the SSFS of the most energetic soliton. Additionally, this increase of the spectral bandwidth comes with an enhancement of the spectrum flatness, due to the higher number of radiations generated.

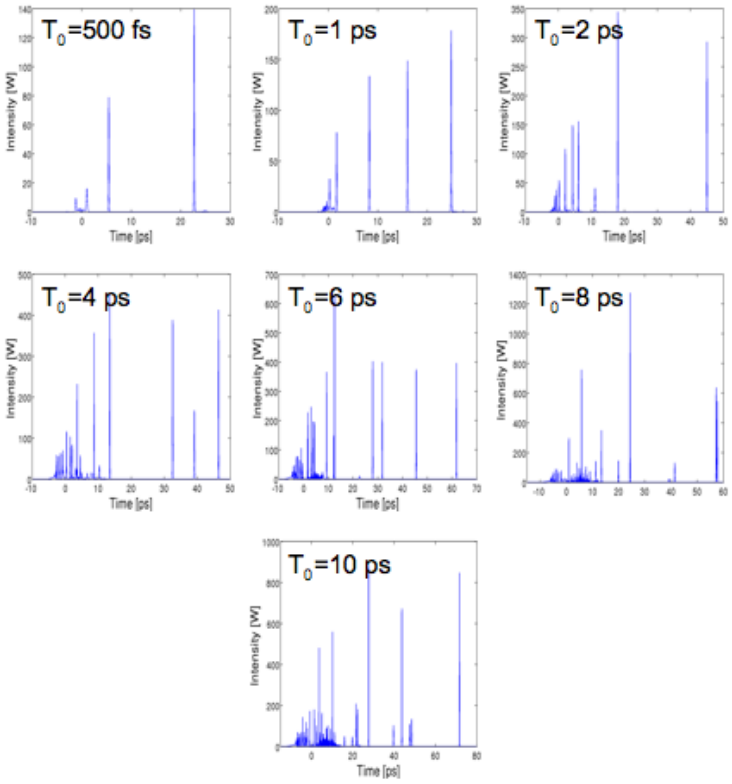

Figure 5.14: Numerical temporal profile at $z = 18\,m$ for different input duration.

Bibliography

[1] M.N. Islam, G. Sucha, I. Bar-Joseph, M. Wegener, J.P. Gordon, and D.S. Chemla. Femtosecond distributed soliton spectrum in fibers. *Journal of the Optical Society of America B*, 6:1149, June 1989.

[2] M.H. Frosz, O. Bang, and A. Bjarklev. Soliton collision and raman gain regimes in continuous-wave pumped supercontinuum generation. *Optics Express*, 14:9391, 2006.

[3] J.M. Dudley and S. Coen. Supercontinuum generation in photonic crystal fiber. *Reviews of Modern Physics*, 78(4):1135–1184, October 2006.

CHAPTER 6

Control of soliton collision-induced enhancement of SC bandwidth

Contents

In this chapter we develop a simplified analytical model that describes how the infrared (IR) tail of the SC is generated. In particular we focus on the mechanisms responsible for the enhancement of SC bandwidth. This chapter is organized as follow: first we introduce the context of this work, then we present some slight modifications to well known models for Raman SSFS and collisions, so to make them closer to our experimental conditions. Finally a comparison between analytical model, numerical solution of the full NLSE and experimental results is presented.

6.1 Introduction

In Chapter 5, some of the physical mechanisms driving SC generation in the IR have been discussed. For long pump pulse propagating in the regime of anomalous dispersion, the nonlinear effect that initiates SC generation is MI. In the first stage of propagation, MI acts to break up the

pump pulse into a periodic train of short pulses, which can be approximated as first-order solitons. Assuming that the MI period, which we denote as T_{MI}, is much shorter than the input pulse duration T_0, the number of solitons can be roughly evaluated as

$$N_{sol} = \frac{T_0}{T_{MI}} = \pi T_0 \sqrt{\frac{2|\beta_2|}{\gamma P_0}}, \tag{6.1}$$

where P_0 is the peak power of the input pulse, γ is the nonlinear coefficient, and β_2 is the second-order dispersion coefficient. Subsequently, as the solitons are further propagating in the fiber, the SSFS induced by Raman scattering acts to break the periodicity of the soliton train. More specifically, the rate of SSFS being proportional to the fourth power of the inverse soliton duration [1], the most-powerful soliton which is initially located in the central part of the soliton train, down-shifts in frequency and decelerates in time faster than the neighbouring solitons. Therefore, that soliton will successively collide with the other solitons delayed in the trailing of the soliton train. Thus, it is gradually amplified throughout collisions in the presence of Raman scattering, since the soliton acquires energy from higher-frequency solitons. Thereby, the soliton frequency is increasingly down-shifting. Because the number of collisions can be very high at the large values of T_0, the soliton can become extremely powerful, thus dramatically emerging from the rest of the soliton background. Hence, it is sometimes referred to as the *giant* soliton or *rogue* soliton, although the question is still being debated whether the latter term is appropriate [2]. Note that the giant soliton never collides with the solitons of the leading edge and therefore, the maximum number of collisions endured by the giant soliton is only half the number of solitons in the train, i.e. $N_{coll} = N_{sol}/2$.

As the result of all collisions in the presence of Raman scattering, the giant soliton is the most shifting from its initial position (both temporally and spectrally) and therefore plays a major role in determining the exten-

sion of the SC spectrum towards the IR. As pointed out in the previous chapter, the collision-enhancement of soliton down-shift rate is crucial for understanding the mechanism of SC generation in an optical fibre.

6.2 Simplified analytical model

The SC spectrum in the anomalous region consists of both an ensemble of solitons of various amplitudes and a dispersive background. In our simplified model, we neglect the dispersive background by assuming that the SC spectrum only consists of solitons, each individual soliton being determined by the three following parameters, namely the peak power (or equivalently time width), the carrier frequency and the temporal position. Under this assumption, the physical system reduces to a finite number of degrees of freedom and is therefore considerably simplified. Hence, we suppose that solitons of different peak powers are moving at different velocities in the time-frequency space under the effect of SSFS. When the temporal positions of two solitons coincide, we assumed that a collision takes place and the two solitons can potentially exchange some energy via the Raman gain. Note that the soliton collision is assumed to be of negligible length. Additionally, we suppose that only pairs of solitons are colliding since collisions between three or more solitons are much less probable. Note that it is reasonable to assume that interaction of the solitons with dispersive waves in the visible has negligeable impact on soliton propagation in the IR. As a further simplification, stable propagation of higher-order solitons is prohibited because of the presence of Raman perturbation and therefore solitons are assumed to be of the first order. Nevertheless, we supposed that the Raman perturbation is not too large so that a soliton keeps the shape of a hyperbolic secant after collision.

In practice, the length of fiber is discretized into many steps on which we numerically integrate the fundamental parameters of each soliton. That yields the trajectory of each soliton in the time-frequency space. Whenever

a collision occurs between two solitons, i.e. the provided time positions coincide, the relative Raman gain is calculated and the peak powers of the two interacting solitons are updated accordingly. Because solitons after a collision tend to reshape adiabatically in order to recover the more stable form of first-order solitons [3], we assume that the time width is resized according to the soliton condition

$$\frac{\tau_s^2}{|\beta_2|} = \frac{1}{\gamma P_s}, \tag{6.2}$$

where τ_s and P_s are the time width and peak power of the soliton, respectively. Therefore, for the given peak power, we modify the time width to fit again a soliton solution of the same energy. Subsequently, the updated peak power and time width are used as initial conditions for the next stage of calculation of the trajectories until the next collision takes place or until integration is finished over the entire fibre length.

Note that in our model the wavelength-dependence of the dispersion and nonlinear coefficients are included.

Thus, we can investigate how the evolution of the peak power impacts the soliton down-shifting in frequency and deceleration in time domain in the anomalous dispersion regime. In doing so, it is possible to obtain a set of trajectories in the time-frequency space, i.e. one per individual soliton. In particular, we focus our attention to the giant soliton which is most red-shifted and therefore represents the upper wavelength limit of the SC spectrum. Note that the giant soliton is formed by acquiring energy from other solitons whereas the total number of individual solitons remains constant throughout propagation in our model.

In Fig. 6.1(b), we have represented the flow-chart of the algorithm implemented for solving the soliton trajectories. Besides, we have shown an example of three temporal trajectories. After each collision, the Raman-amplified soliton will experience a larger frequency shift per unit of propagation length whereas the soliton which is depleted will undergo a smaller

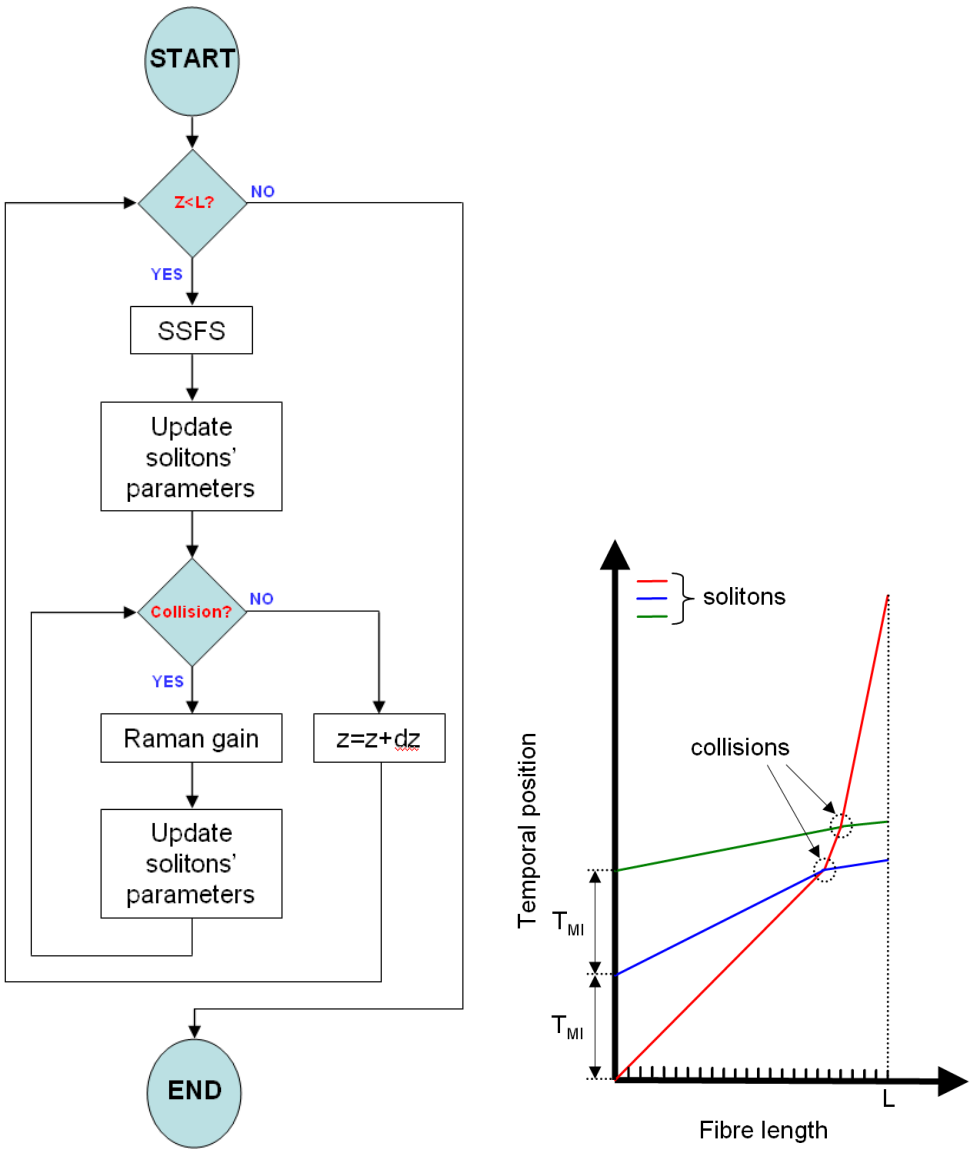

(a) (b)

Figure 6.1: (a) Block diagram representing how our model works. (b) Example of temporal trajectories of three solitons.

rate of frequency shift. This is clearly visible from the changes of the slopes in the trajectories of the colliding solitons. Hence, Raman gain and SSFS are the key ingredients of our simplified model to describe soliton dynamics which governs the extension of SC towards the IR. In the next

subsections, the detailed procedures for evaluating both the Raman gain and the rate of SSFS are described.

6.2.1 Raman gain in soliton collision

To evaluate the amount of Raman gain that is experienced during collisions between solitons, we have used a theoretical approach inspired by that of Islam in Ref. [4]. Nevertheless, we have refined this basic procedure in order to reproduce some essential features observed in the experiments of chapter 5. Hence, in some extreme cases, the time width of solitons can become so short that it is comparable or even inferior to the period of molecular oscillations, that is about 75 fs in silica glass. In other situations, the two colliding solitons may have a frequency detuning exceeding that of the Raman-gain peak. In both situations, one has to take account of the finite bandwidth of the Raman gain, that was unfortunately neglected in Ref [4] thereby leading to overestimate the Raman gain. When accounting for the finite bandwidth of the Raman gain, the amount of Raman gain experienced during the collision is moderated and subsequently the amplification of the giant soliton is restrained. Another simplification in Ref. [4] that artificially maximize the Raman gain is the approximation that the pump soliton is not depleted, leading to unrealistic prediction of the Raman gain when the number of collisions is high. In our approach, the depletion of the higher-frequency colliding soliton is taken into account.

Here, the Raman effect is treated as a perturbation of first-order solitons, for which dispersion and nonlinearity are already balanced. In soliton units, this perturbation will read as:

$$\frac{\partial A}{\partial z} \backsimeq \imath A \int_{-\infty}^{+\infty} f(s)|A(t-s)|^2 ds, \tag{6.3}$$

we write $A(t)$ as $A = A_1 + A_2 e^{\imath\Omega t}$ and we substitute it into eq. 6.3:

$$\begin{aligned}
&\frac{\partial A_1}{\partial z} + e^{\imath\,\Omega\,t}\,\frac{\partial A_2}{\partial z} \simeq \imath\,(A_1 + A_2\,e^{\imath\,\Omega\,t}) \\
&\times \int_{-\infty}^{+\infty} f(s)\{|A_1(t-s)|^2 + |A_2(t-s)|^2 + A_1(t-s)\,A_2^*(t-s)e^{-\imath\,\Omega\,(t-s)} + \\
&+ A_2(t-s)\,e^{\imath\,\Omega\,(t-s)}A_1^*(t-s)\}ds
\end{aligned} \tag{6.4}$$

where $A_1(t)$ and $A_2(t)$ are the complex amplitudes associated with the two interacting first-order solitons separated by a frequency detuning Ω. For clarity, we assume that $A_2(t)$ is pumping $A_1(t)$. If we neglect the effect of dispersion and phases on soliton interaction, and if we focus only on $A_1(t)$, we can write (same procedure for $A_2(t)$):

$$\begin{aligned}
\frac{\partial A_1}{\partial z} &= \imath\,A_1 \int_{-\infty}^{+\infty} f(s)\{|A_1(t-s)|^2 + |A_2(t-s)|^2\}ds + \\
&+ \imath\,A_2 \int_{-\infty}^{+\infty} f(s)\{A_1(t-s)\,A_2^*(t-s)\,e^{\imath\Omega s}\}ds
\end{aligned} \tag{6.5}$$

We exploit the property $\frac{\partial |A_1|^2}{\partial z} = A_1^*\frac{\partial A_1}{\partial z} + A_1\frac{\partial A_1^*}{\partial z}$ so that:

$$\begin{aligned}
\frac{\partial |A_1|^2}{\partial z} &= \imath A_1^*\,A_2 \int_{-\infty}^{+\infty} f(s)\{A_1(t-s)\,A_2^*(t-s)\,e^{\imath\,\Omega\,s}\}ds + \\
&- \imath\,A_1\,A_2^* \int_{-\infty}^{+\infty} f(s)\{A_1^*(t-s)\,A_2(t-s)\,e^{-\imath\,\Omega\,s}\}ds = \\
&= -\Im\{2A_1A_2^* \int_{-\infty}^{+\infty} R(t)A_1(t-s)A_2^*(t-s)e^{-\imath\Omega s}\}.
\end{aligned} \tag{6.6}$$

In case the soliton temporal duration is much longer than the typical period of the molecular oscillation included in the Raman response $f(s)$ (generally for $\tau_s \geq 100fs$), the integral of eq. 6.6 can be simplified by assuming that the two field envelopes are constant. In doing so the integral becomes proportional to the Fourier transform of $F(\Omega) = \mathcal{F}\,(f(s))$. Now the limitation of the procedure presented in Ref. [4] is in the assumption that $F(\Omega) \backsimeq \Omega t_d$, with $t_d = T_d\tau_s$ is the slope of the Raman gain, $T_d \backsimeq 6fs$ is sometimes called the relaxation time of the Raman response. In fact, if the collision implies a weak energy exchange, one can find that the gain factor

in power for $|A_1|^2$ is e^{4t_d} per collision and otherwise for $|A_2|^2$ is e^{-4t_d} . In these conditions the gain factor does not depend on the frequency detuning Ω, because it is balanced by the difference in group delays which make the collision faster and hence less effective. When the number of collision is large, however this assumption leads to an overestimation of the Raman gain. To avoid this problem, we introduce a projection coefficient Q as to estimate the inner integral in eq. 6.6 as $QA_1(t)A_2^*(t)$.

$$Q\int_{-\infty}^{+\infty}|A_1(t)|^2|A_2(t)|^2dt=\int_{-\infty}^{+\infty}A_1^*(t)A_2(t)\left[\int_{-\infty}^{+\infty}f(s)A_1(t-s)A_2^*(t-s)e^{-\imath\Omega s}ds\right]dt. \tag{6.7}$$

Note that in the assumption of Ref. [4], where $A_1(t)$ and $A_2(t)$ are long pulses ($\geq$100 fs), our definition of Q converges to the coefficient Ωt_d.
The power exchange between the colliding solitons, can be written as:

$$\begin{cases}\dfrac{\partial|A_1|^2}{\partial z}=2Q|A_1|^2|A_2|^2\\[2ex]\dfrac{\partial|A_2|^2}{\partial z}=-2Q|A_1|^2|A_2|^2.\end{cases} \tag{6.8}$$

To simplify the calculation of the power exchange and the projection coefficient Q, we use a Gaussian fit of the solitons involved in the collision. The soliton solutions for $|u_1(t)|^2$ and $|u_2(t)|^2$ are:

$$|u_1(t)|^2=P_1(z)sech^2\left(\frac{t}{\tau_1}\right)\ \ and\ \ |u_2(t)|^2=P_2(z)sech^2\left(\frac{t}{\tau_2}\right) \tag{6.9}$$

whereas the Gaussian fit reads as:

$$|u_1(t)|^2=P_1(z)e^{-\frac{t^2}{a_1^2}},,and\ \ |u_2(t)|^2=P_2(z)e^{-\frac{t^2}{a_2^2}}, \tag{6.10}$$

where a_1 and a_2 are chosen so that pulses under gaussian approximation have the same peak power and the same energy of the original solitons. Therefore $a_1=2\tau_1/\sqrt{\pi}$ and $a_2=2\tau_2/\sqrt{\pi}$. Now, if we substitute eq. 6.10 in

eq. 6.7 we obtain:

$$Q = \int_{-\infty}^{+\infty} f(s) e^{-\frac{1}{4}\left(\frac{1}{a_1^2}+\frac{1}{a_2^2}\right)s^2} e^{-\imath\Omega s} ds. \tag{6.11}$$

The advantage under this approximation, is that the coefficient Q does not depend on z and can be calculated one single time per collision. If we use the new expression of Q into the system of eq. 6.8 and if we take the time average so to reduce to single coordinate z, we obtain:

$$\begin{cases} \dfrac{\partial P_1}{\partial z} = 2P_1P_2 \dfrac{a_2}{\sqrt{a_1^2+a_2^2}} e^{-\frac{\Omega^2 z^2}{a_1^2+a_2^2}} \\ \\ \dfrac{\partial P_2}{\partial z} = -2P_1P_2 \dfrac{a_1}{\sqrt{a_1^2+a_2^2}} e^{-\frac{\Omega^2 z^2}{a_1^2+a_2^2}} \end{cases} \tag{6.12}$$

Note that here we conserve the energy $E = P_1(z)a_1 + P_2(z)a_2$ because we have assumed that during the collision the gamma coefficient is constant in frequency. Since the solution of eq. 6.12 is known in closed form for the whole real axis z, we match the asymptotic solution at $z = -\infty$ with the parameters of the two pulses before collision, while we get the values after the collision at $z = +\infty$, being the center of the collision in $z = 0$. With this consideration, we can write the solution as a function of the input parameters:

$$P_{1,OUT} = \frac{C_1 a_2 e^{\psi}}{\kappa + a_1 e^{\psi}}, \quad P_{2,OUT} = C_1 - \frac{C_1 a_1 e^{\psi}}{\kappa + a_1 e^{\psi}}, \tag{6.13}$$

where

$$\psi = \frac{a_2\sqrt{\pi}QC_1}{\Omega}, \;\; C_1 = P_{2,IN} + P_{1,IN}\frac{a_1}{a_2}, \;\; \kappa = \frac{C_1}{P_{1,IN}} a_2 e^{-\psi} - a_1 e^{-\psi}. \tag{6.14}$$

At this point, our assumption is in good agreement with the exponential results in Ref. [4] in the limit of weak conversion and long pulses ($Q \backsimeq \Omega t_d$ and $P_{1,IN} \ll P2, IN$). We study the power gain under various

pulse durations in the case of a single collision between two solitons of the same pulsewidth. In fig. 6.2 we assume that a reduction in temporal

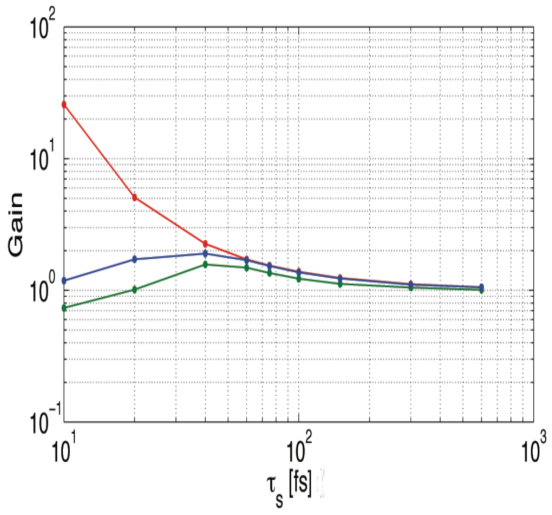

Figure 6.2: Red curve: analytical prediction of gain enhancement under linear approximation of Ref. [4]. Blue curve: analytical prediction following eq. 6.13. Green curve: results from full numerical solution of the NLSE obtained neglecting high order dispersion effects (constant dispersion).

pulsewidth corresponds to an increase in the frequency separation, as to avoid large spectral overlap for the two solitons. We observe a difference in gain between the results presented by Islam and our calculation for solitons shorter than 75 fs, which is a range of pulse duration potentially reachable in experiments and numerical simulations. When reducing the pulse duration the gain predicted from eq. 6.13 becomes smaller in a way similar to the results of the full numerical solution of NLSE. Our results shows that we have extended the validity of the approximated approach to a wider range of pulse durations.

6.2.2 Raman SSFS

Here we present the procedure used to evaluate the SSFS in our model. For this purpose, we have used the generalized form of the procedure explained in Ref. [1]. Indeed in our case we need an expression which

remains valid even in the case of pulses with duration shorter than the typical molecular period of silica response. Differently from the case of collisions, SSFS affects the whole propagation dynamics. Hence we need to consider the combined action of dispersion and Raman susceptibility. The modified NLSE including Raman effect reads in soliton units:

$$-\imath\frac{\partial A}{\partial z} = \frac{1}{2}\frac{\partial^2 A}{\partial t^2} + A(t)\int_{-\infty}^{+\infty} f(s)|A(t-s)|^2 ds \tag{6.15}$$

Now we define the soliton in time and frequency domain (through Fourier transform) in normalized units:

$$A(t) = sech(t)e^{\imath\frac{z}{2}} \xrightarrow{\mathcal{F}} \tilde{A}(\Omega) = \frac{1}{2}sech(\pi\frac{\Omega}{2}) \tag{6.16}$$

with $\Omega = (\omega - \omega_0)\tau_s$ in normalized form as expressed in eq. 4.27, τ_s the soliton time width, $f(-|s|) = 0$ and $\int_{-\infty}^{+\infty} f(s)ds = 1$. It is convenient to write eq. 6.15 in frequency domain through Fourier transform:

$$-\imath\frac{\partial\tilde{A}(\Omega)}{\partial z} = -\frac{1}{2}\Omega^2\,\tilde{A}(\Omega) + \int_{-\infty}^{+\infty}\chi(\Omega'')\tilde{A}(\Omega-\Omega'')d\Omega''\int_{-\infty}^{+\infty}\tilde{A}^*(\Omega')\tilde{A}(\Omega'+\Omega'')d\Omega' \tag{6.17}$$

where

$$\chi(\Omega) = \int_{-\infty}^{+\infty} f(s)e^{\imath\Omega s}ds \quad and \quad \chi(\Omega) = \chi'(\Omega) + \imath\chi''(\Omega) \tag{6.18}$$

Under our choice of normalization $\chi(0) = 1$. We associate the imaginary part of χ with the Raman attenuation coefficient α_R by considering the following pump-signal configuration:

$$A(t) = A_p e^{-\imath\Omega_p t} + A_s(t) \xrightarrow{\mathcal{F}} \tilde{A}(\Omega) = A_p\,\delta(\Omega-\Omega_p) + \tilde{A}_s(\Omega) \tag{6.19}$$

Substituting the latter expression in the eq. 6.17 and considering the terms proportional to the pump power, we have:

$$\frac{\partial}{\partial z}|\tilde{A}_s(\Omega)|^2 = -2\chi''(\Omega-\Omega_p)|A_p|^2|\tilde{A}_s|^2, \quad \Omega \neq \Omega_p, \tag{6.20}$$

where $\alpha_R(\Omega) = 2\chi''(\Omega)$. Since we take into account the soliton mean frequency, and assuming the effect of χ'' as a small perturbation of the soliton defined in eq. 6.16, we obtain:

$$\langle\Omega\rangle = \pi \int_{-\infty}^{+\infty} \Omega \, |\tilde{A}(\Omega)|^2 d\Omega. \tag{6.21}$$

Combining eq. 6.17 and eq. 6.21 we can write:

$$\frac{\partial\langle\Omega\rangle}{\partial z} = -\pi \int_{-\infty}^{+\infty} \alpha_R(\Omega'')d\Omega'' \int_{-\infty}^{+\infty} \tilde{A}^*(\Omega)\,\tilde{A}(\Omega'')d\Omega \int_{-\infty}^{+\infty} \tilde{A}^*(\Omega')\,\tilde{A}(\Omega'+\Omega'')d\Omega'. \tag{6.22}$$

At this point, we know that a change in the mean frequency of the soliton is equivalent to a change in ω_0. By using the formula $\int_{-\infty}^{+\infty} sech(x+\frac{a}{2})sech(x-\frac{a}{2})dx = \frac{2\,a}{sinh(a)}$ we can write:

$$\frac{\partial\omega_0}{\partial z} = -\frac{\pi}{8} \int_{-\infty}^{+\infty} \Omega^3 \frac{\alpha_R(\Omega)}{sinh^2(\frac{\pi}{2}\Omega)} d\Omega \tag{6.23}$$

Here we have done the implicit assumption that the bandwidth of signal A_s is large enough to cover a part of the Raman loss spectrum R (normalized to the value of 0.492 which is the peak value of $\alpha_R(\Omega)$), which leads to:

$$\alpha_R(\Omega) = R\left(\frac{\Omega}{2\pi t_c}\right), \tag{6.24}$$

Now if we come back to physical units the self induced frequency shift reads as:

$$\frac{\partial\nu_0}{\partial z} = -\frac{10^5\lambda^2 D(\lambda)}{16\pi c\tau_s^3} \int_{-\infty}^{+\infty} \Omega^3 \frac{R(\frac{\Omega}{2\pi\tau_s})}{sinh^2(\frac{\pi\Omega}{2})} d\Omega \qquad \left[\frac{THz}{km}\right] \tag{6.25}$$

using λ, $D(lambda)$, c and τ_s in units of cm and ps.

The key point of our calculation is in the latter equation: Gordon in Ref. [1] use a linear approximation $R(\nu) = 0.492(\frac{\nu}{13.2})$ which give a good description of the phenomenon only for soliton pulsewidth τ_s longer than the typical molecular period ($75\,fs$). In our experimental conditions we expect that the

initial solitons are longer than $75\,fs$. However in our mathematical model as well as in the experiment we may cope with time durations closer to this limit due to pulse compression. When solitons have pulse duration much shorter than the molecular oscillation response, SSFS is proportional to pulse energy. To consider all possible cases, we calculate the Raman loss spectrum using a Lorentzian approximation. The results of our calculation compared with results in Ref. [1] is shown in fig. 6.3(a). We observe a disagreement for solitons pulsewidths below 75 fs as we could expect. We

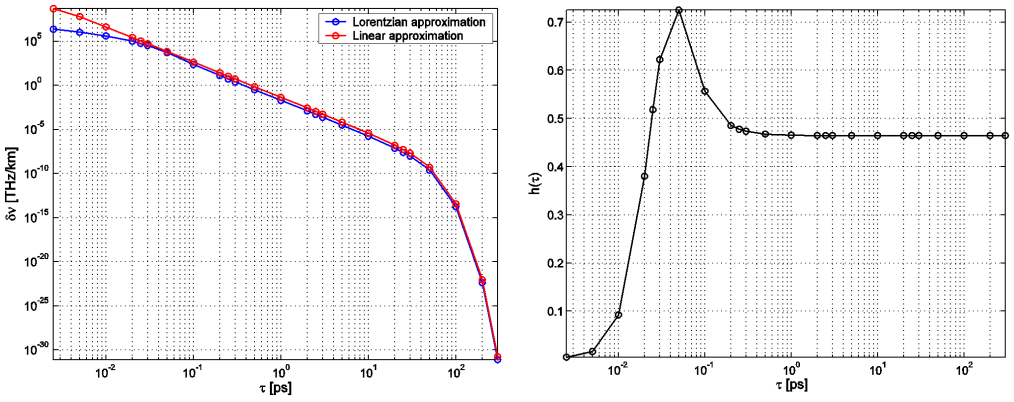

(a) (b)

Figure 6.3: (a) Calculated SSFS using linear (red) and Lorentzian (blue) approximation. (b) Numerically computed $h(t)$.

recall the result of Ref. [1] in terms of SSFS:

$$\frac{\partial \nu_0}{\partial z} \propto \frac{C}{\tau^4} \qquad \left[\frac{THz}{km}\right] \tag{6.26}$$

where $\tau = 1.763\,\tau_s$ is the FWHM transformation and C is depending on the fiber dispersion. We can reformulate our calculation so to have a direct comparison with that of Gordon (Ref. [1]). This is rendered possible by using a comparative function $h(t)$, such as:

$$\frac{\partial \nu_0}{\partial z} \propto \frac{C}{\tau^4} h(\tau) \qquad \left[\frac{THz}{km}\right] \tag{6.27}$$

Figure 6.3(b) shows the resulting values of $h(t)$. The disagreement previously mentioned is more evident in fig. 6.3(b).

6.3 Discussion

The procedure can be summarized as follow. Starting from an ensemble of input solitons whose peak powers and time widths are individually fixed as initial conditions, eq. 6.25 is used to evaluate the amount of SSFS between two consecutive collisions and eq. 6.13 is used to calculate the amount of energy exchanged during each collision. In practice though, it is then necessary to make some assumptions to determine a realistic set of initial parameters for the solitons from the given input pump pulse duration and peak power. We know that the soliton break-up due to MI takes place in a fiber distance which varies upon several conditions. One way to obtain the full description of each soliton would be to follow the propagation with a full numerical solution of the NLSE until solitons are clearly formed [5]. Of course different noise realization might cause different set of soliton parameters, so that finally one need to consider the stochasticity in input conditions when use our model. By using the eq. 6.1 we can calculate the total number of solitons, but not their parameters. We have followed, as in Ref. [5], a fully deterministic approach to calculate the soliton parameters. If MI period is much shorter than the input pump pulse T_0, one can image to fragment the input pulse into a discrete series of time bins, each of them described by the parameter T_{MI}. Then each time bins k give rise to a single soliton of the same energy. For Gaussian input pump pulse ($|A(t)|^2 = P_0 exp(-t^2/T_0^2)$), the optical energy falling in bin of index k is:

$$E_k = 0.5 P_0 T_0 \sqrt{\pi} W_k, \tag{6.28}$$

where $W_k = Erf((2k-1)\varepsilon) - Erf((2(k-1)-1)\varepsilon)$ and $\varepsilon = T_{MI}/2T_0$. Now the soliton durations is:

$$\tau_k = \frac{2T_{MI}^2}{\pi\sqrt{\pi}T_0 W_k}, \tag{6.29}$$

By fixing the time duration and assuming that all solitons are of the first order, it is easy to calculate the remaining soliton parameters (peak power and carrier frequency). At this stage, the only parameter that we have to calculate is the fibre length which is required to transform a Gaussian pulse into solitons bunch by means of MI. This fibre length represents the propagation length needed to obtain our initial conditions that we introduce in our model. To do that, we compare our input conditions to the soliton bunch obtained by solving NLSE for a given pump pulse propagating on a fixed fibre length (see fig. 6.4(a)). By the analysis of the solution of NLSE we are able to calculate the exact fiber length that we need to determine our input conditions. To exemplify this situation, we report in

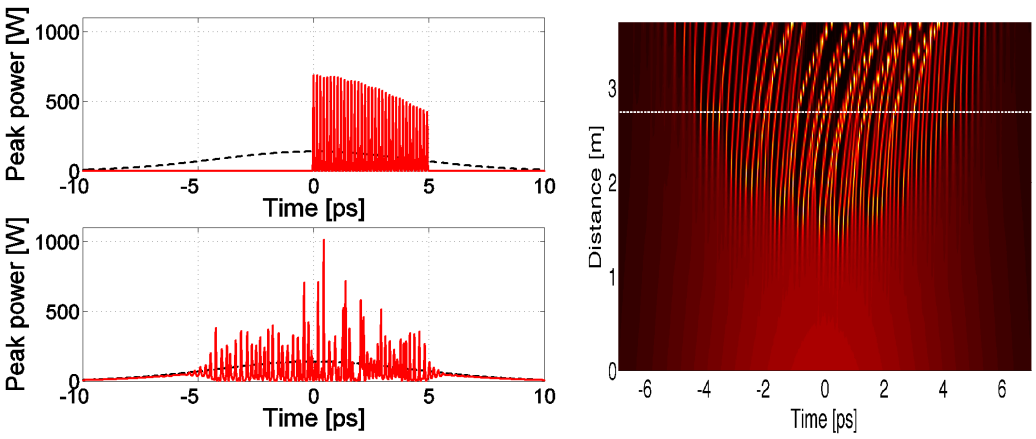

(a) (b)

Figure 6.4: (a) Example of input condition of our model (red curve upper figure) and pulse profile numerically computed by NLSE after the pulse break-up. In dark the input Gaussian pulse with duration 10 ps. (b) Example of 10 ps pulse break up and soliton formation from numerical solution of NLSE. The dashed white line indicates the fibre length required for the soliton train formation in our assumption.

fig. 6.4(b) the propagation of a 10 ps pulse into few meters of fibre. As we can see in fig. 6.4(b) a relatively regular pulse train appears nearby 2.7 m of propagation. After this length, collisions start to modify the symmetry of the soliton train. We show an example of results obtained from our analytical model in figure 6.5(b). On the left-hand side of this figure we plot the number of collisions upon the number of input soliton components directly linked to the input pulse duration (the number of solitons is imposed by MI). On the right side, we show how solitons spread out in different wavelengths during propagation in fibre. Note that here the coordinate $z = 0$ does not identify the input end of the fibre but the position where the soliton train is assumed as regularly formed.

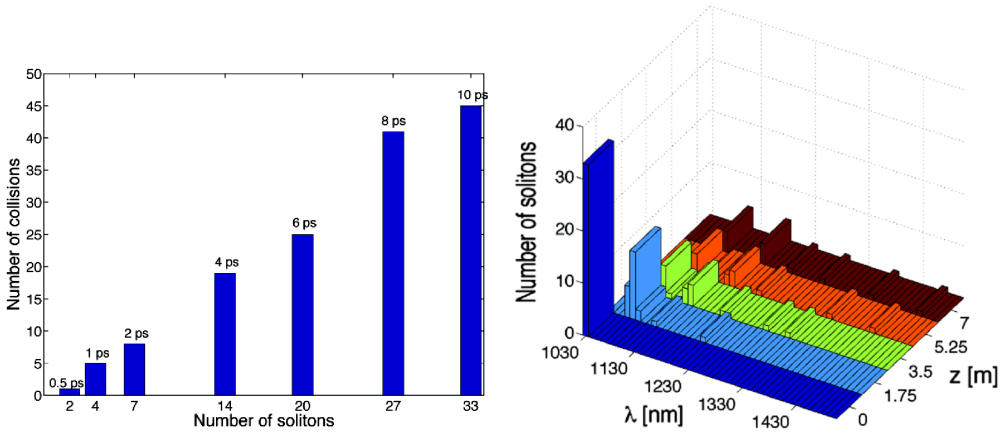

(a) (b)

Figure 6.5: (a) Analytical calculation of number of collision versus number of input soliton for different pulse duration. (b) Wavelength evolution of the solitons for an input pulse duration of 10 psn calculated along the fibre (z=0 m, z=1.75 m, z=3.50 m, z=5.25 m; z=7 m).

Now, after these considerations on the input conditions of our model, we compare on the fig. 6.6 our results. The input pulse duration varies from 500 fs to 10 ps and the input conditions introduced in our model match with the parameters obtained from numerical simulations. The green curve comes from a full numerical solution of NLSE, while the red

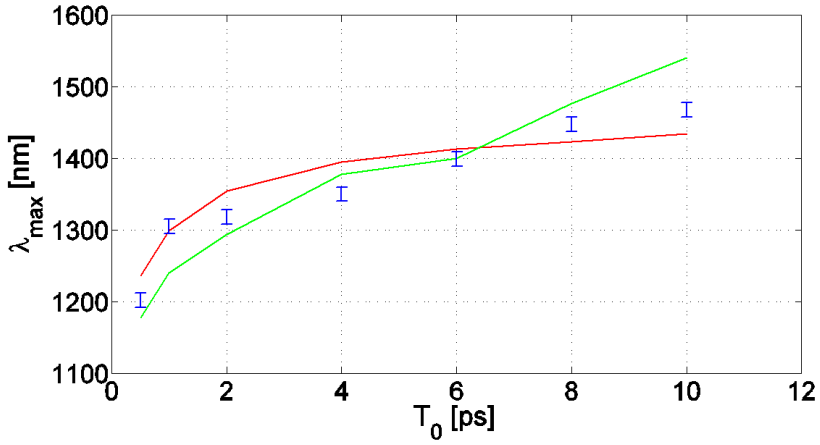

Figure 6.6: Comparative results: analytical solution (blue error bars), numerical solution of the largest red-shifted peak (green curve), experimental results at -20 dB (red curve).

one reports the experimental results of the longest spectrum measured at -20 dB (spectra of fig. 5.10).

The three curves show the same tendency, since the number of collision is proportional to the input pump pulse time width, the IR SC bandwidth is increased when the pump pulse duration grows larger.

6.4 Conclusion

In conclusion we have developed an analytical model that describes the enhancement of IR SC bandwidth through multiple soliton collisions. Our model is based on two main effects which are SSFS and soliton collisions. Additionally, we have identified some mechanisms limiting soliton red-shifting process:

- when the largest red-shifted solitons do not overlap in time with the remaining pulses;
- when the frequency detuning between colliding solitons becomes larger than the Raman gain bandwidth;
- when the colliding soliton has been fully depleted by the most red-

shifted soliton.

The transfer function that we have used for the SSFS takes into consideration these three mechanisms, and this is probably the reason why there is a fairly well agreement with the experiments that we have carried out. It is important to notice that the predicted SSFS obtained with our model, has to be compared to a mean result obtained by using numerical simulations including a random noise seed, or to the experiments obtained from averaging measurements. In fact, it is well-known that the observed SC spectra represent an average of spectra resulting from the various femtosecond red-shifted solitons that are obtained with quasi-similar pump pulses. We stress on the deterministic and not stochastic nature of the

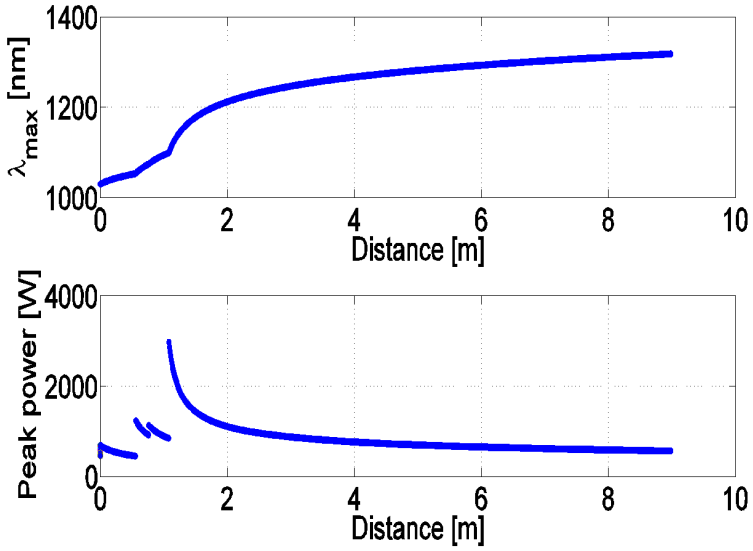

Figure 6.7: Upper frame: red-shifted soliton upon distance from analytical prediction, assuming pulse duration of 2 ps. Lower frame: peak power of the red-shifted soliton.

input conditions that we have assumed in our model. Moreover we have neglected multiple and simultaneous collisions (like triplets) as well as soliton phases. In fig. 6.7 we show the evolution of the carrier wavelength versus distance for the most red-shifted soliton as predicted from our model. Each discontinuity identify a collision involving such soliton. Other collisions pertaining to the other solitons are here not shown. Again

the distance here is measured from the point of appearance of the soliton train. One should add 0.5 m to obtain the approximated position in the fibre. As we can see, for each collision correspond an enhancement of the SSFS of the most red-shifted soliton.

We emphasize the fact that the mechanism of growing of infrared spectral component with pulse energy well agrees with a simplified model which takes into account multiple collisions during propagation.

Bibliography

[1] J.P. Gordon. Theory of the soliton self-frequency shift. *Optics Letters*, 11:662, October 1986.

[2] J.M. Dudley, G. Genty, and B.J. Eggleton. Harnessing and control of optical rogue waves in supercontinuum generation. *Optics Express*, 16:3644, March 2008.

[3] M.H. Frosz, O. Bang, and A. Bjarklev. Soliton collision and raman gain regimes in continuous-wave pumped supercontinuum generation. *Optics Express*, 14:9391, 2006.

[4] M.N. Islam, G. Sucha, I. Bar-Joseph, M. Wegener, J.P. Gordon, and D.S. Chemla. Femtosecond distributed soliton spectrum in fibers. *Journal of the Optical Society of America B*, 6:1149, June 1989.

[5] J.C. Travers. Blue extension of optical fibre supercontinuum generation. *Journal of Optics*, 12:113001, November 2010.

General conclusion

This thesis deals with the propagation and interaction of solitary waves (solitons) in media with second and third order non-linearities.

In a first step, I have investigated, in crystals, the spatial dynamics of two classes of solitons, that were first predicted in the 70s by Zakharov and Manokov. These solitons result from the energy exchange between waves of different velocities when the dispersion is negligible.

First, I have theoretically and experimentally investigated the spatial dynamics of two spatial narrow beams at frequency ω, which are mixed to generate a field at the sum frequency 2ω. Depending on the input intensity, when the generated field at 2ω can sustain a ZM soliton, it decays into ZM solitons at the fundamental frequency ω. This is the first evidence of transition from a steady frequency wave generation to solitonic decay in nonlinear optics.

In a second step, I studied the dynamics of a spatial narrow beam at frequency ω and a quasi-plane wave at frequency ω which are mixed to generate a beam at the sum frequency 2ω, when diffraction is negligible. Depending on the input intensities different nonlinear regimes exist: linear regime, frequency conversion regime and simultonic regime. Simultons are stable velocity-locked bright-dark-bright spatial triplets, determined by the balance between the energy exchange rates and the velocity mismatch between the interacting waves.

Our experimental findings on ZM soliton and simulton dynamics demonstrate the possibility of reaching soliton regimes in media where the diffraction is negligible. These nonlinear regimes could pave the way to the construction of novel systems for storing, retrieving and processing information in the optical and plasma domains.

Additionally ,I used the ZM soliton dynamics to develop a passive Q-switched mode-locked operation of a flash-lamp pumped Nd:YAG laser.

The ZM soliton creation is responsible for the high losses in the resonator which allows the mode-locking regime as it happens with saturable absorber. Indeed, the intensity threshold for mode locking is imposed by the corresponding threshold of ZM soliton formation. As results a train of pulses with duration close to 100 ps, repetition rate of 136 MHz and strong modulation depth is produced.

In a third step, I have experimentally and numerically investigated, in optical fibre, the soliton dynamics in the context of SC generation. I studied the dependence of the spectral broadening in the infrared associated with SC generation obtained in a PCF, by continuously varying the pulse temporal duration of a pump laser from picosecond to nanosecond. I have identified the crucial role played by the most energetic soliton (formed in the central part of the pump pulse), which is responsible for the IR broadening. Because of the corresponding dispersion-induced slowing down, this central soliton collides with all subsequent solitons in the train formed by MI. So, for different input pulse duration, MI break-up the pump pulse into a different number of soliton. The number of these solitons increase with respect to input pulse duration. This is how the IR SC spectra is formed by pumping in the anomalous dispersion region for long input pulses.

In this context, I have developed a simplified analytical model that describes the SSFS enhancement experienced by the most red-shifted soliton, as a result of its energy collection process from all of its neighbours. The mechanism responsible of the growing of infrared spectral component with respect to the pulse energy is in agreement with the results obtained by a simplified model which takes into account of multiple soliton collisions during propagation.

Part of the work about solitons in PCF has been carried out in the framework of an European project called "NextGenPCF". My PhD thesis has been done under a joint supervision program (Cotutelle-de-Thése) between the Universities of Brescia and Limoges. My work has been also

partially supported by the Université Franco-Italienne under the program "Vinci".

APPENDIX A

List of publications of Marco Andreana

Journal papers:

Pump pulse energy induced enhancement of short-wave infrared supercontinuum bandwidth
M. Andreana, A. Labruyère, A. Tonello, S. Wabnitz, P. Leproux, V. Couderc, C. Duterte, A. Cserteg, A. Bertrand, Y. Hernandez, D. Giannone, S. Hilaire, G. Huss
Sent to Optics Express.

Mode-locking operation of a flash-lamp-pumped Nd:YAG laser at 1.064μm with Zakharov-Manakov solitons
M. Andreana, F. Baronio, M. Conforti, A. Tonello, C. De Angelis, V. Couderc
Laser Physics Letters, DOI 10.1002/lapl.201110071 (August 2011)

Soliton Triads Ensemble in Frequency Conversion: from Inverse Scattering Theory to Experimental Observation
F. Baronio, M. Andreana, M. Conforti, G. Manili, V. Couderc, C. De Angelis, A. Barthélémy, A. Degasperis
Optics Express 19, pp. 13192-13200, 2011.

Velocity-locked solitary waves in quadratic media
F. Baronio, M. Conforti, C. De Angelis, A. Degasperis, M. Andreana, V. Couderc, A. Barthélémy
Physical Review Letters 104, 113902(1-4), 2010.

Adjustable supercontinuum laser source with low coherence length and low timing jitter
M. Andreana, A. Bertrand, Y. Hernandez, P. Leproux, V. Couderc, S. Hilaire, G. Huss, D. Giannone, A. Tonello, A. Labruyère, N. Rongeat, P. Nérin
Proc. of SPIE Vol. 7714, Photonic Crystal Fibers IV, 2010.

Frequency Generation and Solitonic Decay in Three Wave Interactions
F. Baronio, M. Conforti, M. Andreana, V. Couderc, C. De Angelis, S. Wabnitz, A. Barthélémy, A. Degasperis
Optics Express 17, pp. 12889-13894, 2009.

Conference papers:

Control of soliton collision-induced enhancement of supercontinuum bandwidth in photonic crystal fiber by variation of pump pulse duration
M. Andreana, A. Labruyère, A. Tonelllo, S. Wabnitz, P. Leproux, V. Couderc, C. Duterte, A. Cserteg, A. Bertrand, Y. Hernandez, D. Giannone, S. Hilaire, G. Huss
Rogue Waves Workshop, Dresden (Germany), November 2011

(**Invited oral presentation**).

Control of soliton collision-induced enhancement of supercontinuum bandwidth in photonic crystal fiber fiber by variation of pump pulse duration
M. Andreana, A. Labruyère, A. Tonelllo, S. Wabnitz, P. Leproux, V. Couderc, C. Duterte, A. Cserteg, A. Bertrand, Y. Hernandez, D. Giannone, S. Hilaire, G. Huss
Nonlinear Optics (NLO), presentation number: NTuC4, Kauai (Hawaii, USA), July 2011 (Oral presentation).

Experimental study and optimisation of pump laser parameters for supercontinuum generation
C. Duterte, M. Andreana, A. Cserteg, A. Bertrand, Y. Hernandez, D. Giannone, P. Leproux, V. Couderc, A. Labruyère, S. Hilaire, G. Huss
Fiber laser applications (FILAS), Istanbul (Turkey), paper: FThE4 , February 2011 (Poster session).

New biomedical opportunities offered by compact sub-nanosecond supercontinuum sources
P. Leproux, V. Couderc, A. Labruyère, M. Andreana, A. De Angelis
Photonics 2010, Guwahati (India), December 2010 (**Invited oral presentation**).

New mode locking operation of a pulsed Nd:YAG laser by using atypical three wave interactions
M. Andreana, V. Couderc, A. Tonelllo, F. Baronio, C. De Angelis
International Conference on Photonics and Applications (ICPA 6), Hanoi (Vietnam), paper: B-02, November 2010 (**Invited oral**

presentation).

New mode locking operation of a pulsed Nd:YAG laser by using atypical three wave interactions
M. Andreana, V. Couderc, A. Tonelllo, F. Baronio, C. De Angelis
Laser Physics Workshop 2010, Foz de Iguacu (Brasil), July 2010 (Oral presentation).

Observation of velocity-locked three-wave interaction solitons
F. Baronio, M. Conforti, C. De Angelis, A. Degasperis, M. Andreana, V. Couderc, A. Barthélémy
Laser Physics Workshop 2010, Foz de Iguacu (Brasil), July 2010 (**Invited oral presentation**).

Experimental And Numerical Investigation Of The Impact Of Pulse Duration On Supercontinuum Generation In A Photonic Crystal Fiber
M. Andreana, A. Bertrand, Y. Hernandez, P. Leproux, V. Couderc, S. Hilaire, G. Huss, D. Giannone, A. Tonello, A. Labruyère
Nonlinear Photonics (NP), Karlsruhe (Germany), paper: NTuC62, June 2010 (Poster session).

Adjustable supercontinuum laser source with low coherence length and low timing jitter
M. Andreana, A. Bertrand, Y. Hernandez, P. Leproux, V. Couderc, S. Hilaire, G. Huss, D. Giannone, A. Tonello, A. Labruyère
SPIE Photonics Europe, Brussels (Belgium), paper: 7714-1, April 2010 (Oral presentation).

Frequency generation and solitonic decay in three-wave nonlinear interactions

F. Baronio, M. Conforti, M. Andreana, V. Couderc, C. De Angelis, S. Wabnitz, A. Degasperis, A. Barthélémy
DGAO-SIOF Conference, Brescia (Italy), paper: C2 (110), June 2009 (Oral presentation).

Experimental Evidence of Three-Wave Zakharov-Manakov Solitons
F. Baronio, M. Conforti, C. De Angelis, A. Degasperis, S. Wabnitz, M. Andreana, V. Couderc, A. Barthélémy
Nonlinear Evolution Equations and Dynamical Systems (NEEDS 2009), Sardinia (Italy), May 2009 (Oral presentation).

Patents:

Source supercontinuum impulsionnelle à durée d'impulsion variable
M. Andreana, P. Leproux, V. Couderc, Y. Hernandez, A. Bertrand, S. Hilaire, P. Roy
Registered on April 8, 2010, n° 10 52662 (France)
Registered on April 8, 2011, n° PCT/FR2011/050505 (International)

Résumé:

En spectroscopie, aussi bien que dans beaucoup d'applications futuristes dans le biophotonique, la gestion des délais entre les différentes longueurs d'onde interagissant par l'intermédiaire de la non-linéarité peut ouvrir un itinéraire vers de nouvelles applications. Dans ce manuscrit la façon d'égaliser et de contrôler la vitesse de groupe des différentes régions d'un spectre optique est étudiée. Le contrôle non linéaire associeé à la connaissance de formes d'ondes optiques auto-supportées appelées solitons. Dans les cristaux, de nouveaux types de propagations solitonic et simultonic non linéaire au moyen de génération de somme de fréquence est étudiés. Cette dynamique peu commune de propagation permet la compensation de vitesse de groupe entre toutes les ondes en interaction.

Mots clés : Soliton, Simulton, Mode-locking, TWRI, Génération de supercontinuum, Interaction de soliton, Effet Raman.

Abstract:

In spectroscopy, as well as in many futuristic applications in biophotonics, the managing of time delays between different wavelengths interacting via the non-linearity may open a route towards new applications. In this manuscript the way to equalize and control group velocity of different wavelenghts is studied. The nonlinear control is related with the knowledge of self-sustained optical waveform called solitons. In crystals, new types of nonlinear solitonic and simultonic propagations by means of sum-frequency generation is studied. This unusual dynamics of propagation allows group velocity compensation between all the interacting waves.

Keywords: Soliton, Simulton, Mode-locking, TWRI, Supercontinuum generation, Soliton interaction, Raman effect.